Tribological Performance of Single and Multi-scale Textured Sliding Contacts under Lubricated Conditions

A thesis submitted in the partial fulfillment of the requirements for the award of the degree of

DOCTOR OF PHILOSOPHY

By

Mr. A. Ramana Reddy

(Roll No. 717019)

Under the supervision of

Dr. Syed Ismail

DEPARTMENT OF MECHANICAL ENGINEERING
NATIONAL INSTITUTE OF TECHNOLOGY WARANGAL
WARANGAL-506 004, TELANGANA, INDIA
2023

Dedicated to

My beloved Parents and Teachers

NATIONAL INSTITUTE OF TECHNOLOGY WARANGAL

DECLARATION

This is to certify that the thesis entitled "**Tribological Performance of Single and Multi-scale Textured Sliding Contacts under Lubricated Conditions**", is a bonafide work done by me under the supervision of Dr. Syed Ismail and was not submitted elsewhere for the award of any degree.

I declare that this written submission represents my idea in my own words and where others' ideas or words have not been included. I have adequately cited and referenced the original sources. I also declare that I have adhered to all principles of academic honesty and integrity and have not misinterpreted or fabricated or falsified any idea/data/fact/source in my submission. I understand that any violation of the above will be a cause for disciplinary action by the Institute and can also evoke penal action from the sources which have thus not been properly cited or from whom proper permission has not taken when needed.

Date:

Place:

A. Ramana Reddy

Research Scholar

Roll No. 717019

NATIONAL INSTITUTE OF TECHNOLOGY WARANGAL

CERTIFICATE

This is to certify that the thesis entitled "**Tribological Performance of Single and Multi-scale Textured Sliding Contacts under Lubricated Conditions**" that is being submitted by **Mr. A. Ramana Reddy** in partial fulfillment for the award of the degree of Doctor of Philosophy (PhD) in the Department of Mechanical Engineering, National Institute of Technology Warangal, India, is a record of the bonafide research work carried out by him under our guidance and supervision. The results of embodied in this thesis have not been submitted to any other University or Institute for the award of any degree or diploma.

Date:

Place:

Dr. Syed Ismail

Associate Professor

Department of Mechanical Engineering

NIT Warangal

ACKNOWLEDGEMENTS

I would like to express my sincere gratitude to my supervisors, **Dr. Syed Ismail** for their invaluable guidance and motivation throughout my Ph.D. I am highly indebted to them for their expertise while sharing their knowledge, understanding, encouragement and patience. I am immensely thankful to them for their valuable advices, correcting all my manuscripts, progress reports, thesis reports with great concern and commitment and spending their precious time with good discussions regarding my research work.

I wish to sincerely thank university authorities, **Prof. N. V. Ramana Rao**, Director, National Institute of Technology, Warangal and others who gave me an opportunity to carry out research work. I also sincerely thank **Prof. V. Suresh Babu**, Head, Mechanical Engineering Department, National Institute of Technology, Warangal for his continuous support towards carrying out research work.

Thanks are also due to **Prof. A. Kumar**, former Head, Mechanical Engineering Department, National Institute of Technology, Warangal for providing necessary departmental facilities and services during successful completion of research work. I wish to express my sincere and whole hearted thanks and gratitude to **Prof. R. Narasimha Rao, Prof. M. J. Davidson,** and **Dr. Arockia Kumar** (DSC members) for their kind help, encouragement and valuable suggestions for the successful completion of research work. I wish to thank **Dr. B. Sathish Ben** for his extended help during this work.

I would like to express my sincere thanks to all my friends and colleagues specially, to **Dr. Srinivas Reddy Badduri, Dr. Amrut Shrikant Mulay, Dr. K. Benarji, Dr. K. Nagu, Dr. Sri Chaitanya, Dr. Venkatesh Babu, Dr. Avinash Borgaonkar, Mr. Markandeyulu, Mr. Nagendra Prasad**, **Mr. Satish Margutti**, **Mr. Sasidhar, Mr. Kali Naresh, Mr. Bhargav Middimedi, Mr. Dhanraj Goteti and Mr. Venkata Ramanaih.** I would like to thank **Mr. L. Ramesh** and **Mr. K. Rohith**, Tribology Lab

technicians, and **Mr. Yellaiah**, Tribology Lab Ex-technician for their support during the completion of the research work.

I extend my gratitude towards mechanical office staff for quick response to my enquiries and supporting me indirectly by processing the documents submitted.

Words are inadequate to express my thanks to all my family members, my father **Mr. A. Yella reddy**, mother **Mrs. A. Bhagya Laxmi**, Brother **Mr. A. Raji Reddy,** Daughter **Manvitha Reddy** and especially my wife **Ms. Myakala Kavitha** for exhibiting patience during this long and arduous journey.

I want to express my sincere thanks to all those who directly or indirectly helped me at various stages of this work. Above all, I express my indebtedness to the "Almighty" for all his blessing and kindness.

A Ramana Reddy

Abstract

The demand for fuel-efficient and reliable machinery to reduce fuel consumption and costs is increasing progressively. In recent years, friction reduction has been one of the major studies in any mechanical moving parts to increase its mechanical efficiency and reliability of machine. Surface texturing has proved to be a reliable method to reduce friction. Surface texturing has proved to be a viable technique to reduce friction. However, selecting the optimized textural parameters for better tribological performance through experiments is time consuming and very costly. Therefore, a numerical code is developed to address the effect of texture depth, distribution (parallel and zig-zag) and area density on single scaled textured parallel sliding contacts on the tribological performance parameters like minimum film thickness, percentage of hydrodynamic load and frictional coefficient under mixed lubrication regime considering mass conservative cavitation condition. In addition, the effect of probabilistic surface roughness of contact surfaces and couple-stress parameter of lubricant are investigated.

Moreover, in most of the practical applications, load may not be constant and more than one lubrication regime exists. Employing single scale surface textures on the sliding surface may be efficient only for hydrodynamic lubrication condition but may not be efficient when more than one lubrication regime exists due to variation in the load. However, most of the mechanical components operate under varying loading and speed conditions. Therefore, a numerical analysis is performed to determine the optimum multi-scale textural configuration under mixed lubrication regime considering the mass conservative cavitation condition by varying textural parameters. The optimized multi-scale textural configuration is compared with single scale textures at varying load and speed conditions.

Experimental work gives clear idea on the effect of multi-scale textured sliding contacts on the tribological performance. Therefore, experimental tests were conducted for the obtained optimum multi-scale textural configuration to determine the tribological performance. Multi-scaled textures (Shallow and deep combination) are fabricated on low carbon steel of AISI 1020 through Nd: YAG laser and tested using on pin-on-disc friction and wear test rig.

The single-scaled numerical results show that texture shape has a significant effect whereas the texture distribution has a slight effect on the tribological performance parameters. Moreover, the couple-stress of lubricant has a prominent effect on the tribological performance. The multi-scaled numerical results indicated that the better tribological performance is observed when the shallow surface textures placed first towards the fluid inlet flow. It has been observed that multi-scale textures exhibit better tribological performance in comparison with single-scale textures at all considered loads. From the experimental results, it was found that multi-scale textural configuration for area density and texture depth of 0.3 and 10 μm exhibit better results in most loading conditions. Moreover, the obtained experimental results are compared with the available numerical results and observed that experimental results are in-line with numerical results with small deviation.

Keywords Couple-stress parameter, Jakobson-Floberg-Ollson (JFO) cavitation, Laser surface texturing, Mixed lubrication, Multi-scaled textures, Pin-on-disc test rig, Texture distribution, Texture shape.

Table of contents

List of Tables

List of Figures

List of Abbreviations

Abbreviation	Description
A_d	Area density
a	Area of the slider
S	Side length of unit cell
p_{atm}	Atmospheric pressure
A, K', Z	Parameters used in Greenwood and Tripp model (1970)
B	Actual texture size/beam size
Br	Breadth of the slider
C	Minimum film thickness
C_f	Boundary frictional coefficient
D	Specimen-lens distance
d	Density of material
E'	Combined young's modulus of sliding surfaces
E_1	young's modulus of sliding surfaces
E_2	young's modulus of stationary surfaces
F	Focal length of lens
F_{avg}	Average frictional force
F_{tot}	Total frictional force
F_a	Asperity friction force
F_h	Hydrodynamic friction force
g	Switch function
H	Surface roughness parameter
h	Film thickness of fluid
h_d	Texture depth
$h_{d,s}$	Texture depth of shallow texture
$h_{d,s}$	Texture depth of deep texture
Lg	Length of the slider
L_N	Applied normal load
l	Couple-stress fluid parameter

l_c	Diameter of a circular texture
l_e	Major axis length of an elliptical texture
$l_{e,s}$	Major axis length of a shallow elliptical texture
$l_{e,d}$	Major axis length of a deep elliptical texture
l_s	Side length of a square texture
l_t	Side length of a triangular texture
$l_{t,s}$	Side length of a shallow triangular texture
$l_{t,d}$	Side length of a deep triangular texture
N	Asperity density
n	Number of textures
nx, nz	Mesh grid in x and z-directions
nx_s, nz_s	Shallow mesh grid in x and z-directions
nx_d, nz_d	Deep mesh grid in x and z-directions
$n_{s,x}$	Number of shallow texture(s) in x-direction
$n_{s,y}$	Number of shallow texture(s) in y-direction
$n_{d,x}$	Number of deep texture(s) in x-direction
$n_{d,y}$	Number of deep texture(s) in y-direction
p	Hydrodynamic pressure
p_a	Asperity pressure
p_c	Cavitation pressure
p_l	Applied pressure
R	Required texture size/beam size
R_a	Average surface Roughness
Re	Relaxation factor
S_d	Sliding distance
U	Slider velocity
W_a	Weight of the sample after the experiment
W_b	Weight of the sample before the experiment
α	Bulk modulus of lubricant
β	Radius of the asperity peaks
γ	Surface pattern parameter

μ	Viscosity of lubricant
υ	Poisson's ratio of the surface
υ_1	Poisson's ratio of sliding surface
υ_2	Poisson's ratio of stationary surface
ρ	Density of oil at hydrodynamic pressure
ρ_c	Density of oil at cavitation pressure
τ	Shear stress of oil
ϕ	Fractional film content
φ_x, φ_z	Pressure corrective factor in x and z direction
φ_c	Contact factor
φ_s	Shear corrective factor
φ_f	Averaging the sliding velocity component of the shear stress
$\varphi_{fs}, \varphi_{fp}$	Shear stress factors

Chapter 1

Introduction

1.1 Background

Because of the limitation of fossil resources, power conservation has become a serious problem across the world (Holmberg and Erdemir (b), 2017). Moreover, there has been an increase in energy consumption due to rapid growth of the world's population edging closer to 400 Exajoules (Holmberg and Erdemir (a), 2019). Hence, there is a demand to design mechanically efficient, reliable machinery to minimize energy consumption (Denkena et al., 2020). In addition, global warming because of CO_2 emissions, threatens coastal regions, reduces crop production due to desertification, and impacts water supplies due to melting of glaciers (Olivier and Janses-Maenhout, 2015). As per International Energy Agency (IEA), the global mean temperature rise has to be restricted up to 2 °C from the current 15 °C by 2050 using some of the identified key technologies. The means to reduce the CO_2 emissions is shown in Fig. 1.1. It is clearly visible that most of the emissions can be reduced by energy efficiency. Friction reduction can be one of the feasible processes to improve the efficiency (Kovach et al., 1982, Kovalchenko et al., 2004) and reduce CO_2 emissions (Holmberg et al., 2012).

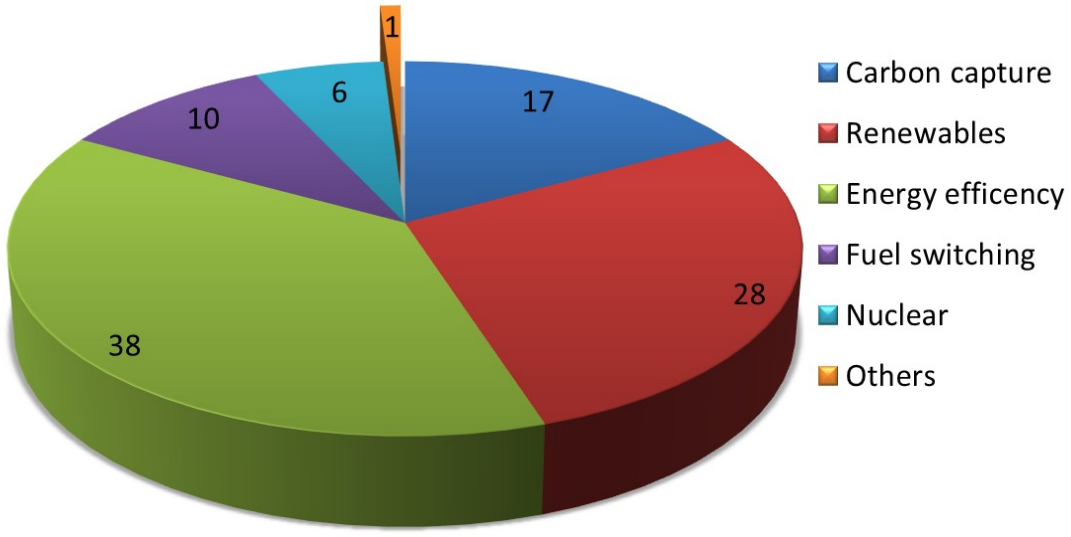

Fig. 1.1. Techniques to reduce the CO_2 emissions (Holmberg et al., 2012)

Moreover, it takes billion dollars to replace the worn parts of machinery or to replace entire worn machinery around the world (Zhao, 2014). Wear generally occurs due to the ploughing (abrasive wear) or shearing (adhesive wear). Wear leads to component degradation, eventually resulting in material failures or becomes less reliable (Chattopadhyay, 2001). Hence there is need to minimize the wear to enhance the service life of components and restrict machinery breakdown.

1.1.1 Friction and wear reduction

One of the reliable methods to reduce friction and wear between the sliding contact is surface texturing. Surface textures are the purposeful formation of cavities or protrusion on the surface. Over the past few years, surface texturing has drawn the scholar's attention because of their phenomenal nature between lubricated sliding contacts. Surface texturing is very effective in terms of improving the tribological performance of sliding surfaces. (Han et al., 2010). It is frequently used method for reducing friction and improving the wear resistance of tribological components (Gachot et al., 2017). The circular textures developed on a surface is shown in Fig. 1.2 (Tang et al., 2020).

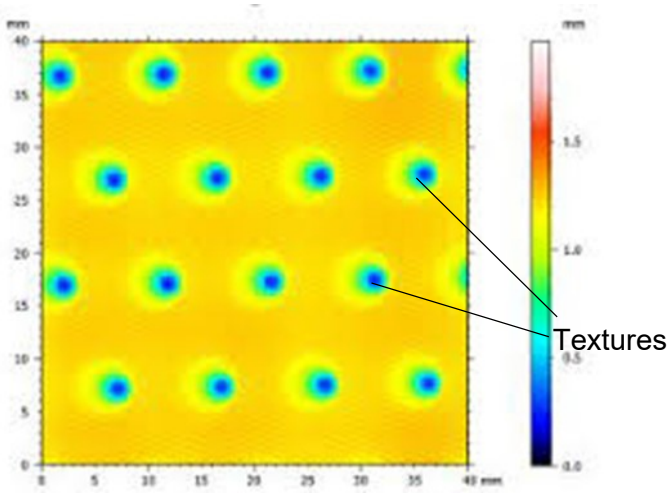

Fig. 1.2. Surface textures (Tang et al., 2020).

Surface textures behave like as a Rayleigh step bearing which creates hydrodynamic pressure even between parallel, flat sliding contacts (Etsion, 2005, Wang and Zhu, 2005, Pascovici et al., 2009).

Surface texturing improves anti-seizing ability (Martz, 1949 and Segu et al., 2013) and high durability (Blatter et al., 1999) of the contacts and avoid stiction in contact (Chilamakuri and Bhusan, 1997).

The concept of surface texturing is inspired by nature. It was also naturally found as micro- and nano-scaled textures on butterfly wings (Kinoshita et al., 2002, Malshe et al., 2013), and lotus leaf (Sun et al.,2005) to keep them super-hydrophobic, textures in the form of cuticles on plant leaf surface to restrict uncontrolled water loss, and surface wettability (Koch et al., 2009), nano structures on rose petal of flowers (Feng et al., 2010, Liu and Jiang, 2011) for brighter appearance, and well-defined multi-scale structures of mollusk shells and sponge spicules confer superior mechanical properties like strength and toughness (Mayer, 2005).

They are also found on ventral skin of the snakes for its locomotion (Abdel-Aal and El Mansori, 2013), special surface structures on tree frog's toes can increase adhesion, enabling them to safely walk on wet surfaces (Bhushan, 2009), skin of fish (Cui, 2021) and sharks (Wen et al., 2014) for fluid-drag reduction in turbulent flow. Due to the ability of shark skin to reduce drag force, Olympic athletes wear skin suits with riblets that mimic the texture of shark skin (Fu et al., 2017). Naturally found textures are shown in Fig. 1.3.

Surface texturing was traditionally used as traction in vehicle tires for enhancement of grip (De Wit and Tsiotras, 1999). A golf ball with peculiar textured surface has less drag and may fly up to four times farther than a golf ball with a smooth surface (Leong and Lin, 2007). Surface texturing was also found on the prosthetic hip implants (Holzwarth and Cotogno, 2012). The smooth and textured golf ball, and femoral head of hip implant is shown in Fig. 1.4. The human bone joint surfaces have cavities to maintain synovial fluid thereby reduce friction. Therefore, the human bone implants have surface with cavities to store the lubricating fluid so that they can supply lubricant and prevent joint destruction. Komvopoulos et al (1996 and 2003) found that the problem adhesion and stiction in Micro-electromechanical system (MEMS) devices is resolved by texturing.

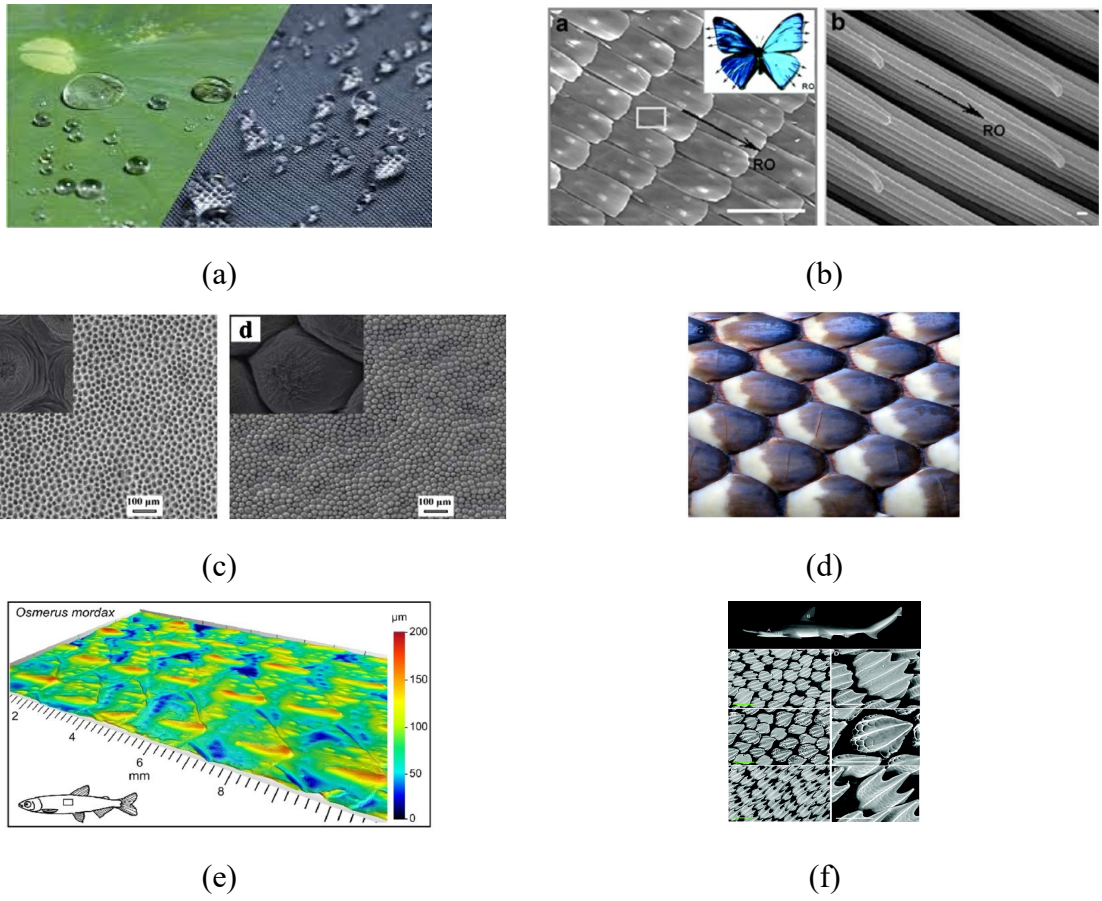

(a) (b)

(c) (d)

(e) (f)

Fig. 1.3. Naturally found textures in (a) Lotus leaf (Sun et al., 2005) (b) Butterfly wings (Kinoshita et al., 2002) (c) Textured rose petal (Feng et al., 2010) (d) Ventral skin of Snake (Abdel-Aal and El Mansori, 2013) (e) Fish skin (Cui, 2021) (f) Shark skin (Wen et al 2014).

(a) (b)

Fig. 1.4. (a) Smooth and Textured Golf ball (Leong and Lin, 2007) (b) Textured Femoral head of hip implant, (Uwe and Giulio, 2012).

Surface texturing is also used in machining operations like facing and turning, by providing the textures on rake face of the single point cutting tool (Nagendra Prasad and Syed, 2020). It also has paramount impact on low-load applications like mechanical seals (Ma et al., 2021), medium load applications like thrust bearing (Henry et al., 2021), shaft-journal bearings (Dadouche and

Conlon, 2016 and Song et al., 2022), piston rings (Ashwin and Sashidhar, 2012), cylinder liner (Miao et al., 2019) and cam-follower pair (Chong, 2014), and high load application like gears (Petare et al., 2020) and hydraulic pumps (Özmen et al., 2020). The machining and tribological applications of texturing is shown in Fig. 1.5.

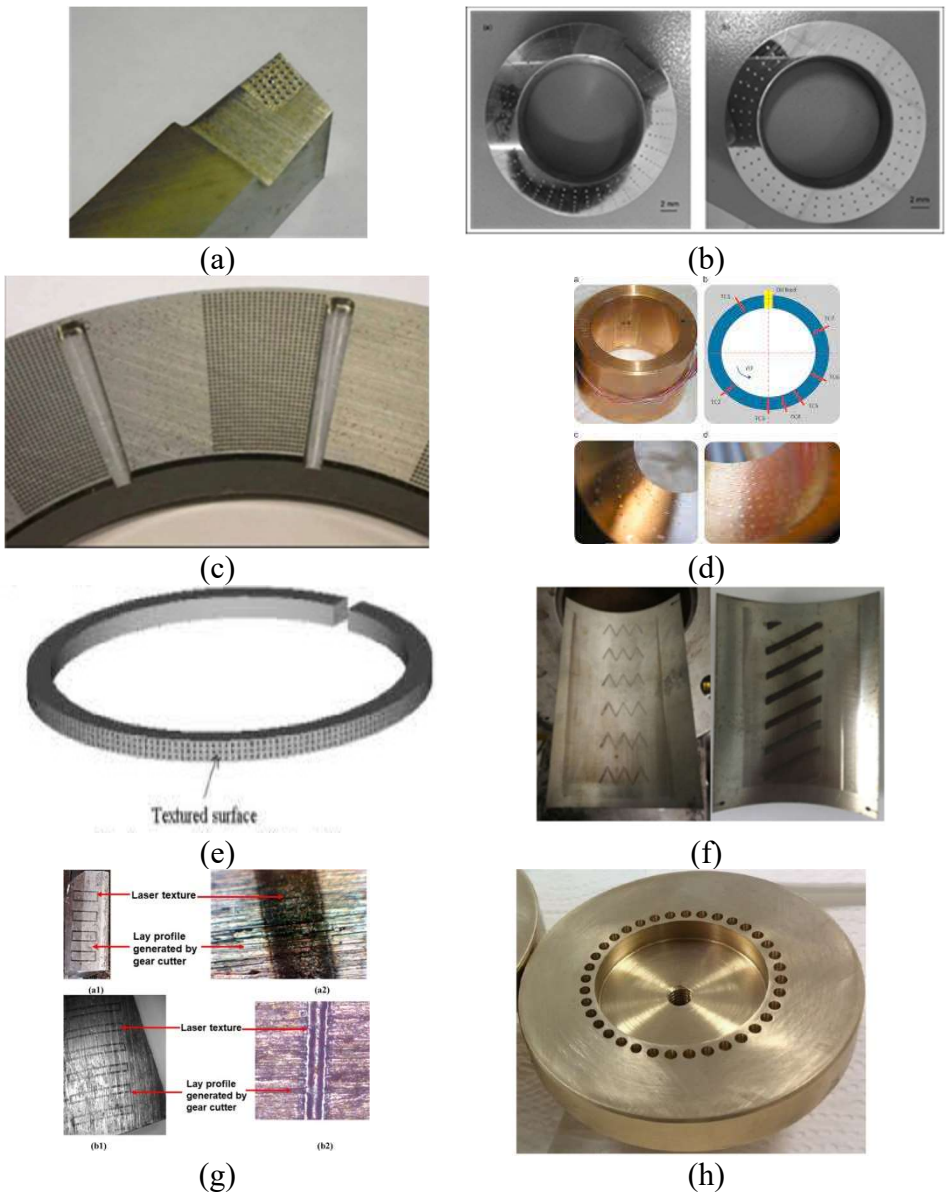

Fig. 1.5. (a) Single point cutting tool (Nagendra Prasad and Syed, 2020), (b) mechanical seals (Ma et al., 2021), (c) thrust bearing, (Henry et al., 2021), (d) journal bearings (Dadouche and Conlon, 2016), (e) piston rings, (Ashwin and Sashidhar, 2012) (f) cylinder liner (Miao et al., 2019), (g) homothetic texture on flank surface of a helical-gear tooth (Petare et al., 2020), (h) slipper of axial pump (Özmen et al., 2020).

1.1.2 Textural parameters

There are different textural parameters to optimize for better tribological performance. Different textural parameters are (a) Surface texture type, (b) area density of different texture shapes, (c) texture orientation, (d) texture distribution, (e) texture depth/height and (f) aspect ratio.

(a) Surface texture type: Surface textures can be positive or negative. Textures protruding out of the surface are positive and cavities inside surfaces are negative. Schematic diagrams of positive and negative textured surfaces are shown in Fig. 1.6.

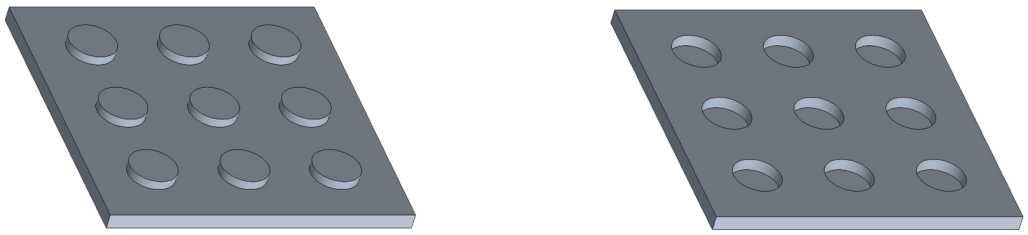

(a) (b)

Fig. 1.6. Square shaped (a) positive texture (b) negative texture.

(b) Area density*:* It is the ratio of total textural area to the total (untextured and textured) area of the surface. It can be increased by two ways either by increasing the size of the texture without altering the texture position or by increasing the number of textures by keeping the texture size constant. The area density can be calculated as

$$Area\ density(Ad) = \frac{Total\ texture\ area}{Area\ of\ the\ surface} \tag{1.1}$$

The texture areas for different shapes and the range of area densities for different textual shapes is shown in Table 1.1.

Table 1.1. Texture area calculation.

Texture shape	**Texture area**	**Surface area**	**Range of area density**
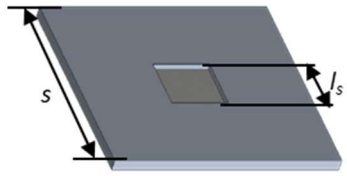	l_s^2	s^2	0-1
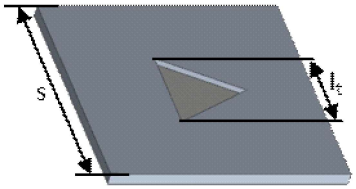	$\frac{\sqrt{3}l_t^2}{4}$	s^2	0-0.43
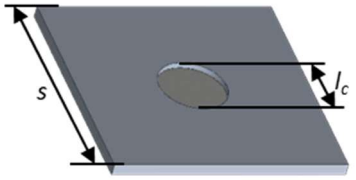	$\frac{\pi l_c^2}{4}$	s^2	0-0.75
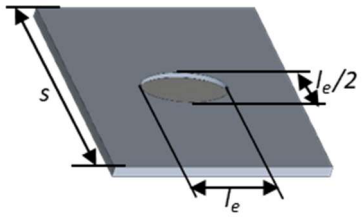	$\frac{\pi l_e^2}{8}$	s^2	0-0.39

***(c) Texture orientation*:** It is the alignment of a texture towards the fluid flow direction. Different orientations of triangular and elliptical textures are shown in Fig. 1.7.

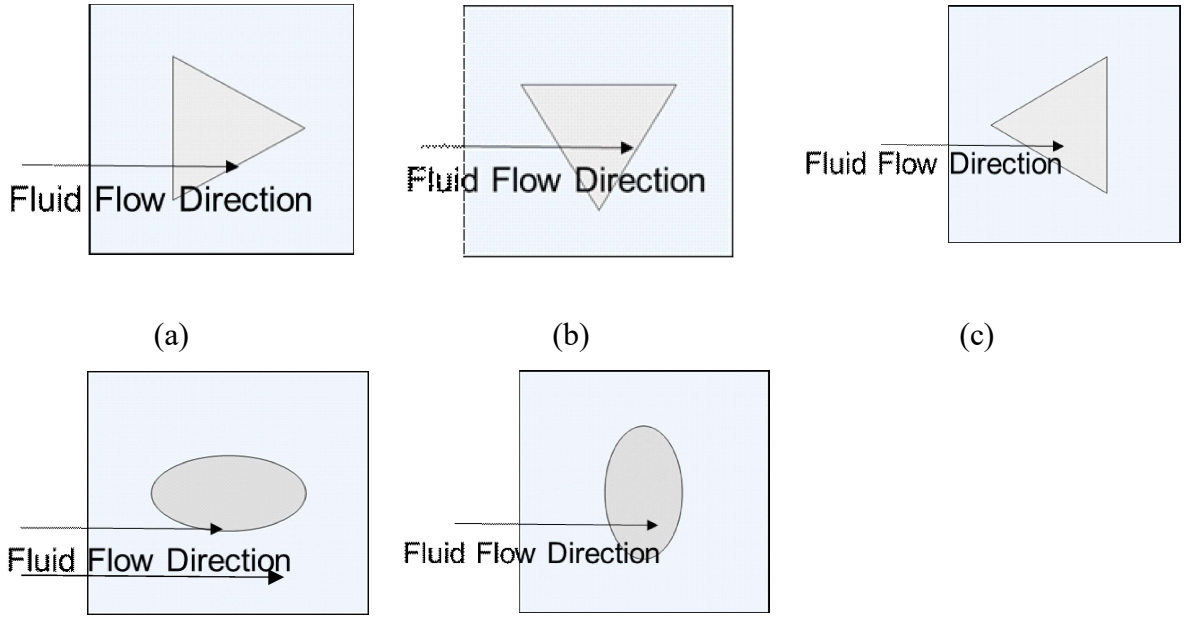

Fig. 1.7. Triangular orientations Fluid flow from (a) base to apex (b) parallel to base (c) from apex to base, elliptical orientations fluid flow (d) parallel to major axis and (e) perpendicular to major axis.

***(d) Texture distribution*:** It is the arrangement of texture on a surface. These arrangements can be square array, zigzag array, and hexagonal array. The different texture arrangements are shown in Fig. 1.8.

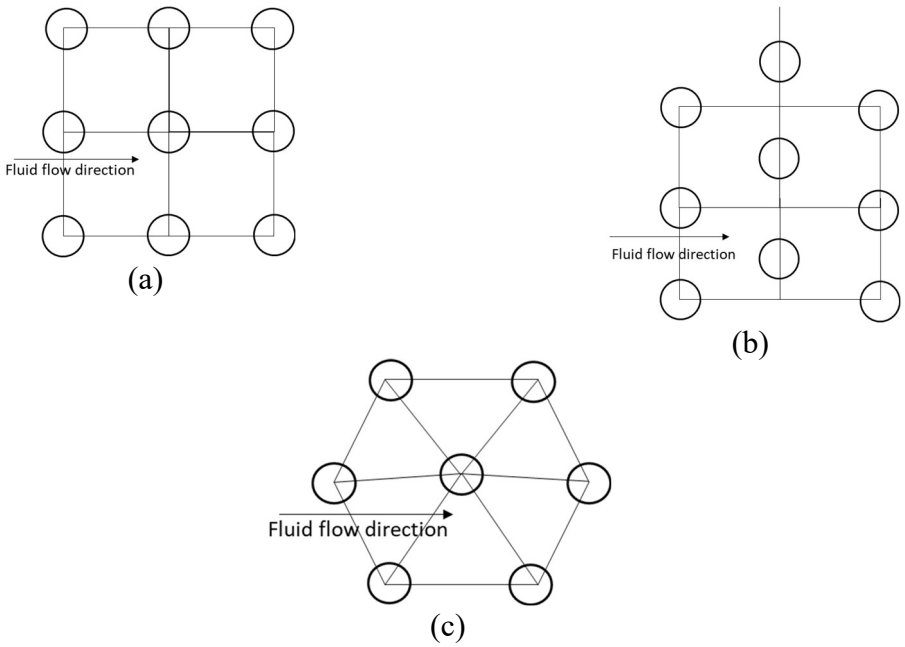

Fig. 1.8. (a) Square (b) zigzag/Staggered and (c) hexagonal texture distributions.

(e) Texture depth/height: It generally the depth/height of a cavity/protrusion from surface.

(f) Aspect ratio: It is the ratio of texture depth/height to the side length/diameter of the texture. This can be altered either by changing the depth or changing size length of texture

$$Aspect\,ratio\,(Ar) = \frac{Height\,(or)\,Depth\,of\,texture}{Side\,length\,(or)\,Diameter\,of\,texture}$$

Surface textures can be shallow or deep. The criteria for shallow and deep textures may be defined by the aspect ratio. The aspect ratio is defined as ratio of texture depth to texture diameter/side length (Kim et al., 2014).

Depending on the presence of textures on the surface, the textural surfaces are divided into (i) Single-scale textured surface, (ii) multi-shape textured surface, and (iii) multi-scale textured surface.

(i) Single-scale textured surface: Only single texture of same shape, size, depth, and orientation is distributed on the surface.

(ii) Multi-shape textured surface: Texture of two or more shapes are distributes on the surface of same size, depth, and orientation.

(iii) Multi- scale textured surface: Texture of two or more shapes are distributes on the surface of any size, depth, and orientation. An example of single-scale, multi-shape, and multi-scale textured surface is shown in Fig. 1.9.

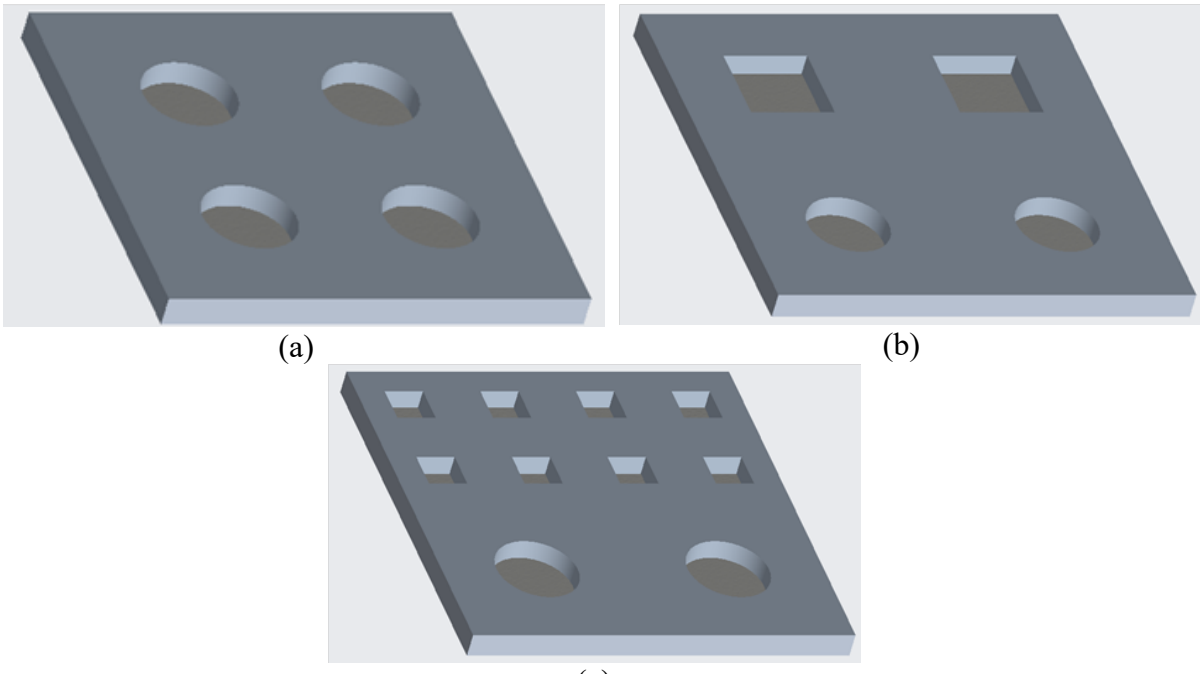

Fig. 1.9. Examples of (a) single-scale, (b) multi-shape, and (c) multi-scale textured surfaces.

1.1.3 Texturing Methods

As it can be observed that textures have significant applications, the textures of required shape area density type and depth can be fabricated using the following techniques. Conventional methods of texturing which was practiced by scholars are plunging with hard material to make micro-indentation (Keller et al.,2009), vibro-rolling (Greco et al., 2010), abrasive jet machining (Abhishek et al., 2018), micro-coining (Gachot et al.,2013), roller-coining (Szurdak and Hirt, 2015) micro-casting (Cannon and King, 2009), shot blasting (Nakano et al., 2007) and honing process (Grabon et al., 2014).

The advanced methods of surface texturing are LIGA process (Marques et al., 1997), Electro-Chemical etchings (Seidel, 1990) Electrical discharge machining (Aspinwall et al., 1992), (Chen and Ahmed., 1993) Electroplating Process (Stephens et al., 2002) and Plasma etching (Coburn and Winters, 1979) and laser surface texturing (Predescu et al., 2010).

1.2 Motivation and scope of the current work

In case of sliding contact conditions due to direct metal-metal contact, a higher amount of wear at the contacting surfaces takes place which results into failure of the entire system. To mitigate the friction and wear, currently surface topography modification in the form of surface texturing is one of the viable techniques to improve the tribological performance.

A lot of work is done on single-scale texturing. However no/little effect of texture depth, distribution, area density, velocity and couple-stress of fluid was studied. There is lack of understanding of tribological behavior of multi-scale surface textures on tribological sectors during different operating conditions of machinery. Due to these mentioned limited work on multi-scale textures, it motivates the design and development of single and multi-scale textures. Moreover, the fabrication of multi-scale textures and testing the multi-scale texture surfaces to investigate its tribological performance is still in process.

1.3 Summary

The introduction on importance of reducing friction and wear is explained. Among the methods of friction and wear reduction surface texturing is reliable method. Surface texture application and different textural parameters are addressed, and fabrication methods are also discussed. Single and multi-scale textures are explained, and the scope of work is discussed.

1.4 Organization of the thesis

The thesis has been organized under seven chapters, with the contents summarized as follows: **Chapter 1** deals with the importance of surface textures and their purposes in nature, textural parameters, and different texturing methods. This chapter also outlines the motivation behind the present research and scope of the current work. At last, the organization of the dissertation is discussed.

An extensive literature survey in the area of textural parameters has been outlined in **Chapter 2**. This chapter reviews the single-scale textures, multi-shape textures, and multi-scale textures and the stability of tribological parameters when multi-scale textures are introduced on the surface. Eventually, the research gaps were identified and a framework is established to fulfil the identified gaps.

Chapter 3 presents the numerical development of single-scale textures and numerical analysis of single-scale textures by varying textural parameters considering the effect of slider velocity and fluid couple stresses. This chapter deals with the tribological performance of the single-scale textures in terms of minimum film thickness, hydrodynamic load percentage, and frictional coefficient.

The numerical development of multi-scale textures and the evaluation of optimal textural parameter suitable for better tribological performance has explained in **Chapter 4**. The suitable model of multi-scale textures considering the effect of operating parameters like load and velocity has been explained. In addition, the comparison of multi-scale textures with single scale textures is done.

Chapter 5 deals with the laser fabrication of multi-scale textures. Laser texturing depends on wavelength, pulse number and frequency. Therefore, in this chapter, the effect of wavelength, pulse number and frequency on the produced texture size and depth is studied, and multi-scale

textures were fabricated using appropriate laser parameters.

Chapter 6 describes the experimental testing of fabricated multi-scale textures. The obtained experimental results are also compared with the numerical results.

Eventually, **Chapter 7** presents the overall conclusions drawn from the investigations carried out and it also suggests further recommendations for future work.

Success is like a shadow. If at all, You want it, don't go beyond it, but go towards the light, and it will follow You.

Dr. A P J ABDUL KALAM

Chapter 2

Literature Review

In the previous chapter, introduction about surface texturing and textural parameters involved in surface texturing and surface texturing methods are addressed. The current chapter deals with an extensive literature survey on importance of surface textures, textural parameters effect on tribological performance on single-scale, multi-shape, and multi-scale textures, and texture fabrication techniques. This chapter also provides a summary of the research gaps, research problem statement, research hypothesis and objectives of the present work.

2.1 Importance of surface textures

Surface textures are used in many applications to improve its performance in day-to-day life. These can be found in solar panels for better light trap (Green, 2002), micro-electro-mechanical devices to reduce stiction (Komvopoulos, 1996, Tay et al., 2011), surgical equipment to make them hydrophobic thereby improve the antibacterial property (Prakash et al., 2021) and etc. Dumitru et al. (2000) investigated the lifetime of micro-dimpled steel disks under mixed lubrication regime. Their results showed textured samples enhance the lifetime up to eight-times than untextured samples. Volchok et al. (2002) investigated the effect of textures on fretting fatigue life through an experimental fretting fatigue device. The two cylinders are oscillated against DIN-1.2510 tool steel plate either side using cantilever beam thus generating cylinder-on-flat contact type. They concluded that textures improve the average fretting fatigue lifetime to double of the untextured case.

Surface textures are used in many tribological machinery like piston rings (Dowson, 1993, Mishra and Ramkumar, 2018,) seals (Anno et al., 1968, Guichelaar et al., 2002), cylinder liner (Rahnejat et al., 2006) thrust bearings (Brizmer et al., 2003, Etsion et al.,2004) and journal bearing (Sinanoğlu et al., 2005, Galda et al., 2007). Pascovici et al. (2009) numerically analysed the textured conformal sliding surfaces with a simple one-dimensional isothermal flow model under hydrodynamic lubrication condition. They found that surface textures behave like as a Rayleigh step bearing which creates hydrodynamic pressure even between parallel, flat sliding contacts. Ronen et al. (2001) performed numerical analysis of circular dimples on

piston/cylinder system using Reynolds equation applying Swift-Steiber boundary condition. They concluded that there is pronounced interaction of fluid between adjoining dimples and there is considerable film pressure between the dimples. It can be observed that surface textures improve the tribological performance of mechanical components. However, varying textural parameters affect the tribological performance. The textual parameters effect on tribological performance is shown in below subsection.

2.2 Textural parameters effect on tribological performance of single scale textures

Many researchers worked on different textural parameters like texture type (positive and negative), shape, area density, depth, texture number, depth profile, orientation, aspect ratio and distribution. Optimized textural parameters are produced for improved tribological performance. The literature based on these parameters are described below.

2.2.1 Texture type and shape

Anno et al. (1969) experimentally analysed the effect of texture type (positive and negative) on film thickness under lubricated conditions. They used circular positive asperities in hexagonal array, square positive asperities in square array, and circular negative asperities in square array. They found that negative asperities obtain almost nil leakage producing sustainable film thickness. Moreover, Siripuram and Stephens (2004) numerically developed circular, square, diamond, hexagonal and triangular textures of both positive and negative texture types on parallel sliding surfaces. They studied the texture area density effect on frictional coefficient under hydrodynamic lubrication regime adopting Reynolds cavitation conditions. They observed that texture area density (for both positive and negative texture types) has significant effect on frictional coefficient and found that negative textures produce better mean hydrodynamic load and lower leakage rate than positive asperity. Moreover, they inferred that negative textures develop less edge stresses.

Shen and Khonsari (2016) performed experiments on square, semi-elliptical and trapezoidal textured low-carbon steel on reciprocating tribo-meter (CETR UMT-3). The counterpart used was cast iron with lubricant (SAE 10 oil) between contacts. They studied the effect of varying area density and depth on frictional coefficient. The experimental results show that the texture area density and depth have larger impact on the frictional behavior while the effect of the texture shape is very limited. In contrast, Galda et al. (2009) performed experiments on circular, long drop, and short drops textured on hardened 42CrMo4 steel ring samples using specially

designed tribometer. They investigated frictional coefficient by varying different textural parameters like area density and depth. The counterpart used for ring was EN-GJS 400-15 cast iron block with L-AN46 mineral oil as lubricant between them. They found that texture shape has paramount impact on friction coefficient in addition to texture area density and depth. Yu et al. (2011) experimentally worked on the effect of circular, elliptical and square textures and their orientations on frictional coefficient. They produced textures on boron–copper alloy and tested under reciprocating sliding tests with counter specimen as cast iron specimens and lubricant as diesel engine oil, CD 15W-40 at different dimple depths and dimple area ratios. They found that elliptical texture performs better tribological performance as compared to circular and square textures.

2.2.2 Area density and texture depth/height

Rahmani et al. (2010) numerically analysed negative and positive textures types on infinitely long parallel sliders under hydrodynamic lubrication applying Reynolds cavitation condition. They studied the effect of area density on maximum dimensionless load capacity. They came to conclusion that for both texture types, load capacity increases with area density. Tang et al. (2013) studied experimentally the effect of area densities on frictional behavior of circular shape textured sliding contact at a normal load of 150 N and an average sliding speed of 0.24 m/s. They found that higher area density produces better tribological performance. To justify this conclusion, they developed a numerical code to find area density effect on load carrying capacity, frictional coefficient of circular shape textures. They found that at higher area densities, better pressure contours are produced between adjacent textures thereby improving tribological characteristics. Yu and Sadeghi (2001) numerically studied the effect of area density, depth, and texture number on the hydrodynamic lubrication mechanism of thrust washers adopting Payvar-Salant's mass conservative cavitation conditions. The governing equation used was isothermal, transient Reynolds equation, adopting centrifugal effects. They concluded that thrust washers can produce higher load capacity with proper texture depth.

Sahlin et al. (2005) performed 2D CFD analysis on the effect of micro-grooves on load carrying capacity of parallel sliding surfaces at constant film thickness, and velocity with varying area density and depth using Navier-stokes equation. They concluded that there exists an optimum area density and texture depth where load capacity reaches maximum. Moreover, Han et al. (2010) analysed the effect of hemi-spherical texture depth on load carrying capacity and friction

coefficient based on Navier-Stokes equation through 3D CFD technique at varying area density. The result reveal that up to a certain depth enhanced load capacity and frictional coefficient was observed. Wang et al. (2015) performed numerical analysis to study the area density effect on load capacity of Rayleigh step bearing through finite element method. They incorporated stress concentration factor in the numerical analysis for different materials are Silicon carbide (SiC) and Ultra-high molecular weight polyethylene (UHMWPE). They inferred that high stiffness material i.e., SiC produces high stress concentration around the rim of texture as compared to low stiffness material i.e., UHMWPE.

Szurdak et al. (2014) performed experimental analysis on elliptical and circular textured AISI 304 low carbon steel sheets, textures fabricated through micro-coining. They analyzed micro-coined and uncoined sheets on ball-on-disk tribometer by varying the area density and texture depth with Al_2O_3 ball as counter-body with lubricant as Poly-alpha-olefin (PAO) oil. They analyzed the effect of frictional coefficient and wear rate at a constant load. They found that micro-coined specimens of higher textural depth produce lower wear rate since higher depth trap more wear volume. Moreover, they concluded that much higher area density textures produce higher frictional coefficient due to increased contact pressure. Li et al (2014) performed laser texturing through Q-switched Nd: YAG laser on copper plate. They studied the friction and wear effect through pin-on-disk tribometer with varying dimple area densities of 0.05, 0.13, and 0.35 at constant depth of 10 μm. The pins are made of GCr15 steel and textured disk of Oxygen-Free High Conductivity copper with lubricant between the pin and disk as Mobil Vacuoline 1405 oil. They concluded that an increase in texture density creates more space for lubricant to reserve which reduces frictional heat generation. This was also confirmed by Henry et al. (2015) by producing square-shaped dimples on parallel thrust pad bearing.

Wu et al. (2018) performed experimental work to study the effect of texture area density on frictional coefficient and wear rate. They performed frictional and wear tests on textured mirror-finished AISI 420 stainless steel discs with AISI 316 l stainless steel ball as a counterpart using reciprocating ball-on-disc tribometer with deionized water as lubricant between them. They concluded that higher area density exhibited better friction reduction. Moreover, they found that friction and wear rate increase in edge profiled textures due to stress concentration at relatively high load-low speed conditions. They suggested that wet polishing chamfer the textured edges thereby producing no/less stress concentration compared to normal polished textures. Bai et al. (2021) investigated on the friction reduction and wear life of un-textured,

groove and circular-textured SiC surface through a ball-on-plate test rig under dry, water lubricated and oil lubricated conditions. They used different counter body surfaces such as 52100 steel, silicon nitride (Si3N4), and poly-tetra-fluoro-ethylene (PTFE). The groove and circular textures of depths 3 μm, 5 μm, and 10 μm at constant texture area density are fabricated through pulsed laser setup. They found that texture depth has significant effect on friction and wear life. Moreover, they observed that groove and circular-textured SiC–steel and SiC– Si_3N_4 friction pairs exhibit a significant effect on friction and wear life as compared to untextured SiC-steel and SiC–Si_3N_4 friction pairs at dry and lubricated conditions. Wakuda et al. (2003) performed surface texturing using abrasive jet machining and laser beam machining to produce different texture depth profiles. They analyzed the effect of frictional coefficient on textural parameters using pin-on-disc tribometer. The pin and disk used was hardened steel and hot-pressed silicon nitride ceramic respectively. They concluded there is negligible change in tribological performance with change in texture depth profile.

2.2.3 Texture number

Rahmani et al. (2007) investigated the optimal geometrical parameters of square-shaped textured parallel thrust bearing on tribological performance characteristics including load support and friction coefficient. In their analysis a one-dimensional Reynolds equation was considered adopting sommerfeld cavitation condition under hydrodynamic lubrication regime. They analyzed three parameters namely number of textures, length ratio (texture size to consecutive texture distance ratio) and height ratio (texture height to minimum film thickness ratio). The results indicated that texture number increment didn't affect the tribological performance in terms of load support or friction coefficient. This was also confirmed by Pascovici et al (2009) considering flow conservation cavitation condition.

Fowell et al. (2012) numerically developed rectangular shaped textures and assessed the influence of texture number on load capacity of parallel slider under hydrodynamic lubrication regime at constant area density and varying film thickness. They observed that the number of textures had little effect on load carrying capacity. In contrast, Guzek et al. (2013) numerically developed elliptical and rectangular textures and analyzed the effect of area density and texture number on hydrodynamic load carrying capacity and frictional coefficient at constant minimum film thickness and sliding velocity using mass-conservative model. They observed higher hydrodynamic load carrying capacity and lower frictional coefficient at higher area density and

lower texture number along the lubricant flow direction. Gherca et al. (2013) analyzed the rectangular, triangular, and parabolic textured parallel sliding contacts under hydrodynamic lubrication regime using mass-conservative model. They investigated the effect of texture number on load capacity and frictional coefficient at constant oil viscosity and sliding speed. They found that lower texture number produces better tribological performance at lower texture depth and vice versa.

2.2.4 Texture orientation

Yu et al. (2010) numerically worked on the hydrodynamic pressure between circular, elliptical and triangular textured conformal contacting surfaces. In addition to texture shape, texture orientation is also considered under hydrodynamic lubrication regime adopting Reynolds cavitation condition. They found that ellipses with major axis positioned perpendicular to the lubricant direction and triangle diverging along the lubricant direction gives higher hydrodynamic pressures than other orientations, showing a strong orientation effect. Moreover, they claimed that for better hydrodynamic pressures the ratio of long to short axis of elliptical texture should be maintained in the range of 2 to 6. Moreover, Syed and Sarangi (2014) performed numerical analysis to study the effect of tribological performance on surface textural shape namely square, hexagonal, triangular, ellipsoidal and elliptical, and their orientation on frictional coefficient. The governing equation used was Reynold's equation deduced from Navier-Stokes equation by incorporating and retaining fluid inertia effects in their numerical solution. They adopted Reynold's cavitation condition and found that elliptical texture oriented with minor axis parallel to sliding direction and triangular texture aligned from base to apex along sliding direction performs better tribological performance.

Yue et al. (2019) experimentally worked on the parallel, inclined and perpendicular groove textures on single and both side of the surfaces. Both materials were made of AISI 1045 and AISI 5140 and were textured with Nd: YAG laser. They were tested on a reciprocating guideway testing machine with commercially available guideway oil (L-G 68) was used as lubricant. They found that both side textured surfaces with groves in parallel orientation and moving parallel to each other, perpendicular to each other and inclined to each other produce higher friction coefficient due to stick slip condition and occlusion of contacts. Moreover, they found that both side textured surfaces with groves in perpendicular or inclined to each other and moving parallel or inclined to one of the surface produce lower friction coefficients.

Experiments have been carried out by Yuan et al. (2011) to study the effect of groove orientation and depth on friction coefficient through reciprocating test rig. Both contact specimens were made of boron–copper alloy cast iron with the lubricant between the contacts as diesel engine oil of CD 15W-40. The groove patterns were created on one of the surfaces with the aid of lithography and electrolytic etching. They found that micro-groove's orientation has paramount impact on friction coefficient. This research shows grooves perpendicular to the sliding direction reduces friction better than parallel grooves under relatively low contact pressure due to hydrodynamic effect. Moreover, the grooves parallel to the sliding direction are more effective in reducing friction under relative high contact pressures than those perpendicular to the sliding direction because parallel sliding minimizes contact stress effect. They concluded that the best configuration for all loads is usually the angle between grooves.

Wang et al. (2013) experimentally worked on the effect of triangle texture orientation on frictional coefficient using ball on disc tribometer. They studied with different textural parameters like area density texture depth, and coverage ratio at varying speeds, and constant load. The textures were made on 45# steel disk in clockwise (CW), counter-clockwise (CCW) and radial directions to disk movement. They used untextured steel ball as counterpart with lubricant between the contact as base oil Y6. The dimples arrays were textured by nanosecond laser. They found that the textures in CCW orientation (fluid moving from base to apex of triangle textures) produced lower frictional coefficient at all speeds for a texture area density and depth. Xie et al. (2014) experimentally analyzed textural shape (circular and triangular) and orientation (flow from base to apex and apex to base of triangle) effect on frictional coefficient using computer controlled rotary tribometer. The textures are made on rotating sintered SiC using Nd: YAG laser. The counterpart ring is stationary and made of carbon and the oil used for Lubrication is deionized water. They concluded that the triangular textures with fluid flowing from base to apex give better frictional coefficient reduction. To prove this, they conducted numerical experiments and found that pressure contours of triangular texture with fluid flowing from base to apex are higher. This was also confirmed numerically by Syed and Sarangi (2013).

Hsu et al. (2014) experimented circular, elliptical and triangular textured parallel sliding contact through pin on disk set up for high speed/low load conditions and ball-on-three flat disks for low speed-high load condition. They used Paraffin oil as lubricant for both testing conditions. The pins and disc made of mild low carbon steel of ANSI 1017–1018 type for high speed/low

load conditions. The ball and flat are made of 52100 high carbon steel for low speed-high load conditions. They found that the oil flow direction perpendicular to major axis of elliptical and towards the base of the triangular textures generated better reduction in frictional coefficient. Zhan and Yang (2012) analyzed the effect of texture distribution angle on wear characteristics of the cylinder liner of cylinder–piston ring system. The circular shaped textures **of** constant depth and area density with different distribution angles of 0° (90°), 15°, 30°, 45°, 60°, and 75° are produced through Nd: YAG laser. They found a strong correlation between wear characteristics of cylinder liners and piston rings and the laser-textured distribution angle and higher reduction in wear is observed at laser-textured angle of 60◦.

2.2.5 Aspect ratio

Costa and Hutchings (2007) experimentally analyzed circular depressions, grooves, and chevrons at different aspect ratios. They textured on steel samples (AISI 01 GFS) with lubricant as additive-free mineral oil. They found that lower and medium aspect ratios exhibit better tribological performance. Higher aspect ratio gives negative effect on tribological performance since stress concentration rises with increase in texture height. Thus, they inferred that aspect ratio is a useful parameter in deciding the hydrodynamic load support and frictional coefficient. Moreover, Ahmed et al. (2016) in his review paper found that aspect ratio is the most influential parameter in determining frictional coefficient in case of mechanical seals and piston ring cylinder liner assembly.

Uddin et al. (2017) examined the effects of circular, elliptical, hexagonal, triangular, and square textural shapes considering the contact pair in hydrodynamic lubrication regime considering Reynold's cavitation condition. The effect aspect ratio on film thickness and friction coefficient was studied for single-scaled textures. Their findings determined that textures with an aspect ratio less than 0.01 were shallow since they produce higher film thickness at lower loads, and textures with a ratio greater than 0.01 were deep. By adopting same cavitation condition, Qiu and his co-workers (2012, 2013, and 2015) numerically investigated patterns of spherical, ellipsoidal, elliptical, circular, triangular and chevron textured parallel slider contacts in hydrodynamic lubrication regime adopting Reynold's cavitation condition to find hydrodynamic load capacity, frictional coefficient, and end flow rate. They varied aspect ratio and area density in the range of 0.01-0.1 and 0.05-0.8 respectively. For each of the dimple shapes considered, the optimal geometry was found with texture height to diameter/side length

ratio in the range of 0.001 to 0.010 and area density in the range of 0.10 to 0.35. Moreover, they found reduced frictional coefficient and load capacity when the minor-axes length of the elliptical texture is half of major-axes length. In addition, Murthy et al. (2007) analyzed the aspect ratio effect of spherical dimple texture on frictional coefficient. It was concluded same that aspect ratio 0.001 to 0.01 shown better results.

Wang et al. (2002) studied circular, micro-textured seal sliding in water where both contact surfaces were made of SiC. The influence of aspect ratio and area density of textures on load carrying capacity is calculated. They found that critical load ratio which is a measure of load carrying capacity initially increased and then gradually degraded/lowered with the aspect ratio. They also observed that and found that both aspect ratio and area density have significant influence on load carrying capacity. In contrast, Wang et al. (2003) in another paper studied circular micro-textured thrust bearing sliding in water and found that aspect ratio of textures has higher influence than area density. Rosenkranz et al. (2018) experimented on surfaces having single scaled elliptical textures made by hot micro-coining. They analysed the effect of pitch area density and aspect ratio on frictional coefficient with varying speed. They used a ball-on-disc tribo-meter (CSM Instruments micro-tribometer) with a disc made of low carbon steel (AISI-304), alumina ball as counter body and Poly-alpha-olefine oil (PAO 40) as a lubricant between them. They found that higher area density and lower aspect ratio gives better frictional coefficient at all speeds.

2.2.6 Texture distribution

Yin et al. (2018) calculated film pressures of different texture distributions like square array, staggered array, stretching along liner axis array and shortening along liner axis array in piston ring cylinder assembly with the mixed lubrication model adopting Reynolds cavitation condition. They found that square array distribution produces higher film pressure followed by shortening along liner axis array and stretching along liner axis array. Staggered array is the most inefficient in producing higher film pressure.

The literature shown in the earlier section was for the case of single-scale textures. Certainly, single scaled texture does not improve the tribological performance at all operating conditions. Single-scale textures exhibit poor tribological performance in some operating conditions like high-load and low-speed, and dynamic load-speed conditions. Therefore, it is recommended to have multi-shape or multi-scale textures to improve the tribological performance at varying

load and speed conditions. This idea of multi-shape textures and multi-scale textures to improve tribological performance was confirmed by Segu and Kim (2014) and Blau and Hsu (2014) respectively. However, a little literature was found on the multi-shape and multi-scale textures which is explained in the below sections.

2.3 Effect of textural parameters on multi-shape textures

The combination of two or more shaped textures on a surface are named as multi-shape textured surfaces. Most of the literature found with respect to multi-shape textures are the experimental works. Moreover, the multi-shape textures used in the experimental work are negative type.

Segu et al. (2013) performed experiments on un-textured, circular and combinations of circular and triangular, and circular and square shape textured sliding surfaces at different area densities. They studied the effect of area density on frictional coefficient and wear life using a pin-on-disc tribometer under MoS_2 lubricated conditions. Both pin and disc are made of hardened stainless steel (AISI 52100) and textures were made on disc using laser surface texturing. Their study revealed that multi-shape textures improve tribological performance. They concluded that area density was an important factor at high and low loads in reducing friction and higher wear life. This was also confirmed by Segu and Kim (2014) under similar load, speed and textural conditions using a ball-on-flat tribometer with poly-alpha-olefin oil as a lubricant.

Moreover, Segu and Hwang (2015, 2016) using same texturing process, experimentally analyzed the multi-shape textures of circular-ellipse, in addition to circular-triangular, and circular-square textures through pin-on-disc tribometer under dry and lubrication conditions Their study revealed that multi-shape textures with higher area density gives a better reduction in friction. In addition, they also found that frictional coefficient is stable when multi-shape textures are introduced on the surface. Zhan et al. (2020) performed experimental work on dimpled, grooved and sinusoidal textures in individual and mixed patterns (dimpled-grooved, grooved-sinusoidal and sinusoidal- dimpled) at constant area density and texture depth. The sliding tests were conducted using a pin-on-disc friction tester under dry conditions. The pin and disk are made of GCr15 and 40Cr steel material respectively. A nano-second laser is used to produce textures on 40Cr steel surface. The results showed that multi-shape textured surfaces exhibit lower frictional coefficient than individual textured surfaces.

2.4 Effect of textural parameters on multi-scale textures

Multi-scale textures are presence of textures of different shape and scale on a surface. There is a little work on the textural parameters effect on multi-scale textures. Moreover, all of the multi-scale texture literature is based on the experiments and analyzed only on circular texture shape with cross like patterns. Grützmacher et al. (2019) in his review paper found that single-scale surface textures are better only at lower loads but unfavorable when load is increased. However, they mentioned that multi-scale textures produce better tribological performance at both lower and higher loads. They also inferred that fabrication of multi-scale textures of different geometric shape, size, and depth on sliding surfaces can stabilize the frictional coefficient at all lubrication regimes.

Therefore, a new concept called multi-scale textures is developed by Hsu et al. (2015) conducted experiments to improve the tribological performance under varying load and speed conditions. They designed the single-scaled textures along with mixture and overlapping textural patterns of multi-scale textures with a combination of a parallelogram and droplet-shaped textures and studied the effect of multi-scale textures along with single scaled parallelogram and droplet-shaped textures on frictional coefficient through a ball-on-three-flats tribometer. The balls and discs were made of 52 100 steel ball bearings with lubricant as paraffin white oil. They inferred that multi-scale textures of both patterns produce comparable frictional coefficients with a minor deviation and multi-scale textures produce superior tribological performance as compared to single-scaled (individual) textures. . In a similar manner, Wang et al. (2006) analyzed circular and rectangular textures using ring on disc tribometer with purified water as lubricant. They studied individual and mixed textural patterns effect on frictional coefficient of sliding pair. Both ring and disc were made of SiC material and textures were produced on disc through lithography and reactive ion etching. They found that introduction of mixed pattern (combination of circular and rectangular textures) depicts a significant reduction in frictional coefficient.

Grützmacher et al. (2018) developed a cross-like surface patterns and hemispherical surface patterns using laser interference patterning and hot micro-coining respectively. Through their experiments on ball on disc tribometer, they studied frictional coefficient of single-scale texture (individual cross-like or hemispherical surface patterns) and multi-scale texture (combination of cross-like and hemispherical surface patterns) They found that these multi-scaled textures produced lower frictional coefficient than single-scale textures. The same has been observed in

the work of Rosenkranz et al. (2021). Furthermore, Grützmacher et al. (2018, a) studied the influence of single-scale (laser textured or roller coined) and multi-scale (laser textured and roller coined) textured surfaces on frictional coefficient using journal bearing test. The bearing was made of low carbon steel (AISI-304), and the textured journal was made of a copper alloy (CuSn12NiC-GCB). They found that significant amount of frictional coefficient is reduced using multi-scaled textual surfaces as compared to single-scale texture models.

2.5 Surface texturing fabrication methods

There are many texturing processes from mechanical, chemical, electro-chemical to electron or ion beam processing. There are advantages and disadvantages associated with each of these methods. Mechanical surface texturing, for example, is a simple and low-cost process, but the control on texture uniformity and depth is troublesome. The mechanical properties do not change with chemical etching and there is zero machining force or surface damage. However, it requires larger time consumption in printing masks and etching. Moreover, the masking is done on trial-and-error basis for producing accurate texture size (Arslan et al., 2016). Electron or ion beam processing techniques, in general are high precision texturing technique and can generate textures even of nano-size (Kurella and Dahotre, 2005). However, it is high processing cost, as it needs vacuum chambers as surroundings. So, this method is not suitable for large volume production (Won and Kim, 2019). In comparison to mechanical, chemical and electrical and electron or ion beam texturing processes, laser texturing has been found better with control in shape and size (Brown and Arnold, 2010).

LST has several advantages like non-contact (hence no tool wear) (Volchok et al., 2002), flexible processing (Gao et al., 2011) thus produce textures of required shape, size, and depth accurately on any material like metals (Daniel et al, 2003, von der Linde and Sokolowski-Tinten, 2000) semiconductors (Kelly et al., 1998, Sundaram and Mazur, 2002), ceramic (Geiger et al., 1998, Sudrie et al., 2001, Schaffer et al., 2004), polymers like polyether ether ketone (PEEK) and ultra-high-molecular-weight polyethylene (UHMWPE) (Riveiro et al., 2005) and biological tissues (Konig, 2002). Moreover, laser texturing provides a unique balance of texture precision and large-scale production, (Mucklich et al., 2006, Sun et al., 2007, Huang et al., 2010 and Kurselis et al., 2012) and has high efficiency compared to any other texturing processes (Singh and Harimkar, 2012). Moreover, being a material ablation process, laser technology enhances the mechanical and chemical properties of the surface (Obergfell et al., 2003, Mahmoudi et al., 2010, Iturralde, 2013). Laser surface texturing does not affect environment

and produces textures in less time period (Etsion et al., 1999, Etsion, 2010). The limitations of laser texturing are that it produces only negative type textures. For high melting point materials like platinum and tungsten, laser texturing cannot be efficient to engrave the material. Laser beam heat can affect the textured surface and cause variations in its metallurgical properties (Shamsul Baharin et al., 2016).

2.6 Research gap

Based on the literature review, the outlined key gaps are, a less effort has been made on texture distribution and optimum area density and texture depth of parallel sliding contacts for improved film thickness and frictional coefficient while considering mass conservative cavitation condition, couple-stress, and mixed lubrication conditions. No/limited work related to numerical analysis of multi scale textures effect on the tribological performance considering couple-stress, mass conservative cavitation condition, and mixed lubrication conditions has been observed in the literature survey. Moreover, no numerical analysis is carried out on the multi-scale textured parallel slider to optimize the texture number along and across fluid flow and sliding surfaces by varying velocity and load. The effect of multi-scale texture location, and area density on the film thickness and friction coefficient has not yet been examined. As far as fabrication of textures, no/little work is done on AISI 1020 steel surfaces. The effect of laser pulse number and pulse frequency on the texture depth is not yet studied. Literature on multi-scale textures is limited to variation in texture shape but not on multi-scale textural area density and texture depth. A scarce amount of work was reported on the frictional coefficient and wear rate of multi-scale textures.

2.7 Research problem

Limited work has been reported on the variation of texture area density, depth and distribution of multi -scale textured sliding contacts. A thorough examination on the tribological behavior of multi-scale textured sliding contacts under various textural parameters is required. The tribological behavior of such multi-scale textured sliding contacts is still dramatic in nature, and meticulous examination of such textured surfaces under various textural parameters is still required. The present research work addresses the design and development multi-scale textured sliding contacts and its tribological investigation under different operating conditions.

2.8 Research hypothesis

It is believed that single scale textures sliding contacts produce better film pressure when textural parameters like area density, texture depth are optimized and texture distribution chosen correctly. The multi-scale textured surface can produce stable tribological performance as compared to single-scale textures at most of the loading conditions. It is expected that the textural parameters like texture distribution, texture number and area density of multi-scale textures show a prominent effect on the output parameters like frictional coefficient and wear rate at different loads and speeds.

2.9 Research objective

In view of the afore-mentioned literature, the objectives of present research work can be outlined as follows.

1. Development of numerical simulation to study the tribological performance of single-scaled textured sliding contact under mixed lubrication regime while considering mass-conservative cavitation condition and couple stress fluid condition.
2. Development of numerical simulation for determination of better size and distribution of multi-scale textured sliding contact under mixed lubrication regime while considering mass-conservative cavitation condition.
3. Fabrication of multi-scaled surface textures on AISI 1020 material under ambient conditions by laser ablation method.
4. Experimentations related to the impact of multi-scale textured sliding contact on the tribological performance under lubricated conditions.

2.10 Summary

The exhaustive literature review on different textural parameters is presented. The review has reported on the importance of surface textures, single-scale textures, multi shape textures and multi scale textures, and their tribological performance at different textural and operating parameters. This chapter also discussed on the fabrication methods of surface textures. The detailed procedure of numerical development of single-scale textures and numerical analysis of single-scale textures by varying textural parameters considering the effect couple stress of the lubricant is discussed in chapter 3.

Chapter 3

Tribological performance of single-scale textured parallel sliding contact under mixed lubrication condition by considering mass conservation condition and couple-stress parameter

In this chapter, numerical simulations are conducted to study the impact of various textural parameters on tribological performance of single-scale textured parallel sliding contacts under mixed lubrication regime considering mass conservative cavitation condition. Moreover, the effect of surface roughness, slider velocity and fluid couple stress is studied. The tribological performance is calculated in terms of minimum film thickness, frictional coefficient, and hydrodynamic load percentage. In mixed lubrication regime, although the total load is supported by the fluid film and asperity contacts, it is beneficial to obtain more hydrodynamic load support than asperity load support in order to achieve better tribological performance. In the present analysis, hydrodynamic load percentage is evaluated to characterize the hydrodynamic load support of textured sliding contact.

3.1 Single-scale texture modelling and distribution

This sub-section deals with the texture placement on an imaginary unit cell and equations involved in calculating texture area density. The textures are modelled by using the center of the unit cell as the texture center as shown in Fig. 3.1. (c). Textures are distributed uniformly and schematic representation of the parallel and zig-zag distributions of triangular textures is shown in Fig. 3.1.

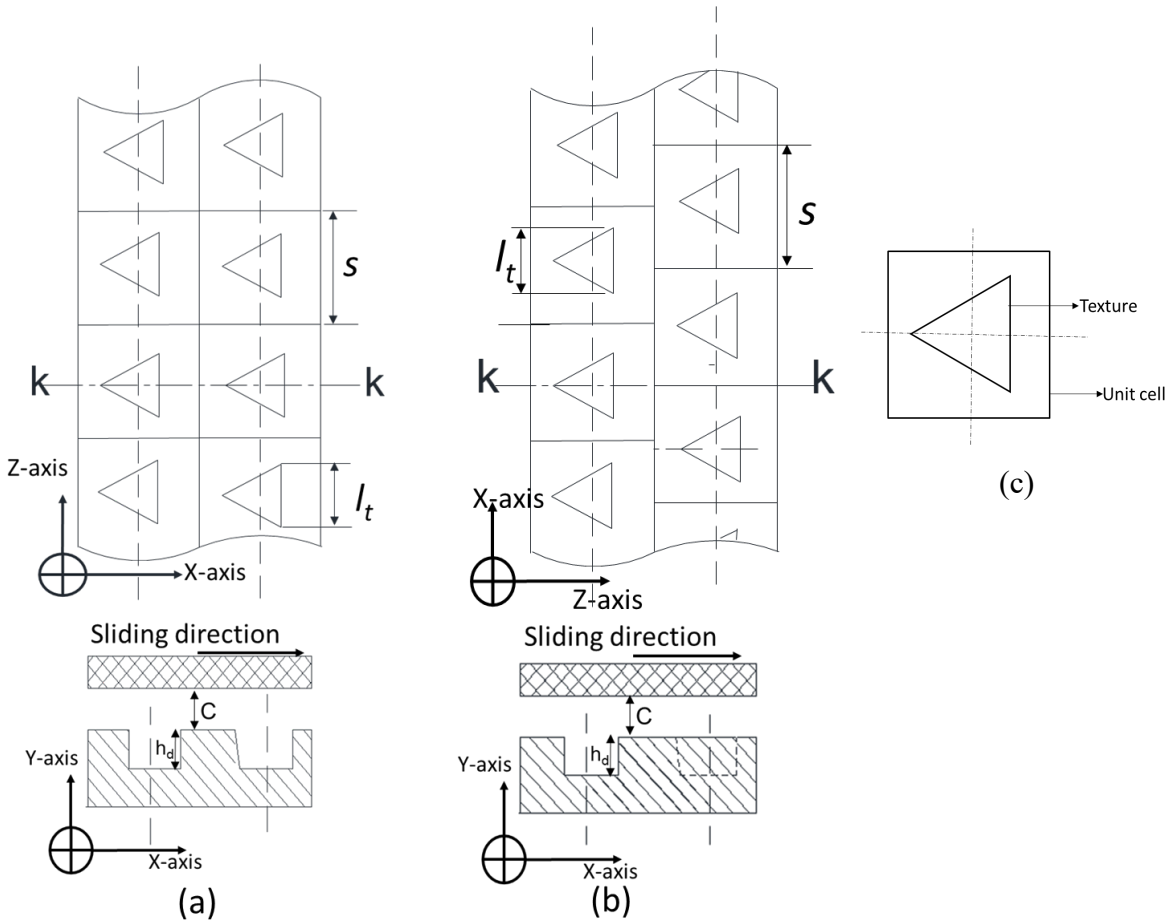

Fig. 3.1. Top view and front view of triangular textures in (a) Parallel distribution (b) Zigzag distribution (c) Unit cell.

Similarly, elliptical textures are arranged with minor axis half of major axis. The shape and size of textures placed inside the unit cell vary with the area density according to the equation:

$$Ad = \begin{cases} \dfrac{\sqrt{3}\, l_t^{\,2}}{4s^2} & \text{for triangular textures} \\ \dfrac{\pi\, l_e^{\,2}}{8s^2} & \text{for elliptical textures} \end{cases} \tag{3.1}$$

Where Ad is area density, l_t is the base length of triangular texture, l_e is the major axis length of elliptical texture, and s is unit cell length. The film thickness (h) between two interacting surfaces is obtained by the equation,

$$h = \begin{cases} C + h_d & \text{over the texture} \\ C & \text{elsewhere} \end{cases} \tag{3.2}$$

Where C is minimum film thickness and h_d is texture depth.

3.2 Governing equations

In general, there are several different types of lubrication regimes for lubricated sliding contacts, such as hydrodynamic, mixed, and boundary lubrication regime. A sliding contact is said to be in hydrodynamic lubrication, if the fluid enters in between the sliding contacts through the micro-wedge effect and supports the whole applied normal load. However, when speeds are low or loads are high causes the fluid film to be interrupted by the asperities between the surfaces. This asperity interaction generates certain pressure. This asperity pressure in addition to hydrodynamic pressure supports the applied normal load and the type of lubrication regime can be called as mixed lubrication regime. In boundary lubrication regime most of the applied normal load is supported by asperities. A modified Reynolds equation is used to evaluate the average hydrodynamic pressure, while the asperity contact model is used to determine the asperity pressure. The models used in the present work are discussed in the following sections.

3.2.1 Reynolds equation

This sub-section deals with the equations involved in calculating hydrodynamic pressure developed between parallel sliding contacts during sliding. In most tribo-component pairs, one surface is stationary and the other moves as shown in Fig 3.2. For these applications, the iso-viscous, incompressible, steady-state, 2D Reynolds equation is useful in predicting the pressure distribution (Khonsari, 2013) and the equation is :

$$\frac{\partial}{\partial x}\left(\frac{h^3}{12\mu}\frac{\partial p}{\partial x}\right)+\frac{\partial}{\partial z}\left(\frac{h^3}{12\mu}\frac{\partial p}{\partial z}\right)=\frac{U}{2}\frac{\partial h}{\partial x} \tag{3.3}$$

By including couple-stress parameter, the modified Reynolds equation according to Sharma et al (2016) is given by:

$$\frac{\partial}{\partial x}\left(\frac{f(h,l)}{\mu}\frac{\partial p}{\partial x}\right)+\frac{\partial}{\partial z}\left(\frac{f(h,l)}{\mu}\frac{\partial p}{\partial z}\right)=6U\frac{\partial h}{\partial x} \tag{3.4}$$

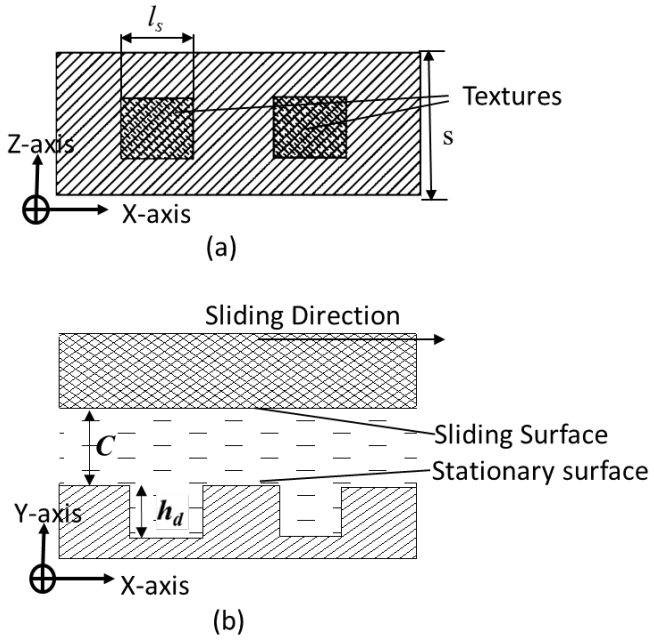

Fig. 3.2. Schematic of textured parallel sliding contacts (a) top view (b) front view.

Where $f(h,l)=h^3-12l^2\left\{h-2l\tanh\left(\frac{h}{2l}\right)\right\}$, U is the velocity of slider, μ is the viscosity of fluid, h is the film thickness of fluid, l is the couple-stress parameter of fluid, and p is the hydrodynamic pressure. The fluid flow is considered to be laminar and no slip condition prevails. The textured surface is considered as stationary surface and smooth surface is moving with velocity of 'U' m/s. The frame of reference coordinate system is taken on the textured surface. Due to this consideration, the change of film thickness with respect to time can be neglected in the Reynolds equation. By adopting JFO cavitation condition (Vijayaraghavan and Keith, 1989)

$$p=\begin{cases} p_c+g\alpha\ln(\phi) & at\ \ \phi\geq 1 \\ p_c\ at\ \ \phi<1 \end{cases} \tag{3.5}$$

where $\phi=\rho/\rho_c$, in the *Eq. (3.4)*, the modified Reynolds equation is obtained as

$$\frac{\partial}{\partial x}\left(\frac{g\alpha f(h,l)}{12\mu}\frac{\partial\phi}{\partial x}\right)+\frac{\partial}{\partial z}\left(\frac{g\alpha f(h,l)}{12\mu}\frac{\partial\phi}{\partial z}\right)=\frac{U}{2}\frac{\partial(\phi h)}{\partial x} \tag{3.6}$$

Where α is the bulk modulus of fluid, p is the hydrodynamic pressure, p_c is the cavitation pressure, ρ is the density of oil at hydrodynamic pressure, ρ_c is the density of oil at cavitation pressure, ϕ is the fractional film content, and g is the switch function of value, $g=\begin{cases}1 & if\ \ \phi\geq 1\\ 0 & if\ \ \phi<1\end{cases}$.

Furthermore, by considering the effect of surface irregularities according to Patir and Cheng

(1978), the *Eq. (3.6)* becomes

$$\frac{\partial}{\partial x}\left(\frac{g\alpha f(h,l)\varphi_x}{12\mu}\frac{\partial\phi}{\partial x}\right)+\frac{\partial}{\partial z}\left(\frac{g\alpha f(h,l)\varphi_z}{12\mu}\frac{\partial\phi}{\partial z}\right)=\frac{U\varphi_c}{2}\frac{\partial(\phi h)}{\partial x}+\frac{\sigma U}{2}\frac{\partial\varphi_s}{\partial x} \tag{3.7}$$

Here φ_x, φ_z, and φ_s are flow factors.

3.2.2 Flow factors calculation

In the present study, the surface pattern parameter, γ is considered as one i.e., circular surface irregularity pattern and the corresponding corrective factors φ_x, φ_z, and φ_s can be computed according to Patir and Cheng's model (1978). The contact factor φ_c is calculated from Wu and Zhengs model (1989) by assuming surface irregularities have Gaussian shaped heights. By considering γ =1, the equations of flow factors and contact factor can be deduced as follows:

$$\varphi_x=\varphi_z=1-0.9e^{-0.56H} \tag{3.8}$$

$$\varphi_s=\begin{cases}1.899H^{0.98}e^{-0.92H+0.05H^2} & H\le 5\\ 1.126e^{-0.25H} & H>5\end{cases} \tag{3.9}$$

$$\varphi_c=\begin{cases}e^{-0.6912+0.782H-0.304H^2+0.0401H^3} & 0\le H<3\\ 1 & H\ge 3\end{cases} \tag{3.10}$$

Where H is surface roughness factor *(h/σ)* where σ is combined root mean square (RMS) value of surface irregularities of two surfaces. When $H\rightarrow\infty$, then φ_x, $\varphi_z\rightarrow 1$ and $\varphi_s\rightarrow 0$, then the *Eq. (3.7)* can be reduced to generalized Reynolds equation for smooth surfaces as in *Eq.(3.6)*.

3.2.3 Asperity pressure calculation

The present sub-section deals with the equations involved in calculating hydrodynamic pressure developed between parallel sliding contacts during sliding, asperity contact pressure. Whether the regime is in mixed or hydrodynamic lubrication can be identified by the surface roughness parameter *(H)*. If $H\ge 4$ then the regime is considered as hydrodynamic lubrication, and if $1<H<4$ then the regime is considered as mixed lubrication. In mixed lubrication, the applied pressure is supported by hydrodynamic pressure (p) and asperity contact pressure (p_a). The hydrodynamic pressure is calculated by solving the *Eq. (3.5)* and *Eq. (3.3)*, whereas, the contact pressure is found by Greenwood and Tripp equation (1970):

$$p_a=K'E'F_{2.5}(H) \tag{3.11}$$

Where $K'=\frac{16\sqrt{2}}{15}\pi(N\beta\sigma)^2\sqrt{\frac{\sigma}{\beta}}$ (3.12)

Here K' is a function of RMS of surface irregularities (σ), by keeping all other parameters

constant. According to that, the equation is (Hu et al., 1994),

$$K' = 5.319\times10^{10}\times\sigma^{2.5} \tag{3.13}$$

And the value of $F_{2.5}(H)$ can be found by approximating asperity height to be in Gaussian distribution with film thickness and the related equation can be found in Hu et al (1994):

$$F_{2.5}(H) = \begin{cases} A(4-H)^{Z} & \text{if } H < 4 \\ 0 & \text{otherwise} \end{cases} \tag{3.14}$$

Where, $\sigma = \sqrt{\sigma_1^2 + \sigma_2^2}$ is the equivalent RMS surface roughness, $E' = \dfrac{E_1 E_2}{\left(E_1\left(1-\nu_2^{\,2}\right)+E_2\left(1-\nu_1^{\,2}\right)\right)}$ is the equivalent elastic modulus. σ_1, σ_2, ν_1, ν_2, E_1, and E_2 are all the input parameters like RMS surface roughness, Poisson's ratio and young's modulus of two surfaces respectively, N is the asperity density, β is the radius of the asperity peaks.

3.3 Numerical simulation

Numerical code is developed in MATLAB to calculate hydrodynamic pressure, asperity pressure by considering appropriate input parameters. The values of input parameters used in this numerical solution are shown in Table 1.1. *Eq. (3.7)* is discretized using the central finite difference method and solved by the Gauss-Seidal iterative scheme by satisfying appropriate boundary conditions.

Due to texture interaction, periodic boundary condition i.e., *p(X, Z=0)=p(X, Z=Lg)* is considered along X-axis and atmospheric pressure boundary condition is considered along Z-axis, for both texture distributions as shown in the Fig. 3.3.

Table 3.1. Input Parameters used in numerical simulation of single-scaled textured sliding contacts.

S. No.	Name of the Input Parameter	Value	Units
1	Velocity of the slider (U)	2,4,6,8	m/s
2	Texture depth (h_d)	0– 24	µm
3	Area density	0.1, 0.2, 0.3.	-
4	Applied pressure (p_l)	0.25	MPa
5	Atmospheric pressure (p_{atm})	0.101325	MPa
6	Viscosity of fluid, (μ) (Gu et al., 2016)	0.01	Pa s
7	Bulk modulus of fluid (α) (Gu et al., 2016)	1.69	GPa
8	Young's modulus of sliding surface (E_1) (Tomanik, 2013)	250	GPa
9	Young's modulus of stationary surface (E_2) (Tomanik, 2013)	120	GPa
10	Cavitation pressure (p_c) (Gu et al., 2016)	$0.9x10^5$	Pa
11	Poisson's ratio of sliding surface (v_1) (Tomanik, 2013)	0.3	-
12	Poisson's ratio of stationary surface (v_2) (Tomanik, 2013)	0.3	-
13	Combined RMS surfaces roughness (σ)	0-1.5	µm
14	*A (*Hu et al., 1994*)*	$4.4068 x10^5$	-
15	*Z (*Hu et al., 1994*)*	6.804	-
16	Boundary frictional coefficient (C_f) (Tomanik, 2013)	0.12	-
17	Length of the slider (Lg)	4	mm
18	Area of the slider (a)	8	mm^2

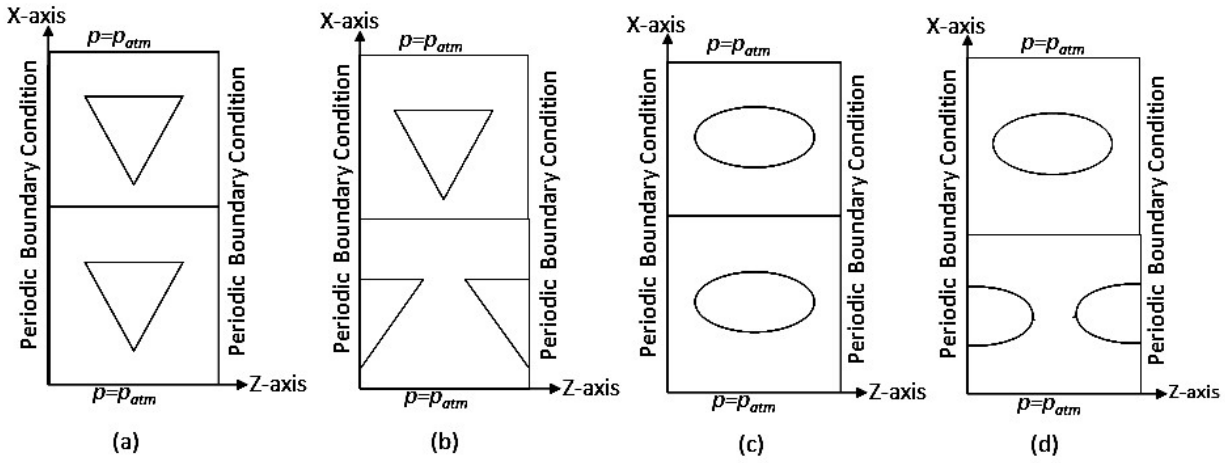

Fig. 3.3. Boundary conditions.

At each node, the fractional film content of the fluid is calculated by *Eq. (3.7)*. Then hydrodynamic pressure, p is calculated by *Eq. (3.5)*. Pressure convergence criteria chosen to calculate the hydrodynamic pressure is given as: $\sum_{i=1}^{nx}\sum_{j=1}^{nz}\left|\frac{p(i,j)-p(i,j)_{old}}{p(i,j)}\right| \leq 1\times10^{-5}$

$p(i,j)$, $p_{old}(i,j)$ are the hydrodynamic pressures at a certain node,(i,j) at current and previous pressure convergence iterations respectively.

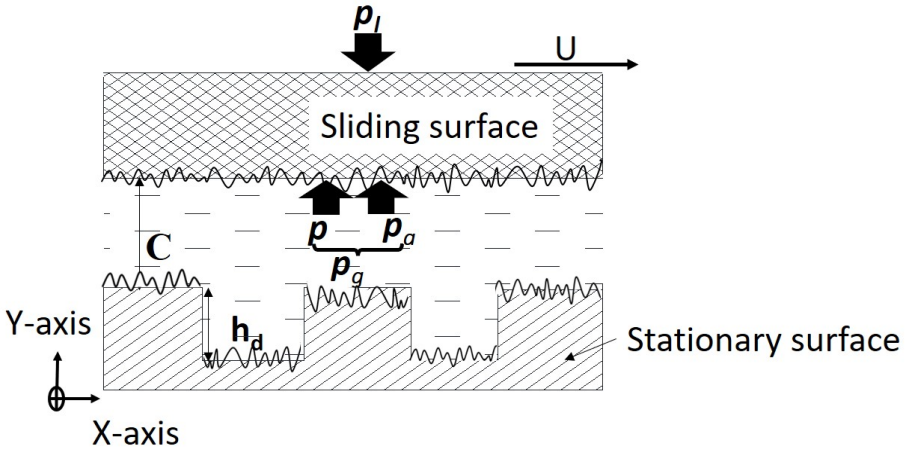

Fig. 3.4. Pressure balance diagram of textured parallel sliding contact.

After determining the hydrodynamic pressure p by using *Eq. (3.5)*, the asperity pressure, p_a is calculated from *Eq. (3.11)*. Then, the total generated pressure, p_g is determined, which is the sum of hydrodynamic and asperity contact pressures. This total generated pressure in the fluid is balanced for an error convergence of 10^{-3} with the total applied pressure, p_l on the sliding contact. The pressure balance diagram is shown in Fig.3.4. The related pressure balance criterion is shown below

$$\left|\frac{p_e - p_{g,k}}{p_e}\right| \leq 1\times10^{-3}$$

Here, $p_{g,k}$ is the total generated pressure at k^{th} iteration. The flow chart of the developed numerical code is shown in Figure 3.5.

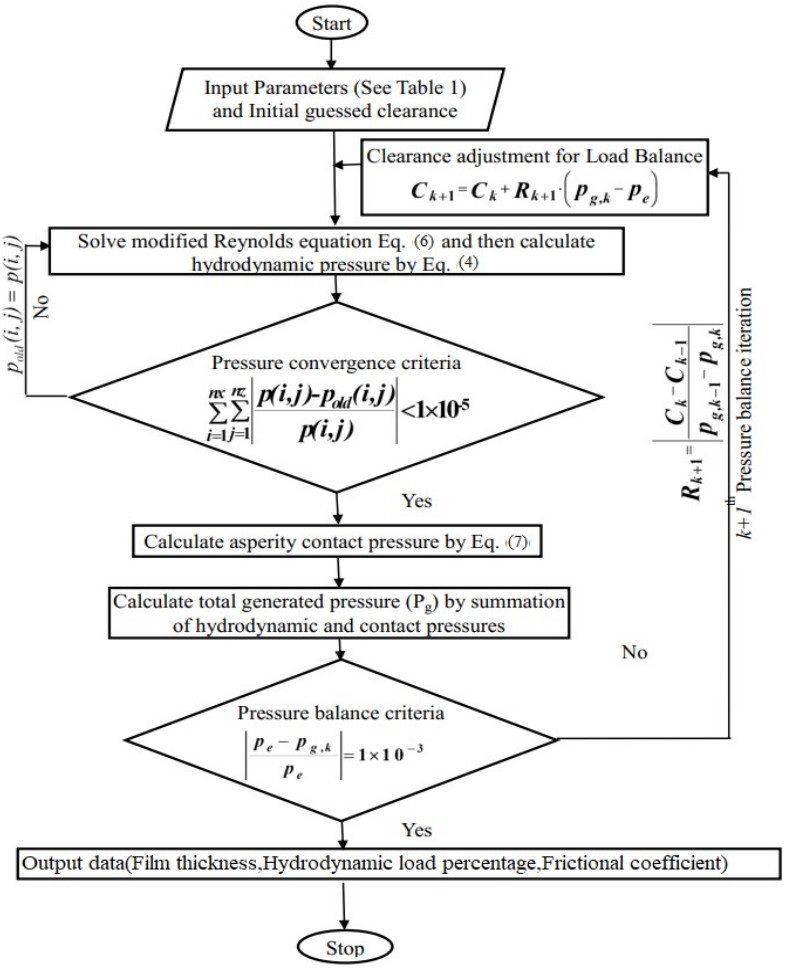

Fig. 3.5. Flow chart of numerical code.

3.4 Performance parameters

Here, the equations involved in calculating performance parameters like, minimum film thickness, hydrodynamic load percentage, and frictional coefficient are discussed. The performance parameters are calculated after balancing the calculated pressure with applied load pressure.

3.4.1 Minimum film thickness

Once the load balance criterion is satisfied, the minimum film thickness is calculated by:

$$C_{k+1} = C_k + Re_{k+1}\left(p_{g,k} - p_l\right) \tag{3.15}$$

$$Re_{k+1} = \left|\frac{C_k - C_{k-1}}{p_{g,k-1} - p_{g,k}}\right| \tag{3.16}$$

Here C_k and C_{k+1} the minimum film thickness in old and new iterations respectively, Re_{k+1} is relaxation factor for new iteration.

3.4.2 Hydrodynamic load percentage

The following equation is used to calculate the hydrodynamic load percentage

$$Hydrodynamic\ load\ percentage = \frac{p}{p_l} \times 100 \tag{3.17}$$

Here p is hydrodynamic pressure, p_l is the applied load pressure.

3.4.3 Frictional coefficient

Once the desired hydrodynamic pressure and asperity pressure is obtained based on the exerted pressure, the frictional coefficient is calculated by the following equation

$$\text{Frictional coefficient} = \frac{F_{tot}}{p_l . a} \tag{3.18}$$

Where, F_{tot} is the total friction force, which is calculated from the equations given below;

$$F_{tot} = F_h + F_a \tag{3.19}$$

$$F_h = \iint \left\{ \frac{\mu U}{h} (\varphi_f + \varphi_{fs}) + \varphi_{fp} \frac{1}{2} \frac{\partial p}{\partial x} \left(h - 2l \tanh \frac{h}{2l} \right) \right\} dx.dz \tag{3.20}$$

$$F_a = C_f \iint p_a . dx.dz \tag{3.21}$$

Herein, a is area of the considered contact surface, F_h, and F_a are friction forces due to fluid and asperity contacts respectively. By assuming isotropic roughness φ_f, φ_{fs}, and φ_{fp} are the corrective factors for viscous friction and approximated as follows (Patir and Cheng, 1979)

$$\phi_{fp} = 1 - 1.40 e^{-0.66H} \tag{3.22}$$

$$\phi_{fs} = \begin{cases} 11.1 H^{2.31} e^{-2.38H + 0.11H^2} & 0.5 < H < 7 \\ 0 & H > 7 \end{cases} \tag{3.23}$$

$$\phi_f = \begin{cases} \frac{35}{32} z_1 \left\{ (1 - z_1^2)^3 \ln \frac{z_1 + 1}{\in^*} + \frac{1}{60} \left[-55 + z_1 (132 + z_1 (345 + z_1 (-160 + z_1 (-405 + z_1 (60 + 147 z_1))))) \right] \right\} & \text{if } H \le 3 \\ \frac{35}{32} z_1 \left\{ (1 - z_1^2)^3 \ln \frac{z_1 + 1}{z_1 - 1} + \frac{z_1}{15} \left[66 + z_1^2 (30 z_1^2 - 80) \right] \right\} & \text{if } H > 3 \end{cases}$$

(3.24)

Here, $z_1 = h/3$, $\in^* = \in/3\sigma$ and $\in = \sigma/100$. When $H \to \infty$, then φ_f, and $\varphi_{fp} \to 1$ and $\varphi_{fs} \to 0$, then the *Eq. (3.20)* can be reduced to generalized friction forces due to fluid between smooth surfaces.

3.5 Results and Discussions

Prior to the detailed explanation of textural effects on the tribological performance of parallel sliding contact, mesh sensitivity analysis and validation of the numerical model are performed.

3.5.1 Mesh sensitivity analysis

Prior to the numerical analysis, the mesh sensitivity study was performed to decide the appropriate mesh grid size to avoid numerical instability of the solution. The mean hydrodynamic pressure is estimated for a pressure convergence criterion of 10^{-5} for different mesh nodes as shown in Figure 3.6. It can be observed that there is not much deviation in mean hydrodynamic pressure value after 104 and 84 nodes in *z*- and *x*-directions respectively. Therefore, a mesh grid size ($nx \times nz$) of 84 × 104 is chosen for further analysis.

3.5.2 Validation of the numerical model

The numerical simulations were performed to validate the present numerical model with the previously available results. The present code is simulated with the conditions of Gu et al. (2016) and the hydrodynamic load percentage calculated and compared with their result. The numerical simulation results indicate that the developed numerical model agreed well with the work of Gu et al. (2016) as shown in Fig. 3.7. Therefore, the developed model is sufficiently accurate enough and error-free.

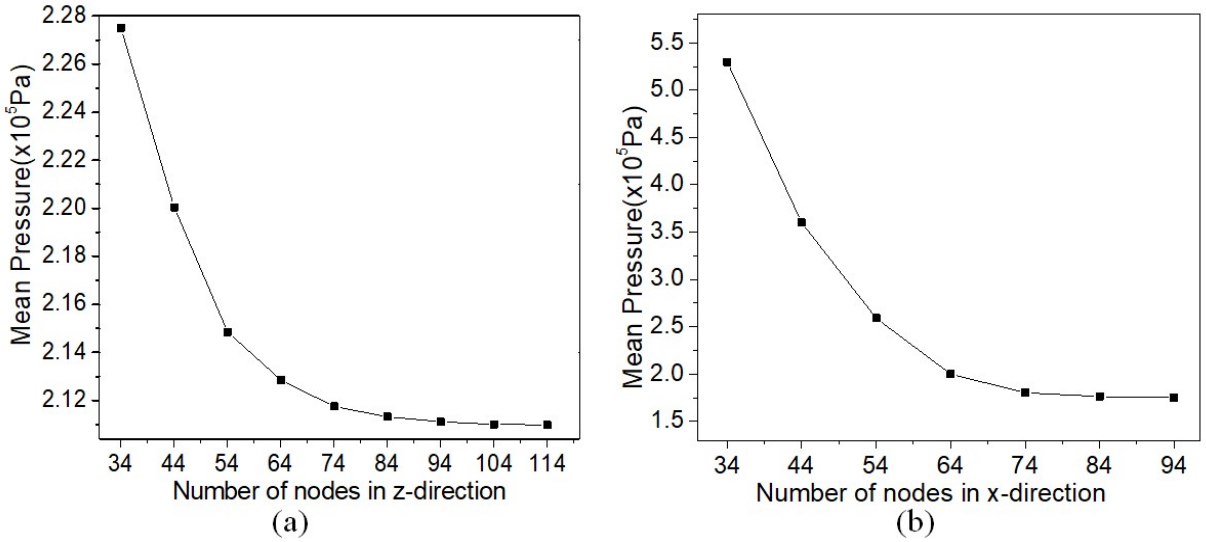

Fig. 3.6. Mesh sensitivity analysis of a triangular textured cell (a) *z*- direction (b) *x*- direction.

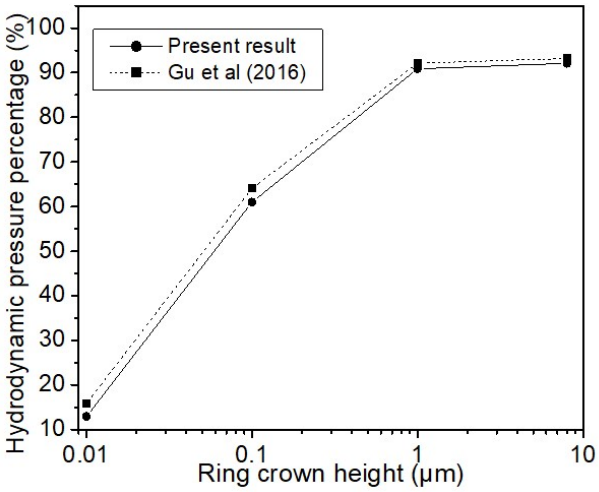

Fig. 3.7.Validation of hydrodynamic load percentage with the previously available result (Gu et. al., 2016).

3.5.3 Effect of textural and couple-stress parameters on tribological performance

In this section, the effect of textural parameters on tribological performance parameters under mixed lubrication condition is studied. The textural parameters considered in the analysis are texture shape, size, depth, and distribution. The tribological performance parameters are minimum film thickness, hydrodynamic load percentage, and frictional coefficient. The effect of the couple-stress parameter on tribological performance parameters is also studied.

The effect of texture depth on minimum film thickness, frictional coefficient, and hydrodynamic load percentage for different texture shapes and distribution is shown in Figure 3.8. As shown in Figure 3.8(a), it can be observed that from un-textured to the texture depth of 6 μm, there is shift of lubrication regime from mixed to hydrodynamic. This can also be observed from Figure 3.8(b). Hence, there is drastic decrease in frictional coefficient due to the absence of asperity contacts. However, with texture depth >6 μm, again contact enters into mixed lubrication regime. Hence, there is steep rise in frictional coefficient as shown in Figure 3.8(c). Here, elliptical textures produce better minimum film thickness at all texture depths as compared to triangular textures. This can be attributed to higher pressure interaction between adjacent elliptical textures than triangular textures as shown in Figure 3.9.

As shown in Figure 3.8(a) and (c), elliptical texture depth of 3 μm gives 268% higher film thickness and 74% lower frictional coefficient as compared to the un-textured surface. The film thickness and frictional coefficient of deeper textures are almost equal to the un-textured. The reason for this can be solved by considering textures similar to Rayleigh's step bearing. Rayleigh's theory states that when step height to fluid film thickness ratio exceeds the value of

4.4, the step height cannot produce the hydrodynamic effect. Hence, the textured surface acts as un-textured surface at one point of increased texture depth. For elliptical textures, the texture distribution has little/no prominent effect on film thickness. This is due to the generation of equivalent pressure contour and peak pressure for both parallel and zigzag distribution which can be seen in Figure 3.10. However, in the case of triangular textures, zigzag distribution exhibits a slightly higher film thickness as compared to parallel distribution (see Figure 3.8(a)). This may be due to broader pressure contour and higher contour region of maximum pressure in zigzag distribution as compared to parallel distribution as shown in Figure 3.11.

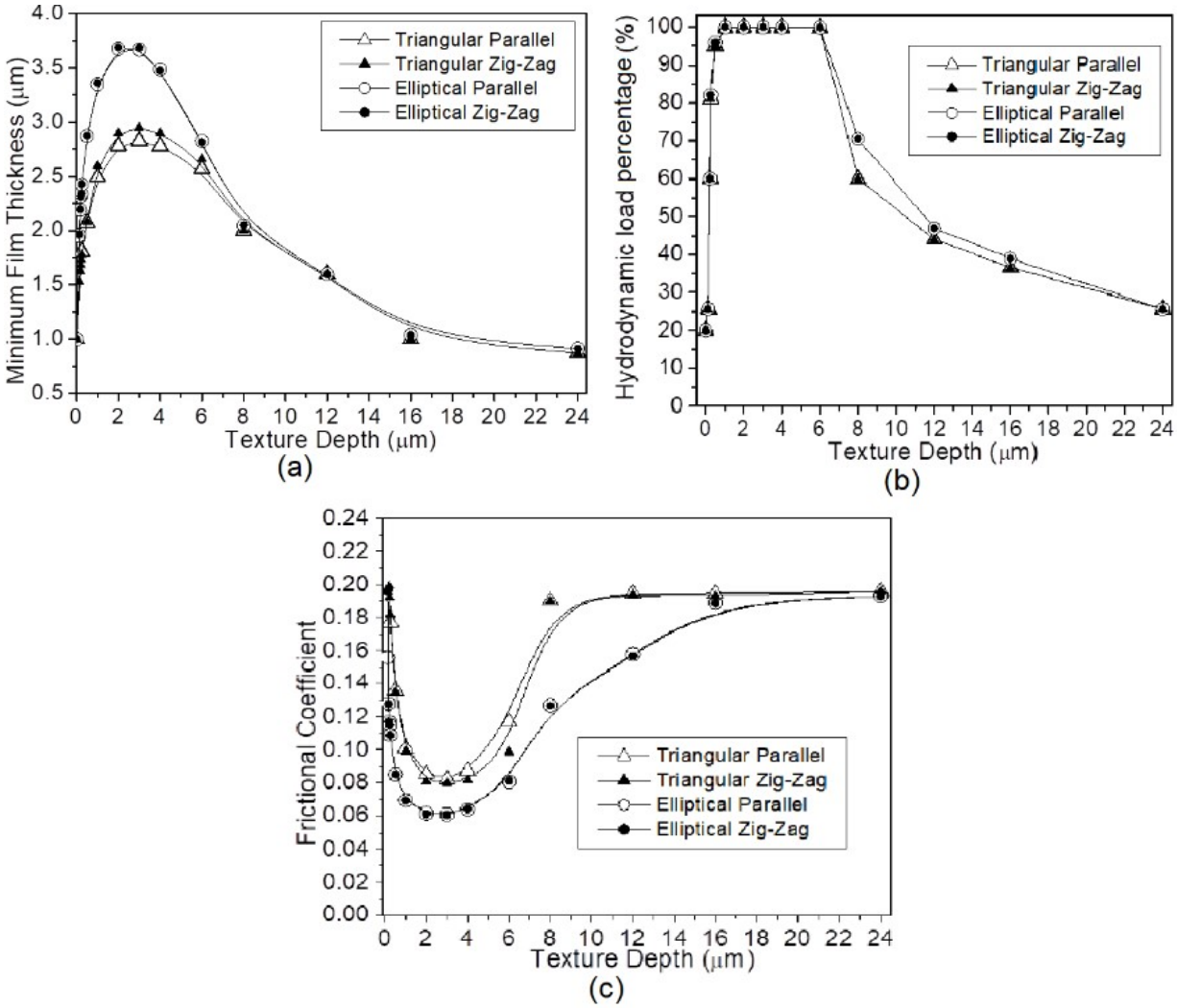

Fig. 3.8. Variation of (a) minimum film thickness (b) hydrodynamic load percentage and (c) frictional coefficient with texture depth at area density of 0.2, and velocity of 8 m/s.

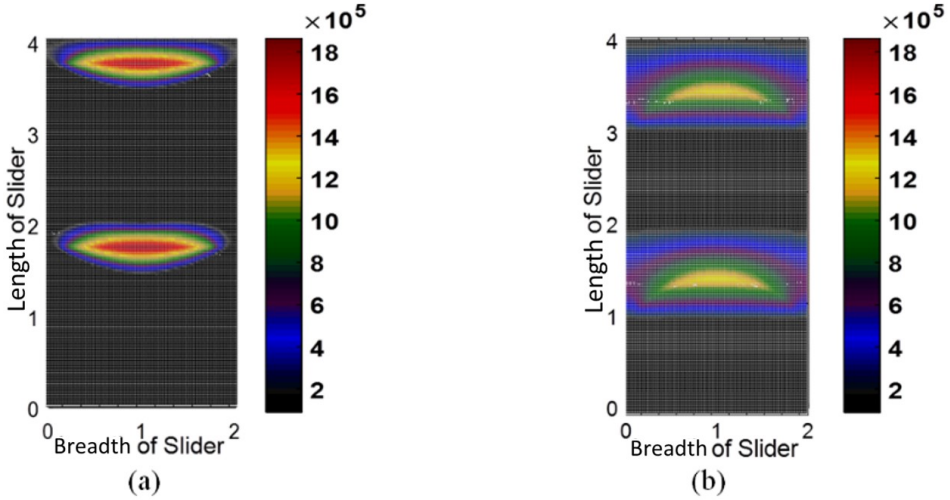

Fig. 3.9. Pressure contour for parallel distributed (a) triangular (b) elliptical textures.

For elliptical textures, the texture distribution has little/no prominent effect on film thickness. This is due to the generation of equivalent pressure contour and peak pressure for both parallel and zigzag distribution which can be seen in Fig. 3.10. However, in the case of triangular textures, zigzag distribution exhibits a slightly higher film thickness as compared to parallel distribution (see Fig. 3.8(a)). This may be due to broader pressure contour and higher contour region of maximum pressure in zigzag distribution as compared to parallel distribution as shown in Fig. 3.11.

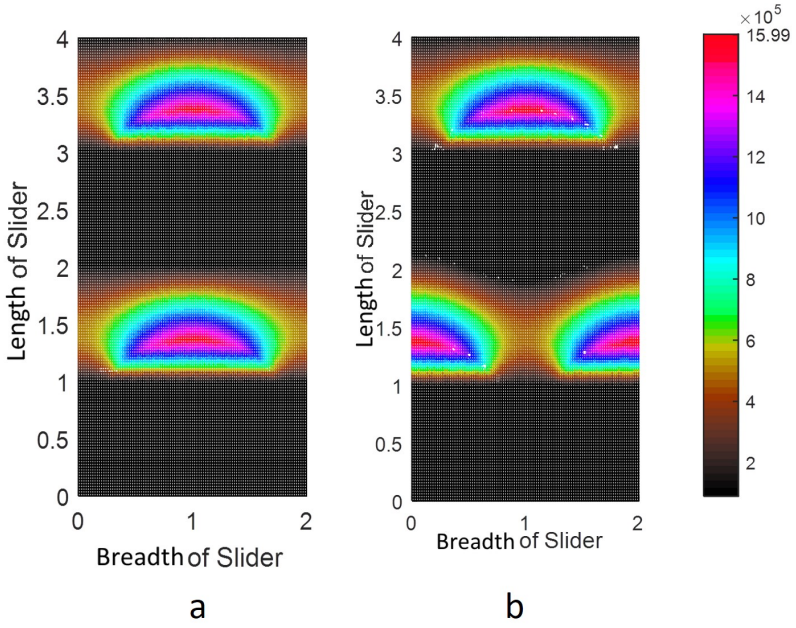

Fig. 3.10. Pressure contours of elliptical textures of (a) parallel (b) zigzag distributions.

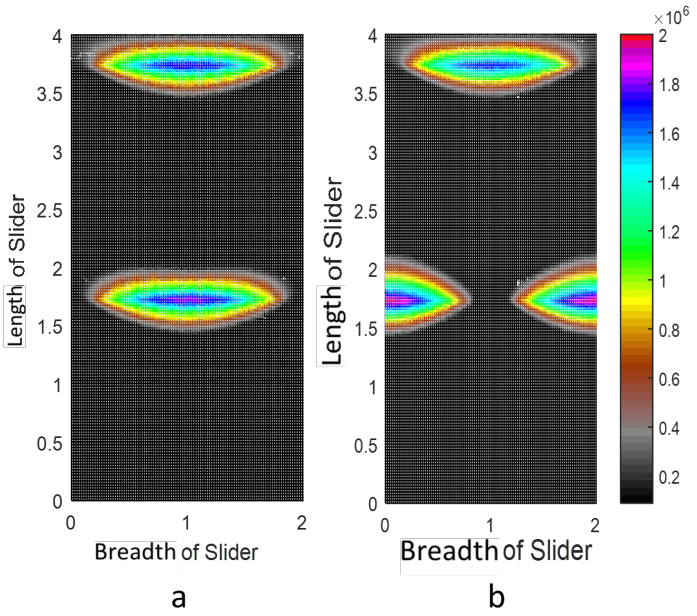

Fig. 3.11.Pressure contours of triangular textures of (a) parallel (b) zigzag distributions.

It is inferred from the preceding study that better tribological performance is obtained for a texture depth of around 3 μm (see Figure 3.8). Therefore, in further analysis, the texture depth is considered as 3 μm. The area density effect on minimum film thickness as well as the frictional coefficient for different texture shapes and distribution are shown in Figure 3.12. It can be observed from Figure 3.12(a) that better tribological performance is obtained with increasing area density. This can be attributed to the restriction of fluid flow by longer texture edges at higher area densities. This generates higher hydrodynamic pressure which leads to higher minimum film thickness. Hydrodynamic lubrication regime prevails at surface roughness parameter, $H > 4$, i.e., for film thickness $h > 2.52$ μm which is shown as dashed line in Figure 3.12(a). It can be observed that at an area density of 0.1, lubrication regime is in mixed lubrication. As the area density increases, the lubrication regime changes from mixed to hydrodynamic lubrication. Therefore, it can be seen from Figure 3.12(b) that as area density increases, there is reduction in frictional coefficient.

In the present work, better tribological performance is observed at an area density of 0.3 (refer Figure 3.12). Moreover, the effect of distribution is negligible on the tribological performance. Hence zigzag distribution is considered for further analysis. From the literature (Ma et al., 1996), it has been inferred that the surface roughness effect on tribological performance depict a comparable trend with the area density. Therefore, the present subsection deals with the effect of surface roughness on tribological performance at an area density of 0.3 (refer Figure 3.13).

It has been observed that for a surface roughness value $\sigma < 0.9$, the hydrodynamic pressure predominates (refer Figure 3.13(b)) and higher film thickness is observed for the surface roughness value of up to 0.3 and then decreases as surface roughness increases and vice-versa for frictional coefficient. However, the change in film thickness and frictional coefficient is marginal (see Figure 3.13(a) and (c)). For surface roughness values, $\sigma > 0.9$, asperity pressure dominates (refer Figure 3.13(b)), because at larger surface asperities, the fluid cannot sustain between the contact zone and a direct asperity to asperity contact takes place. This leads to higher frictional coefficient (see Figure 3.13(c)).

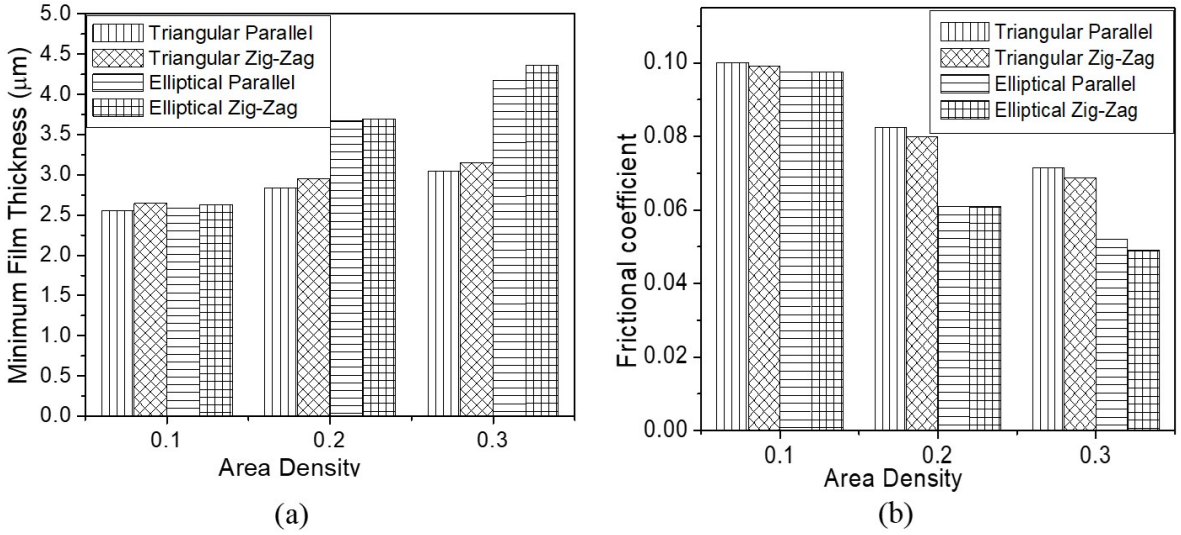

Fig. 3.12. Variation of (a) minimum film thickness and (b) frictional coefficient with area density for velocity of 8 m/s, surface roughness of 0.63 μm.

In the further analyses, the constant area density and surface roughness of 0.3 and 0.63 respectively, are considered. The effect of sliding velocity on tribological performance parameters is shown in Fig. 3.14. At lower velocities (i.e., less than 2 m/s), the contact undergoes mixed lubrication due to which there is reduction in minimum film thickness (refer Fig. 3.14(a)) and steep rise in frictional coefficient (refer Fig. 3.14(c)). Fig. 3.14(a) depicts those higher velocities (i.e., greater than 2 m/s) produces higher minimum film thickness for all texture shapes. This is due to the generation of more hydrodynamic load percentage and it is confirmed in Fig. 3.14(b) by hydrodynamic load percentage. However frictional coefficient increases due to higher shearing of fluid at higher velocities.

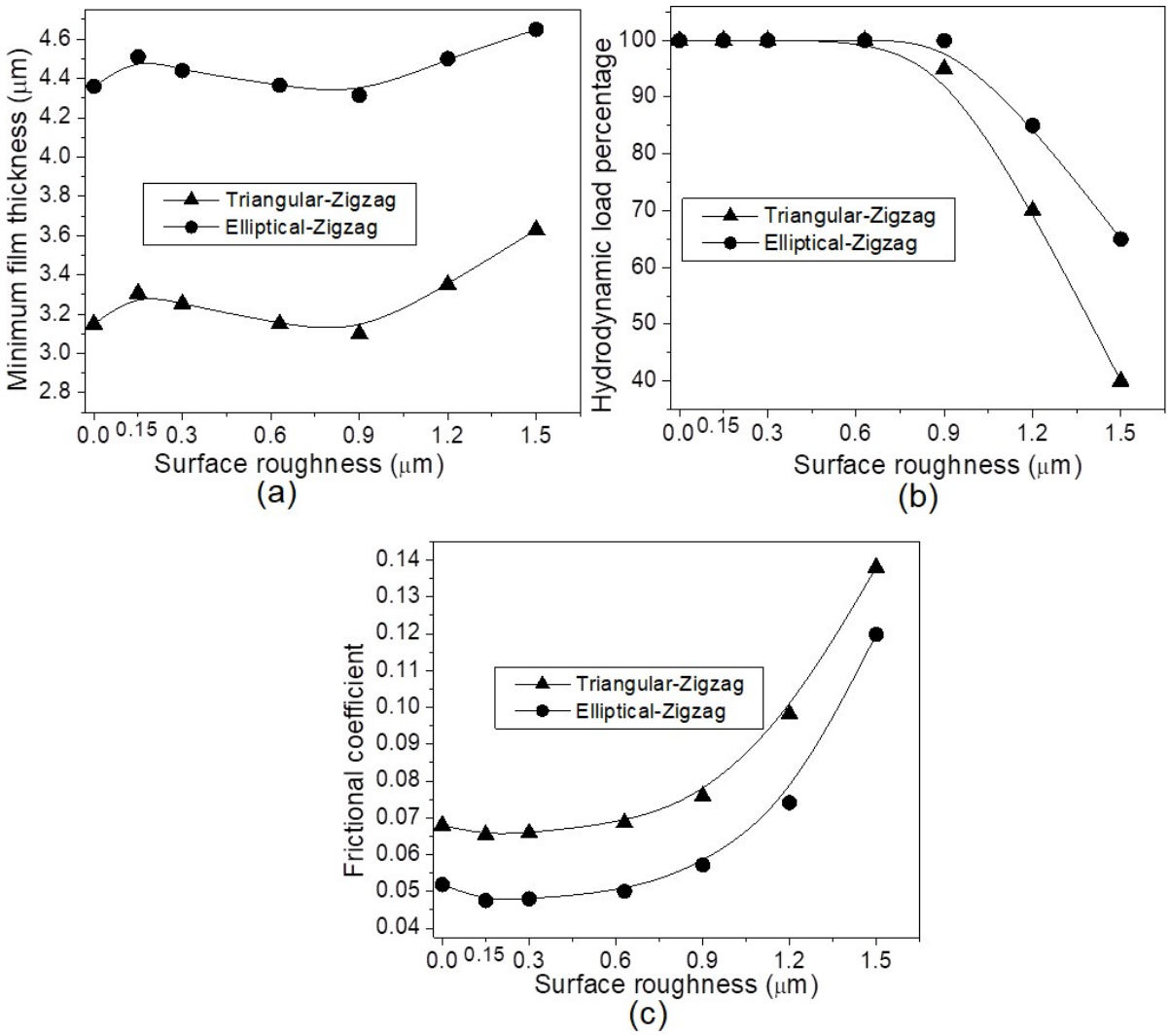

Fig.3.13. Variation of (a) minimum film thickness (b) hydrodynamic load percentage and (c) frictional coefficient with surface roughness for velocity of 8 m/s, texture depth of 3 μm and area density of 0.3.

In the subsequent analysis, tribological performance parameters were studied by considering the sliding velocity of 2 m/s at which minimum frictional coefficient has been observed. The couple-stress parameter effect on tribological performance in both textures is shown in Fig. 3.15. It can be observed that elliptical textures produce higher minimum film thickness as compared to triangular textures at all couple-stress parameter values. However, it is observed that the rate of change of minimum film thickness and the frictional coefficient with couple-stress parameter is high in triangular textures as compared to elliptical textures. As a whole, couple-stress parameter exhibits significant effect on the tribological performance parameters.

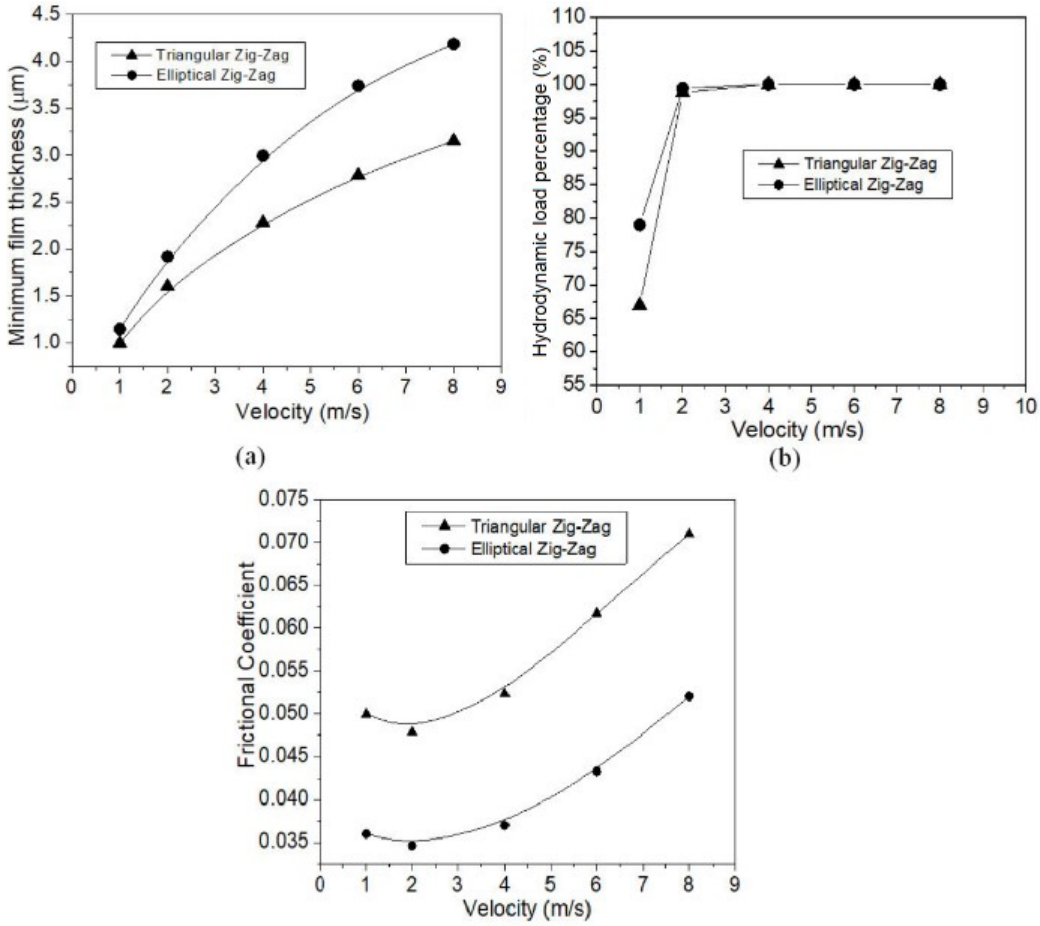

Fig.3.14. Variation of (a) Minimum film thickness (b) hydrodynamic load percentage and (c) frictional coefficient with velocity at texture depth of 3 μm, area density of 0.3 and surface roughness of 0.63 μm.

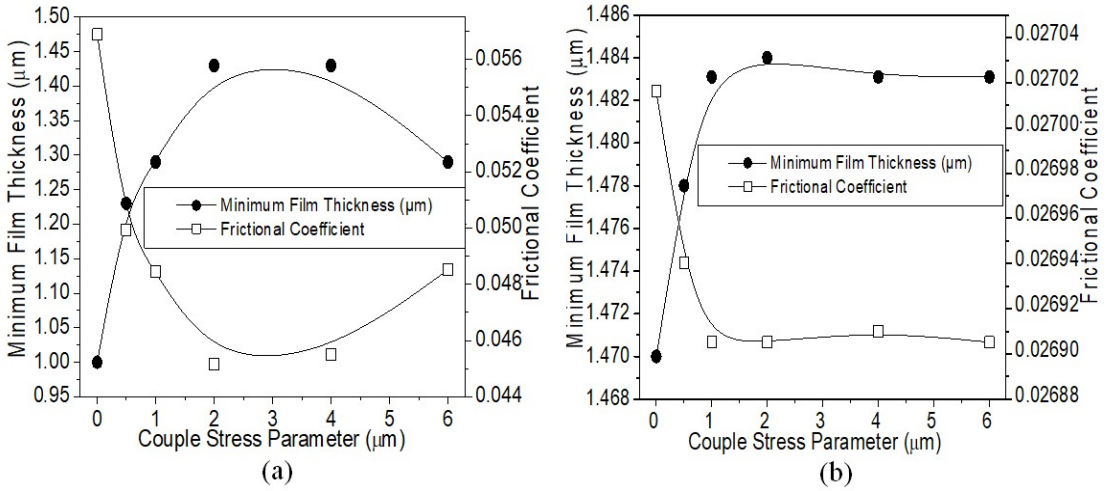

Fig. 3.15. Variation of minimum film thickness and frictional coefficient with couple-stress parameter ,*l* for (a) triangular and (b) elliptical textures at velocity of 2 m/s, texture depth of 3 μm and surface roughness of 0.63 μm.

3.6 Summary

In this chapter, a numerical model has been developed for single-scale textured parallel sliding contact under mixed lubrication regime adopting mass conserving JFO cavitation condition. To presume rough surface, models such as Patir-Cheng model and Greenwood Tripp model are solved for hydrodynamic pressure and asperity pressure, respectively. The model developed is validated with simulation results of previously available literature. The effect of textual area density, depth, distribution, velocity and couple-stress parameter on tribological parameters like minimum film thickness, hydrodynamic load percentage and frictional coefficient is studied.

The result indicates that the elliptical texture shape exhibits higher tribological performance as compared to triangular texture for all textural parameters. The effect of texture distribution is not significant on the tribological performance parameters. For surface roughness $\sigma < 0.9$ and $U > 2$ m/s, hydrodynamic pressure predominates due to which lower friction coefficient is obtained. Whereas, for surface roughness $\sigma > 0.9$ and $U < 2$ m/s, asperity pressure predominates and higher frictional coefficient is obtained. The couple-stress parameter has a positive effect on tribological performance for both textural shapes.

The single-scaled textured surfaces are subjected to reduced friction, at hydrodynamic lubrication regime. The textural parameters like area density, depth and distribution affects the tribological performance. To mitigate the frictional losses, under varying operating conditions, single-scaled textures are considered ineffective. Therefore, the idea of multi-scale textures is developed. But the performance of these multi-scale textures is affected by various textural parameters like area density, multi-scale textural position, and etc. In Chapter 4 a detailed tribological investigation is carried out by developing a numerical code on design of multi-scale textures to reduce frictional coefficient at different load and speed conditions.

Chapter 4

Tribological performance of multi-scale textured parallel sliding contacts under mixed lubrication regime by considering mass conservation cavitation condition and couple-stress parameter

In the previous chapter, the tribological performance of single-scale textured parallel sliding contacts by considering mixed lubrication regime and mass conservation condition is studied. The single-scaled textured surfaces produce better tribological performance only at specific operating conditions. However, in real time applications, a tribo-pair is operated under different load and speed conditions. Hence, there is a necessity to develop a textural surface which produces better tribological performance at varying operating parameters. To mitigate the frictional losses, under varying operating conditions, the idea of multi-scale textures is developed. Therefore, in Chapter 4 a detailed tribological investigation is carried out with the development of numerical code on multi-scale textures by varying textural parameters like area density, multi-scale textural position, and etc. to reduce frictional coefficient at different load and speed conditions. Moreover, the effect of fluid couple stresses on multi-scale textures is studied.

4.1. Multi-scale textures

From the literature (Syed and Sarangi, 2014, Segu and Hwang 2015, Segu and Hwang 2016, Uddin et al., 2017), it has been observed that elliptical and triangular texture shapes exhibit improved tribological characteristics. Therefore, the present analysis used these two different shapes of textures, namely, elliptical and triangular textures. In order to identify the better combination of multi-scale texture, the analysis has been carried out on various configurations, like elliptical shallow-elliptical deep, elliptical shallow-triangular deep, elliptical deep-triangular shallow and triangular shallow-triangular deep textures. The respective equations to

calculate the size of shallow and deep textures are shown in Table 4.1. The present analysis considered the minor axis length of elliptical texture as half of its major axis length.

Table 4.1 Equations of multi-scale textural parameters.

Texture Configuration	**Major axis length/ side length of texture**	**Texture depth of shallow and deep textures**	**Area density (A_d)**
Elliptical shallow and elliptical deep	$l_{e,s}=2\left[\sqrt{\frac{Lg.Br.A_d}{\pi n_s}}\right]$ $l_{e,d}=2\left[\sqrt{\frac{Lg.Br.A_d}{\pi n_d}}\right]$	$h_{d,s}=(Ar)_S\times l_{e,s}$ $h_{d,d}=(Ar)_d\times l_{e,d}$	$\frac{\pi}{8LB}\left[n_s l_{e,s}^2+n_d l_{e,d}^2\right]$
Elliptical shallow and triangular deep	$l_{e,s}=2\left[\sqrt{\frac{Lg.Br.A_d}{\pi n_s}}\right]$ $l_{t,d}=\sqrt{\frac{2Lg.Br.A_d}{3n_d}}$	$h_{d,s}=(Ar)_S\times l_{e,s}$ $h_{d,d}=(Ar)_d\times l_{t,d}$	$\frac{1}{8LB}\left[\pi n_s l_{e,s}^2+2\sqrt{3}n_d l_{t,d}^2\right]$
Elliptical deep and triangular shallow	$l_{t,s}=\sqrt{\frac{2Lg.Br.A_d}{3n_s}}$ $l_{e,d}=2\left[\sqrt{\frac{Lg.Br.A_d}{\pi n_d}}\right]$	$h_{d,s}=(Ar)_S\times l_{t,s}$ $h_{d,d}=(Ar)_d\times l_{e,d}$	$\frac{1}{8LB}\left[2\sqrt{3}n_s l_{t,s}^2+\pi n_d l_{e,d}^2\right]$
Triangular shallow and triangular deep	$l_{t,s}=\sqrt{\frac{2Lg.Br.A_d}{3n_s}}$ $l_{t,d}=\sqrt{\frac{2Lg.Br.A_d}{3n_d}}$	$h_{d,s}=(Ar)_S\times l_{t,s}$ $h_{d,d}=(Ar)_d\times l_{t,d}$	$\frac{\sqrt{3}}{4LB}\left[n_s l_{t,s}^2+n_d l_{t,d}^2\right]$

The aspect ratios (A_r) less than or equal to 0.01 and greater than 0.01 are considered as shallow and deep textures respectively (Murthy et al 2007, Qiu et al 2012, Qiu 2013, Uddin et al. 2017). The fluid film thickness is calculated using the equation:

$$h=\begin{cases}C+h_{d,s} & \text{over the shallow texture}\\ C+h_{d,d} & \text{over the deep texture}\\ C & \text{elsewhere}\end{cases} \tag{4.1}$$

Where h is the fluid film thickness and C is the minimum film thickness between the interacting surfaces, $h_{d,s}$ and $h_{d,d}$ texture depth of shallow and deep textures respectively.

4.2. Governing equations

The numerical simulation and equations related to hydrodynamic pressure and asperity pressure used in single-scale textures (Chapter 3) are applicable in the present multi-scale texture analysis. Moreover, the boundary conditions applied along and across fluid flow are same as that of boundary conditions of single scale textured specimen. The effect of deep-shallow texture position, number of textures along and across the fluid flow directions, multi-scale texture configuration is studied and explained in the following section.

4.3. Results and Discussions

Developed numerical code is executed to calculate the tribological characteristics of sliding surfaces by providing appropriate input parameters. The input parameter values considered in this numerical analysis are shown in Table 4.2. The considered tribological characteristics include minimum film thickness, hydrodynamic load percentage, and frictional coefficient. Since the numerical result should not depend on the mesh size, a mesh refinement analysis is carried out. Numerical code is validated with the previously existing result to make the code error-free.

4.3.1. Mesh refinement and code validation

Mesh sensitivity analysis is carried out to determine the appropriate mesh grid so that numerical error is reduced and become negligible. A shallow and deep texture is considered in a unit cell. In the initial iteration, the mesh size of 40 × 40 and 400 × 400 mesh grid is considered for the shallow and deep textures respectively. The mean pressure is calculated by varying the number of nodes across and along the sliding direction of shallow texture as shown in the Fig. 4.1(a). It can be observed that the mean pressure is not varying much after the number of nodes of 90 along the sliding direction and 110 across the sliding direction. Therefore, the mesh grid of 90 × 110 is considered for shallow textures. Once the mesh grid is obtained for shallow texture, a similar procedure is applied to calculate the mesh grid of deep texture which is shown in the Fig. 4.1(b). The final shallow mesh grid $(nx_s \times nz_s)$ of 90 × 110 and deep mesh grid ($nx_d \times nz_d$) of 500 × 600 are used for further analysis.

Table 4.2 Input Parameters used in numerical simulation of multi-scaled textured sliding contacts.

S.No	Input Parameter	Value	Units
1	Velocity of the sliding surface(U)	2, 8	m/s
2	Viscosity of fluid, (μ) (Gu et al., 2016)	0.01	Pa.s
3	Bulk modulus of fluid (α) (Gu et al., 2016)	1.69	GPa
4	Equivalent RMS Roughness of two surfaces (σ) (Gu et al., 2016)	0.63	µm
5	Cavitation pressure (p_c) (Gu et al., 2016)	0.9×10^5	Pa
6	Surface pattern parameter (γ)	1	-
7	Equivalent young's modulus of two surfaces (E') (Gu et al., 2016)	69.1	GPa
8	K'(Gu et al., 2016)	1.198×10^{-4}	-
9	A(Gu et al., 2016)	4.4068×10^{-5}	-
10	Z(Gu et al., 2016)	6.804	-
11	Applied Load (L_N)	10-80	N
12	Atmospheric pressure (p_{atm})	1.01325×10^5	Pa
13	Boundary frictional coefficient (C_f) (Gu et al., 2016)	0.12	-
14	Breadth of the slider (Br)	2	mm
15	Length of the slider (Lg)	4	mm
16	Area of the slider (a)	8	mm^2
17	Area Density (A_d)	0.1, 0.2, 0.3,0.39	-
18	Fluid couple-stress parameter (l)	0,0.5,1,2,3,4,6	µm

After mesh refinement, the developed multi-scaled numerical code is compared with the results of Tomanik et al. (2013) by giving the same input parameters like texture depth, diameter, and pitch. The result of minimum fluid film thickness is shown in the Fig. 4.1(c). The result shows a good agreement with the previously available result and this indicates that the code is error-free. The slight gap between the two results may be due to the type of cavitation condition adopted and mesh grid size.

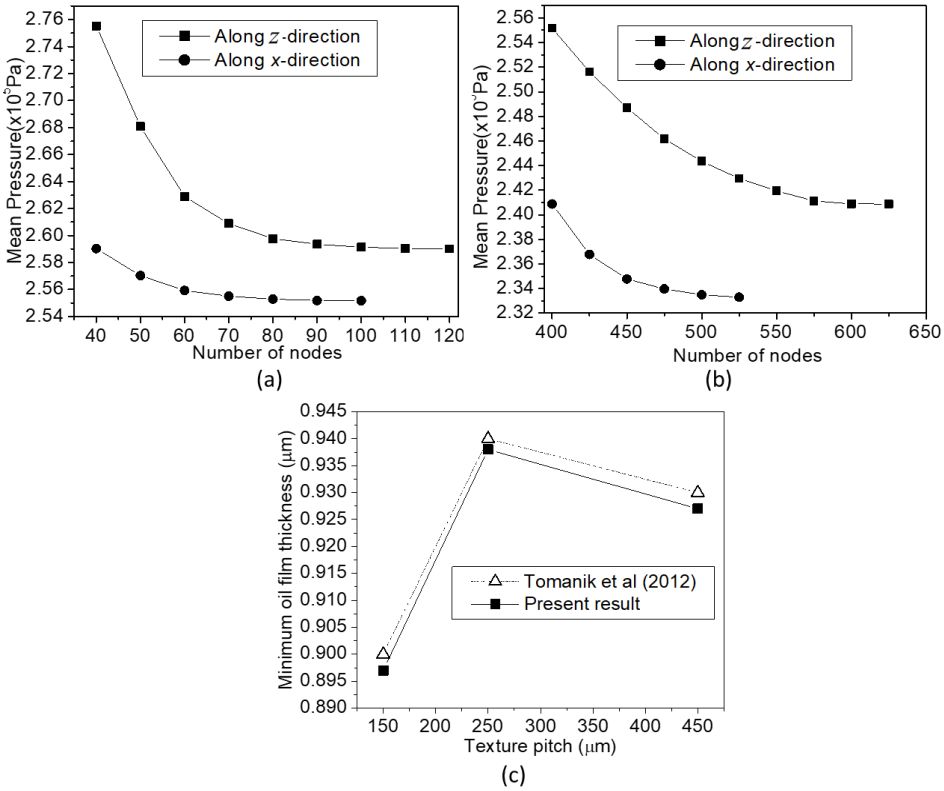

Fig. 4.1. Mesh sensitivity analysis for (a) shallow and (b) deep elliptical texture, and (c) Minimum fluid film thickness vs texture pitch with previously existing result.

The effect of multi-scale textures position, number of textures along and across fluid flow direction, area density, velocity, and load on the tribological characteristics is studied and explained in the below sub-sections.

4.3.2 Effect of multi-scale textures position towards fluid flow direction

In this section, shallow and deep texture location with respect to fluid flow direction is studied. For the present analysis, area density is considered as 0.2, and aspect ratio of shallow and deep textures are considered as 0.004 and 0.011 respectively. The deep textures can be obtained either by changing the texture depth (refer Fig. 4.2(a) and 4.2(b)) or by changing the texture diameter/side length which is shown in the Fig. 4.2(c) and 4.2(d). For the same texture depth, the texture diameter/side length of the deep texture reduces largely as compared to shallow texture diameter/side length to satisfy the condition of the same aspect ratio. However, to maintain the same area density, the number of deep textures has been increased which can be observed in the Fig. 4.2(c) and 4.2(d). The load is varied from 10 to 60 N which corresponds to the applied pressure of 1.25 to 7.5 MPa respectively at a constant velocity of 8 m/s. The total number of deep textures (for same texture depth as of shallow texture) is taken as 8, because

this is the minimum number of textures required to get the aspect ratio of greater than 0.01.

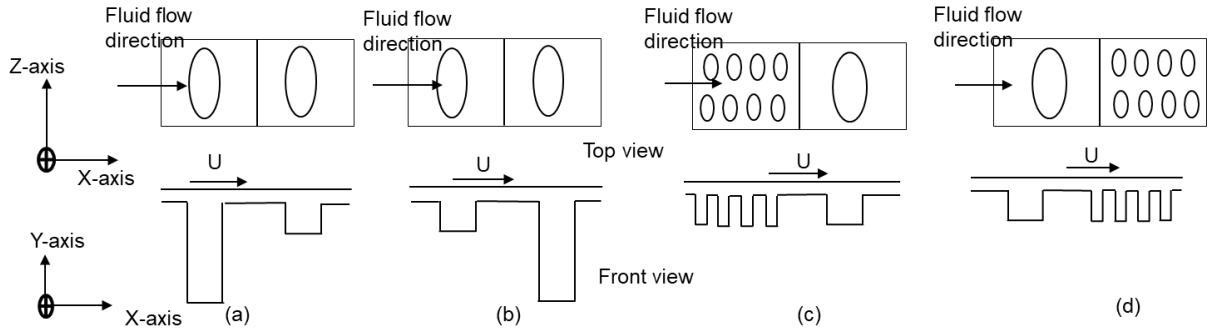

Fig. 4.2. Schematic diagram of different patterns of elliptical textures (a) deep-shallow $(ED\text{-}ES)_d$ (b) shallow-deep $(ES\text{-}ED)_d$ of same diameter (c) deep-shallow $(ED\text{-}ES)_t$ and (d) shallow-deep $(ES\text{-}ED)_t$ of same texture depth.

The effect of these patterns on the tribological characteristics such as minimum film thickness, hydrodynamic load percentage and frictional coefficient with respect to load is shown in the Fig. 4.3. It can be observed that the multi-scale texture position of same depth $(ES\text{-}ED)_t$ exhibit a improved tribological characteristics as compared to other configurations. The location of shallow textures placed first as compared to deep textures to the fluid flow direction depicts an improved tribological characteristics because fluid will not entrap more in shallow textures and enough fluid will flow over the deep textures to produce sustainable pressure development due to which high hydrodynamic load percentage is observed (see Fig. 4.3(b)).

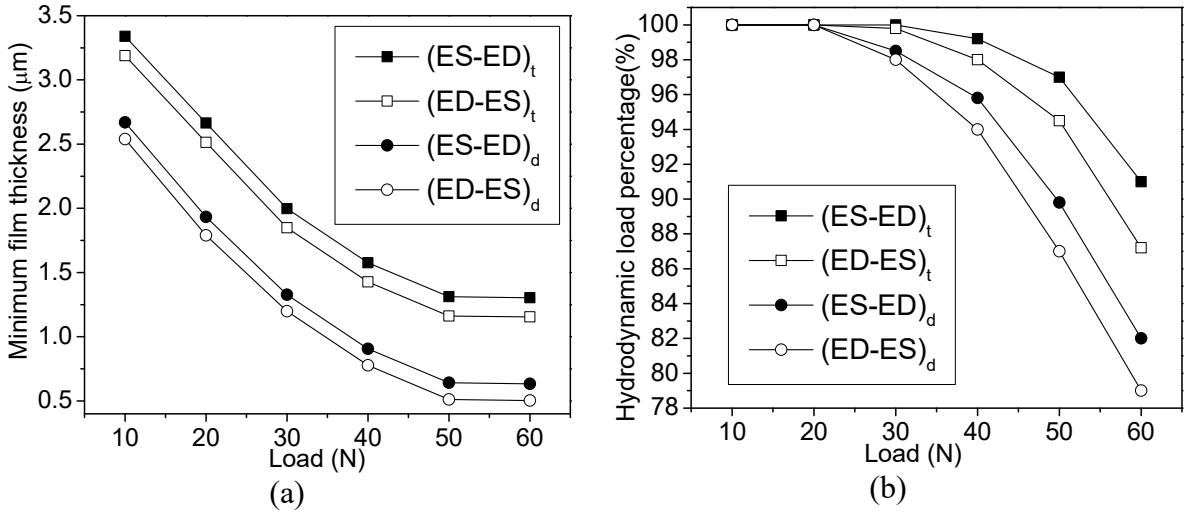

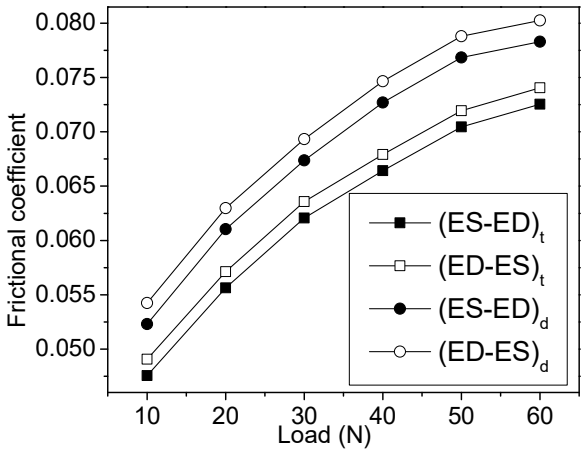

(c)

Fig. 4.3. Effect of load on (a) minimum film thickness, (b) hydrodynamic load percentage and (c) frictional coefficient on different deep-shallow textural positions at a velocity of 8 m/s and area density of 0.2.

It can also be inferred from the Fig. 4.3 that textures of same diameter does not produce better hydrodynamic pressures to support the load. This may be due to the fact that deep textures of same diameter produce higher cavitation thereby lowering hydrodynamic pressures as shown in Fig. 4.4(a) and Fig. 4.4(b), which was also confirmed by Dobrica et al. (2010), Rosenkranz et al. (2016) and Grützmacher et al. (2018). Textures of same depth does not act as reservoirs thereby producing better hydrodynamic pressures as shown in Fig. 4.4(c) and Fig. 4.4(d). In the further analysis of work, multi-scale textures with same texture depth has been considered.

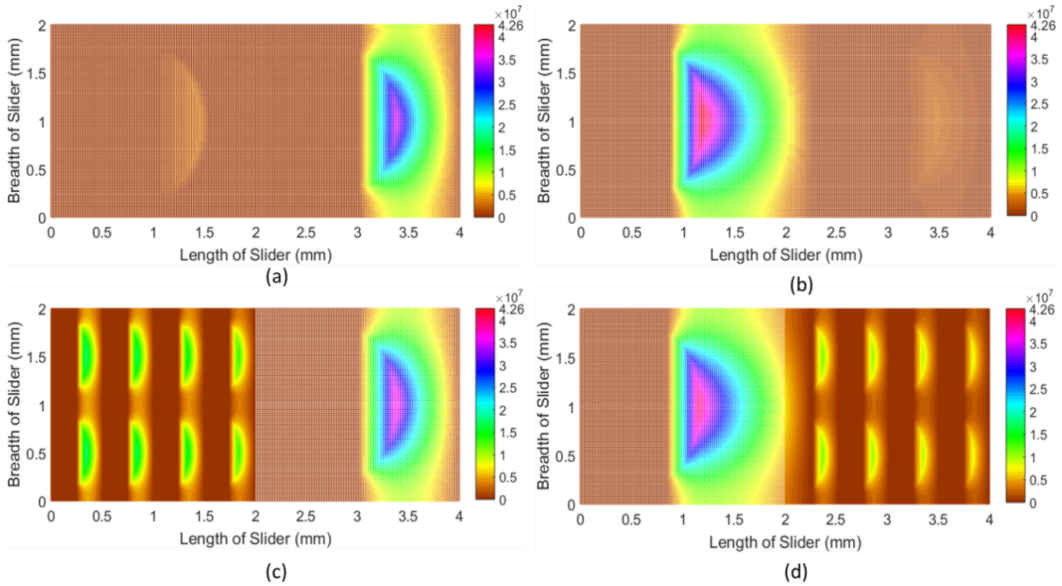

Fig. 4.4. Hydrodynamic pressure profiles (in Pa) of multi-scale textural patterns (a) $(ED\text{-}ES)_d$ (b) $(ES\text{-}ED)_d$ (c) $(ED\text{-}ES)_t$ and (d)$(ES\text{-}ED)_t$ at a constant velocity and load of 8 m/s and 50 N respectively.

4.3.3. Effect of number of textures along and across the fluid flow direction

The effect of number of textures on the tribological characteristics is studied in the present analysis. The schematic diagram of number of deep and shallow textures along the fluid flow direction is shown in the Fig. 4.5. The effect of number of textures along the fluid flow direction is studied by considering a number of deep textures across the fluid flow direction as 2, at an area density of 0.2, velocity of 8 m/s and load of 50 N which corresponds to 6.25 MPa. The aspect ratio of shallow texture is 0.004 and deep textures are in between 0.011 to 0.014 for deep texture number of 8 to 14. The effect of number of textures across the fluid flow direction on the tribological characteristics is shown in the Fig. 4.6. It can be inferred from Fig. 4.6(a) that there is a decrease in minimum film thickness and an increase in frictional coefficient as the texture number increases from $n_{d,x}$=4 to $n_{d,x}$=7.

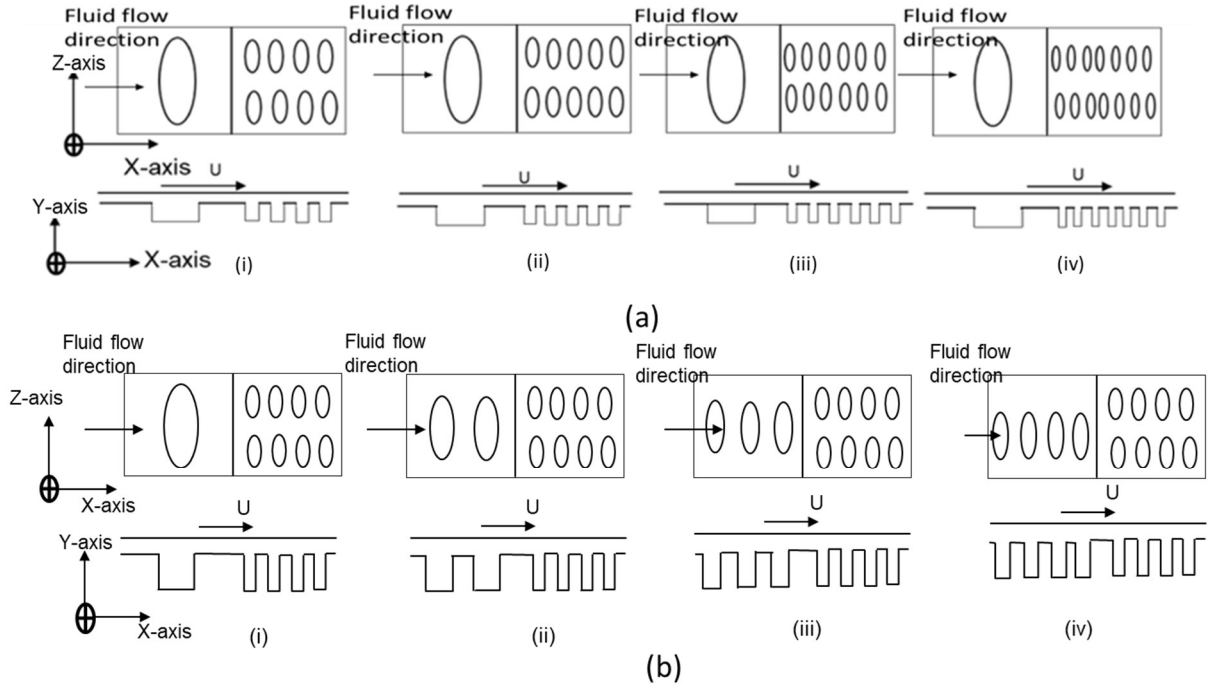

Fig. 4.5. Schematic diagram of (a) number of deep elliptical texture along fluid flow direction (i) $n_{d,x}$=4, (ii) $n_{d,x}$=5, (iii) $n_{d,x}$=6, and (iv) $n_{d,x}$=7, (b) number of shallow elliptical texture along sliding direction (i) $n_{s,x}$=1, (ii) $n_{s,x}$=2, (iii) $n_{s,x}$=3,and (iv) $n_{s,x}$ =4.

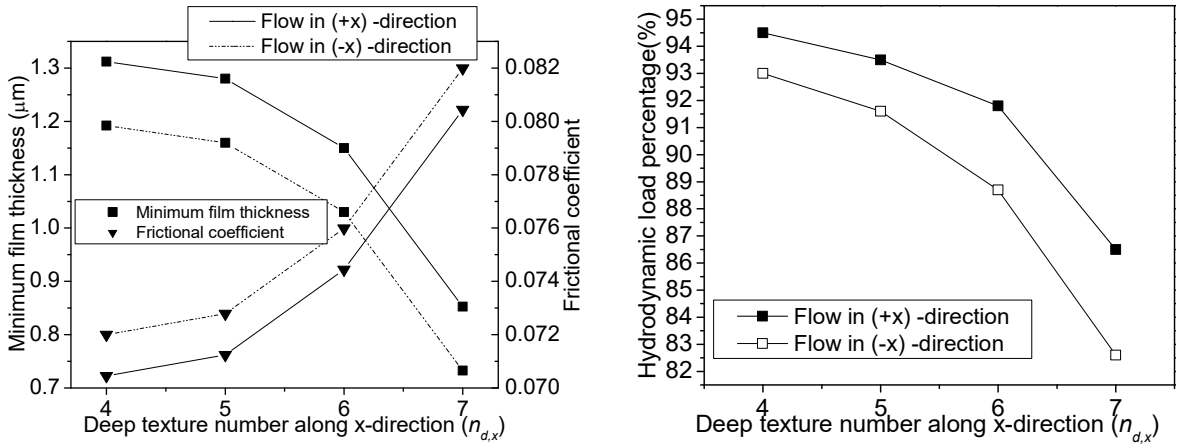

(a) (b)

Fig. 4.6. Effect of deep texture number along fluid flow (in *x*-direction) on tribological characteristics at L_N=50 N, U=8 m/s and $n_{s,x}$=1, $n_{s,z}$=1 & $n_{d,z}$=2.

The fluid flows towards the initial textures higher hydrodynamic pressures are generated. When fluid further flows towards the successive textures, fluid loses potency to generate higher hydrodynamic pressures thereby getting exhausted. This leads to reduction in hydrodynamic load percentage (see Fig. 4.6(b)). The reduction of hydrodynamic pressures may be due to fluid entrapment where hydrodynamic pressure contours decreases as fluid flows through successive deep textures (refer Fig. 4.7). Therefore, for further analysis, the number of deep textures along the fluid flow direction is considered as 4.

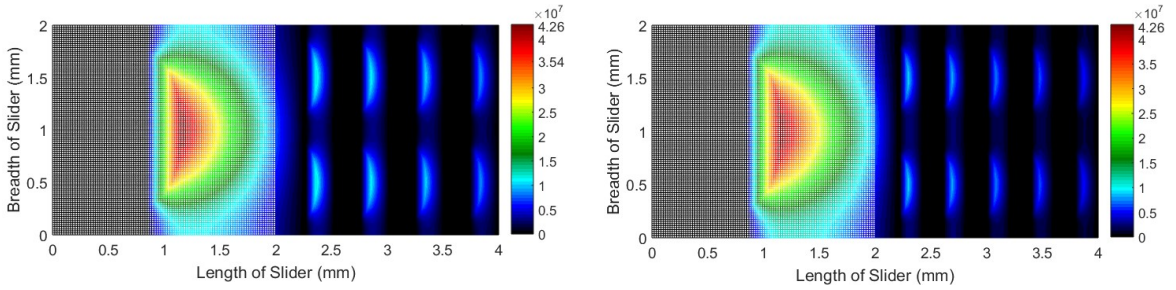

(a) (b)

Fig. 4.7. Hydrodynamic pressure profiles (in Pa) of deep texture number (a) $n_{d,x}$=4 and (b) $n_{d,x}$=5 at a constant velocity and load of 8 m/s and 50 N respectively and $n_{s,x}$=1, $n_{s,z}$=1 & $n_{d,z}$=2.

Similarly, an analysis is carried out by increasing the number of shallow textures. With the increase in shallow texture number ($n_{s,x}$), minimum film thickness decreases and frictional coefficient increases as shown in Fig. 4.8 (a). This is because the fluid film does not able to generate a sustainable fluid film pressure and reduction in hydrodynamic load percentage which is shown in Fig .4.8(b). This can be also be confirmed by observing the hydrodynamic pressure

profiles which is shown in Fig .4.9. It can be seen that $n_{s,x}$=1 (refer Fig .4.9(a)) produces higher and broader hydrodynamic pressures contour as compared to $n_{s,x}$=2 (refer Fig .4.9(b)).

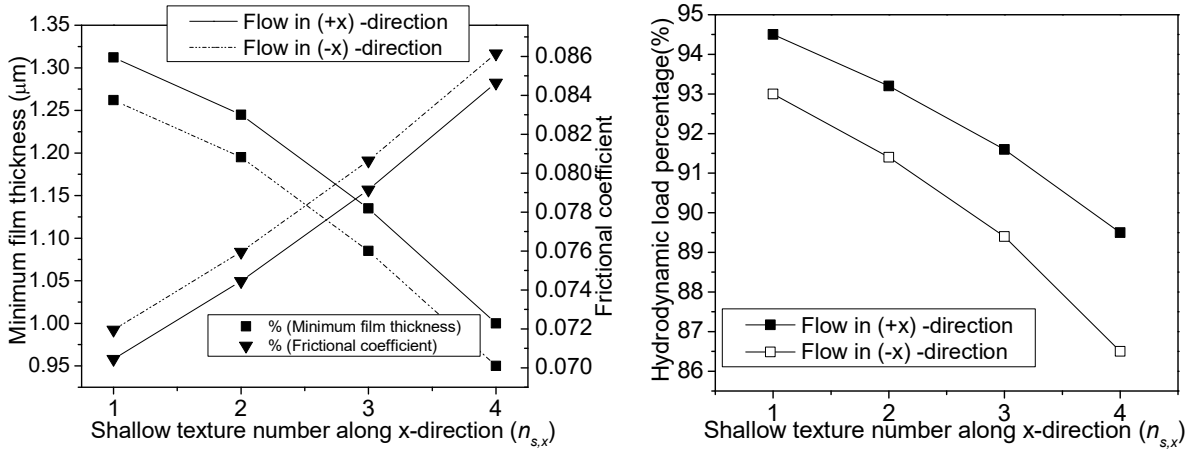

(a) (b)

Fig. 4.8. Effect of shallow texture number along fluid flow (in *x*-direction) on tribological characteristics at L_N=50 N, U=8 m/s and $n_{s,z}$=1, $n_{d,x}$=4 & $n_{d,z}$=2.

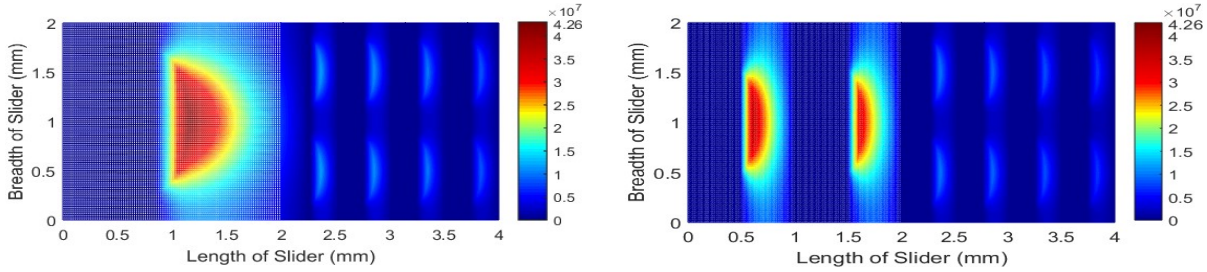

(a) (b)

Fig. 4.9. Hydrodynamic pressure profiles (in Pa) of shallow texture number (a) $n_{s,x}$=1 and (b) $n_{s,x}$=2 at a constant velocity and load of 8 m/s and 50 N respectively at $n_{s,z}$=1, $n_{d,x}$=4 & $n_{d,z}$=2.

From the previous analysis, shallow and deep texture numbers along fluid flow direction of 1 and 4 respectively shown improved tribological characteristics. Hence, the analysis is performed by varying the number of textures across the fluid flow direction considering number of textures along the fluid flow direction as $n_{s,x}$=1and $n_{d,x}$=4 at an area density, velocity, and load of 0.2, 8 m/s, and 50 N respectively. Figure 4.10 indicates the schematic diagram of number of textures across the fluid flow direction. The aspect ratio of single shallow texture is 0.004 and deep textures are in between 0.011 to 0.02 for a number of deep textures 8 to 28 respectively.

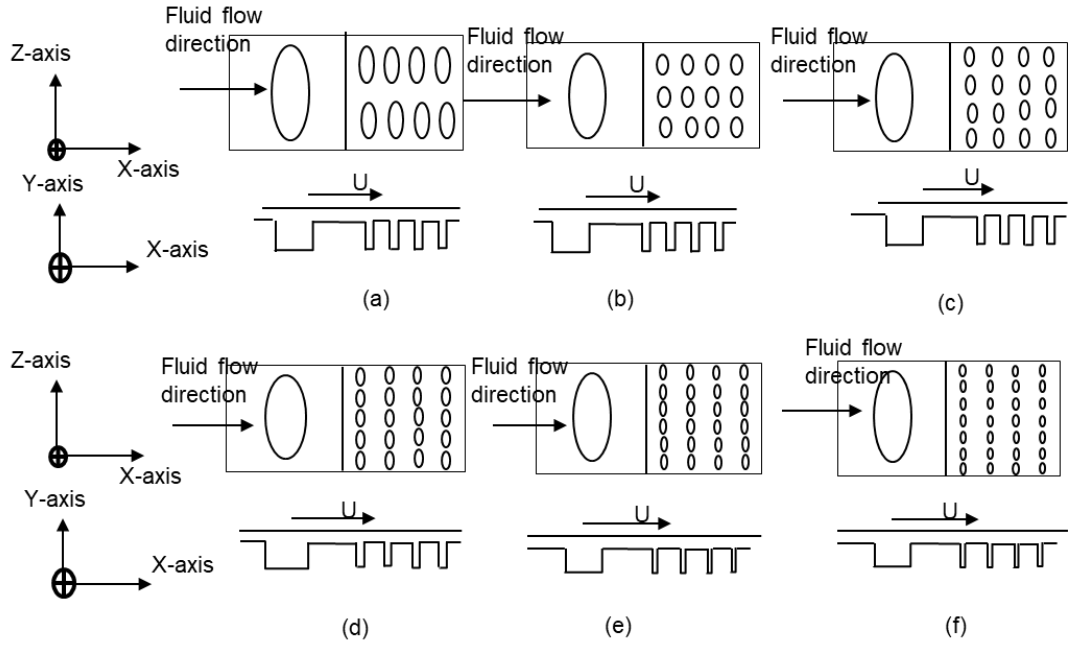

Fig. 4.10. (a) Schematic diagram of elliptical deep texture number (a) $n_{d,z}$=2, (b) $n_{d,z}$=3, (c) $n_{d,z}$=4, (d) $n_{d,z}$=5 (e) $n_{d,z}$ =6 and (f) $n_{d,z}$=7 across fluid flow direction.

The effect of number of textures across the fluid flow direction on the tribological characteristics is shown in the Fig. 4.11. It can be observed that there is an increase in film thickness (refer Fig. 4.11(a)), hydrodynamic load percentage (refer Fig. 4.11(b)) and decrease in frictional coefficient (refer Fig. 4.11(a)) with the number of textures of up to $n_{d,z}$=5. Because as the number of textures increases across the fluid flow direction, fluid counteracts the multiple textures produces better pressure contours between adjacent textures thereby improving tribological characteristics which can be seen in Fig. 4.12(a). Further increase in texture number, decreases the minimum film thickness, hydrodynamic load percentage and increases the frictional coefficient. As the number of textures increases, the size of texture reduces due to which fluid flow may not experience any textural effect. This causes a reduction in the hydrodynamic pressure as shown in Fig. 4.12(b). For further analysis of the present work, the shallow texture is considered as one and deep textures along and across the fluid flow direction are considered as 4 × 5. The effect of fluid flow in reverse direction is also shown in Fig. 4.6 and Fig 4.8. During bi-directional condition, there is interchange of shallow and deep textures to the fluid flow. It is already shown in Fig. 4.3 that there is slight increment in frictional coefficient when fluid flows from deep to shallow textures as compared to fluid flow from shallow to deep textures. The same effect of increased frictional coefficient for bi-directional sliding is seen in this section (refer Fig. 4.6 and Fig. 4.8.) irrespective of varying texture number.

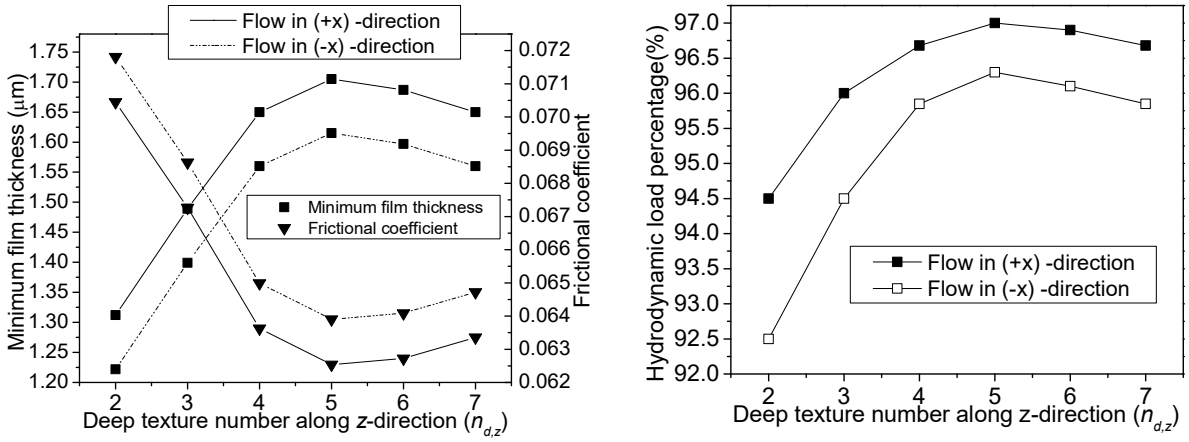

(a) (b)

Fig. 4.11. Effect of deep texture number across fluid flow (in *z*-direction) on tribological characteristics at a constant velocity and load of 8 m/s and 50 N respectively.

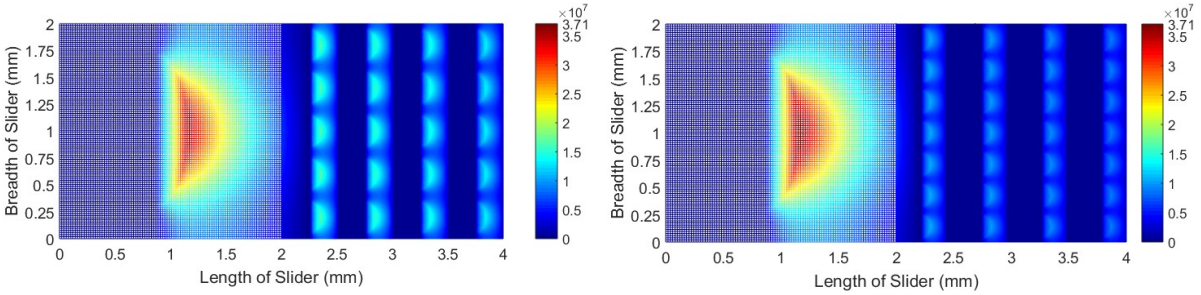

(a) (b)

4.12. Hydrodynamic pressure profiles (in Pa) of deep texture number (a) $n_{d,z}$=5 and (b) $n_{d,z}$=7 at a constant velocity and load of 8 m/s and 50 N respectively.

4.3.4 Effect of texture shape and area density

The present analysis is performed with the texture number ($n_{s,x} \times n_{s,z}$) of 1×1 and ($n_{d,x} \times n_{d,z}$) of 4×5 which produces improved tribological characteristics by considering two textural shapes, namely, elliptical and triangular. The different multi-scale textural configurations of elliptical shallow–elliptical deep (ES-ED) elliptical shallow–triangular deep (ES-TD), triangular shallow–elliptical deep (TS-ED), and triangular shallow–triangular deep (TS-TD) are shown in the Fig. 4.13, and their effect on the tribological characteristics with varying area density is shown in the Fig. 4.14. The velocity and load are considered as 8 m/s and 50 N by varying area density from 0.1 to maximum possible area density of 0.39. The aspect ratio of single shallow texture is in between 0.0057 to 0.0032 and deep textures are in between 0.026 to 0.014 for area densities of 0.1 to 0.39 respectively.

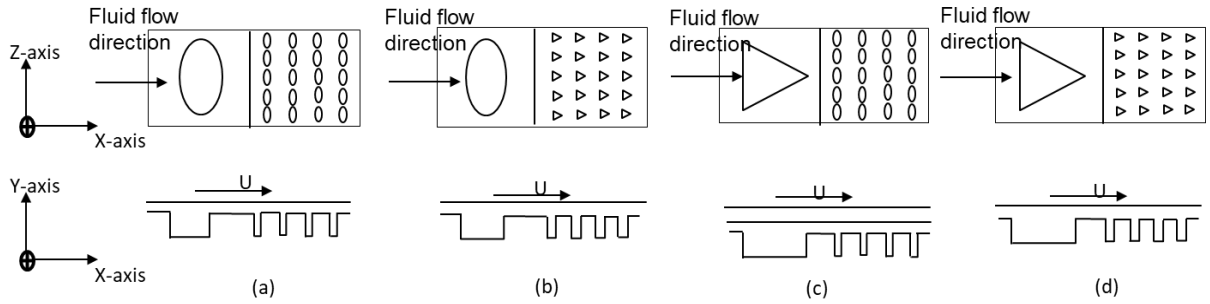

Fig. 4.13. Schematic diagram of (a) elliptical shallow and elliptical deep (ES-ED), (b) elliptical shallow and triangular deep (ES-TD), (c) triangular shallow and triangular deep (TS-TD), and (d) triangular deep and elliptical shallow (TS-ED) textural configurations.

The effect of area density on the tribological characteristic is shown in Fig. 4.14. From Fig. 4.14 it can be observed that minimum film thickness, hydrodynamic load percentage increases and frictional coefficient decreases with the area density of up to 0.3. Further increase in area density exhibit a negative effect on the tribological characteristic parameters. This may be due to the collapse of film thickness because of lessened gap between texture-to-texture boundaries at the maximum possible area density.

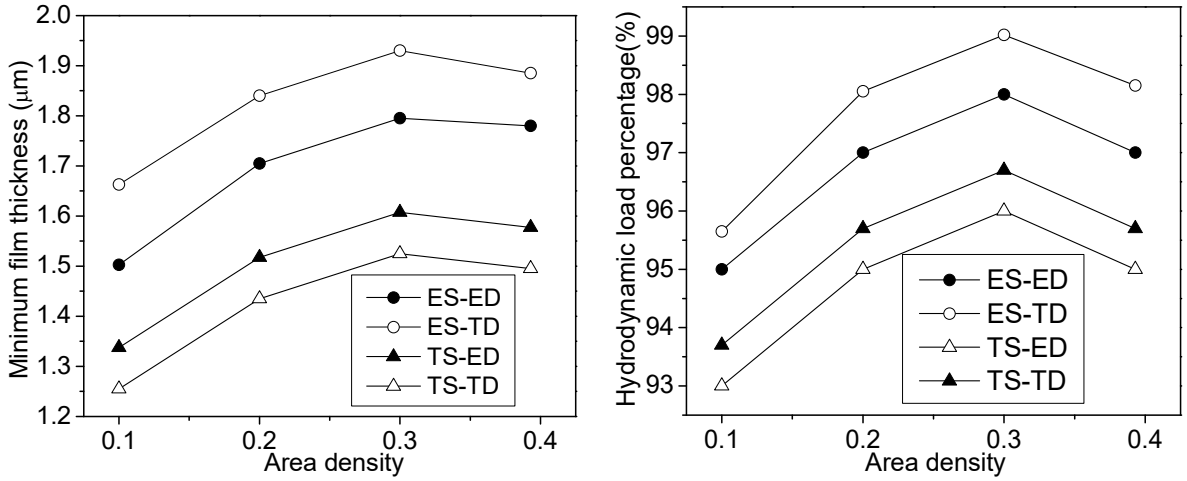

(a) (b)

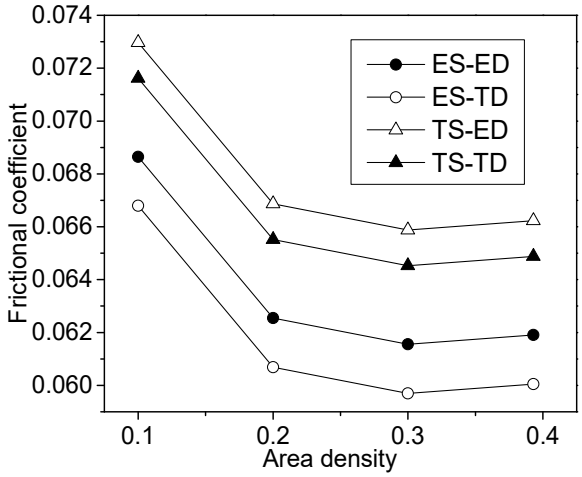

(c)

Fig. 4.14. Effect of area density on (a) minimum film thickness (b) hydrodynamic load percentage and (c) frictional coefficient.

ES-TD configuration generates improved tribological characteristics as compared to other configurations which can be observed in Fig. 4.14. This can be attributed to the better generation of hydrodynamic pressure contours by triangular deep textures as compared to elliptical deep textures (refer Fig. 4.15). Triangular deep textures develop a sustainable hydrodynamic lubrication regime and restrict the surfaces entering into mixed lubrication as shown in Fig. 4.15(b) (i) and 15(d) (i). This may be due to the fluid convergence towards the apex, the pressure contour inside the deep textures develops higher peak pressures. In contrast, an elliptical shallow texture produces better hydrodynamic pressures as compared to triangular shallow textures as shown in Fig. 4.15(a)(i) and 15(b)(i). This can be attributed to fluid encountering the higher wedge for elliptical shallow texture, thereby producing better hydrodynamic pressure contours. Therefore, the combination of ES-TD configuration exhibits improved tribological characteristics as compared to other configuration. The area density of zero implies the flat texture at which lower minimum film thickness and higher frictional coefficient of 0.801 μm and 0.115 respectively are observed. During reverse flow due to bi-directional sliding, both elliptical and triangular textures interchange each other. In addition to the interchange of textures, triangular texture orientation also changes. This leads to the drastic reduction in tribological performance. Therefore, the effect of reverse flow is not shown in this section.

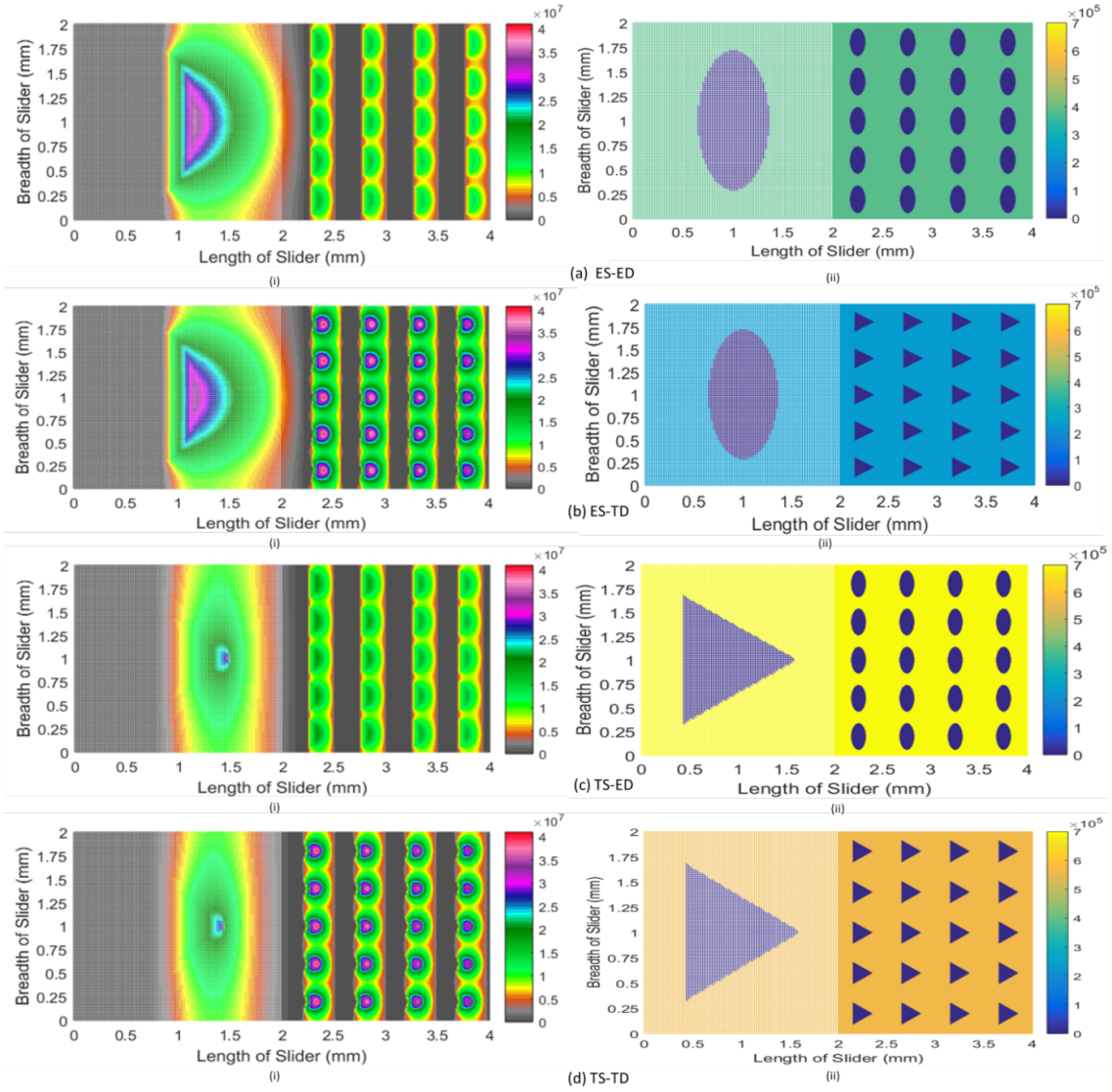

Fig. 4.15. Hydrodynamic and asperity pressure profiles (in Pa) of multi-scaled textures of (a) ES-ED, (b) ES-TD, (c) TS-ED and (d) TS-TD different configurations at a constant velocity and load of 8 m/s and 50 N respectively.

In the previous analysis, single scale textural surfaces are studied and their tribological performance is investigated. In the present analysis, the impact of multi-scale textures on tribological performance is examined. Therefore, under similar operating conditions the performance of multi-scale and single textures are compared in the following section.

4.3.5 Comparison of multi-scaled with single-scaled textures

As observed from the previous study, ES-TD configuration exhibits improved tribological characteristics. Hence, in the present analysis, ES-TD configuration of area density (A_d) of 0.3 is considered. The two velocities, i.e., 2 m/s and 8 m/s, and load of 10-80 N which corresponds

to 1.25-10 MPa respectively have been considered for the analysis. The effect of multi-scaled and single-scaled textures on the tribological characteristics with varying load is shown in the Fig. 4.16. The aspect ratios of multi-scaled textures used are 0.0033 and 0.014 respectively at an area density of 0.3. Also, the aspect ratio of single-scaled textures used is 0.01 at same area density of 0.3.

The effect of load on the tribological characteristics is shown in Fig. 4.16. The reduced frictional coefficient is observed with the use of multi-scale textures as compared to single-scale textures which implies that the multi-scaled texturing is effective. With the increase in load and/or decrease in sliding speed, frictional coefficient increases as shown in Fig. 4.16(c). From the results of Hsu et al., (2015), it has been observed that the effect of load and velocity on tribological performance of single and multi-scaled textures exhibit a similar trend.

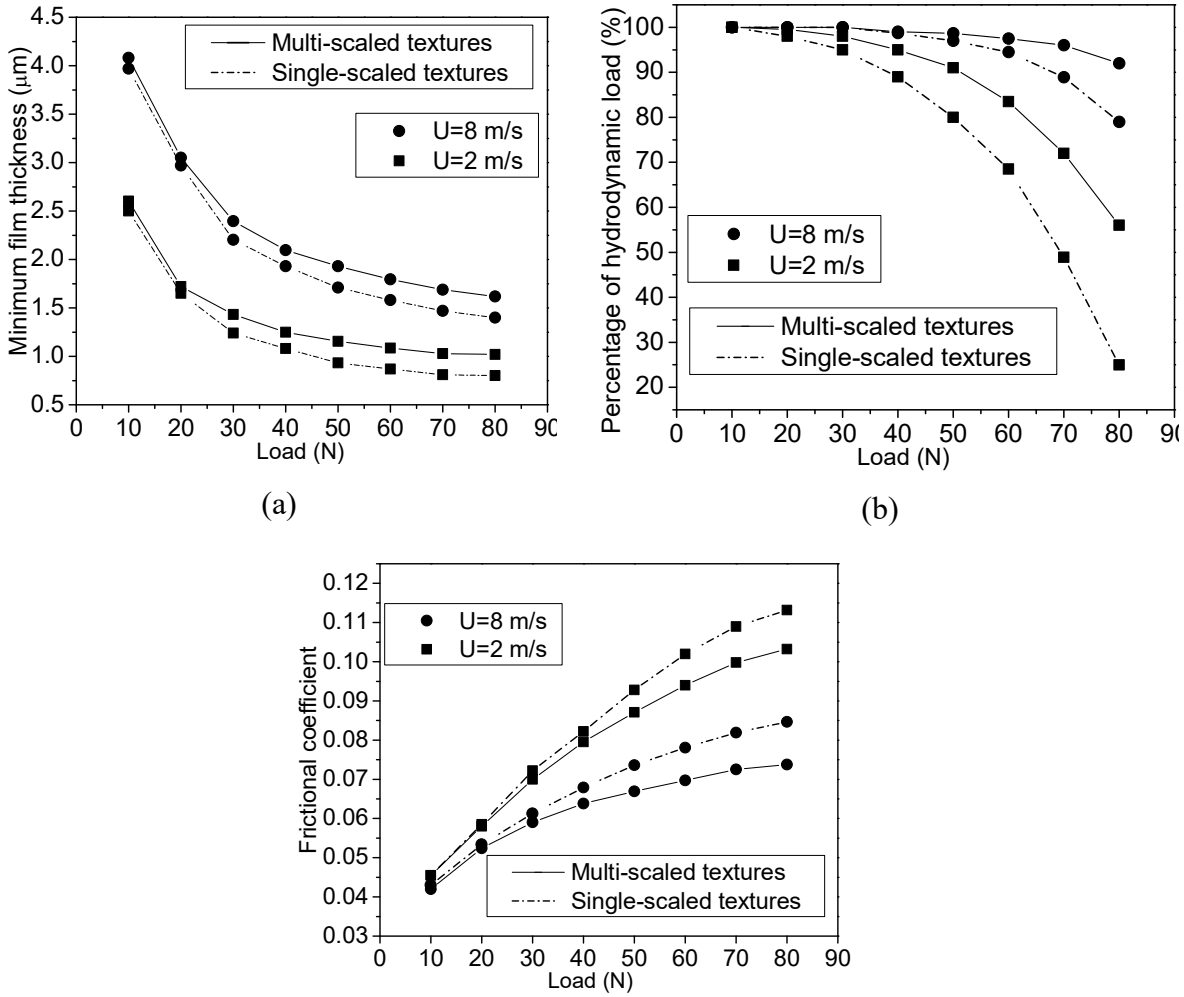

Fig. 4.16. Effect of load on (a) minimum film thickness (b) hydrodynamic load percentage and (c) frictional coefficient for single-scale and multi-scale textures.

At lower load of 10 N, no/negligible change in tribological performance is observed (refer Fig 4.16) for single and multi-scaled textures. This can be due to the hydrodynamic regime prevails in both single and multi-scale textures which can be inferred from Fig 4.16 (b). However, at higher load of 80 N, enhanced minimum film thickness and reduced frictional coefficient have been observed for multi-scaled textures as compared to single-scaled textures as shown in Fig. 4.16(a) and 16(c) respectively. This can be attributed to the better hydrodynamic load percentage developed by multi-scaled textures as compared to the single-scaled textures which is shown in Fig. 4.16(b). This can also be confirmed by pressure contours (refer Fig 4.17(a)) i.e. higher hydrodynamic pressure generated by multi-scaled textures as compared to single-scaled textures. Hence, lower asperity pressures are produced by multi-scale textures as compared to single-scale textures (refer Fig. 4.17(b)) to support the total applied load. The lower hydrodynamic pressure contours generated by single-scaled texture urges the more asperity contacts to balance the applied load thereby producing higher asperity pressures (single-scale peak pressure is 3.5 MPa whereas for multi-scale, it is of 1.5 MPa) as shown in Fig. 4.17(b).

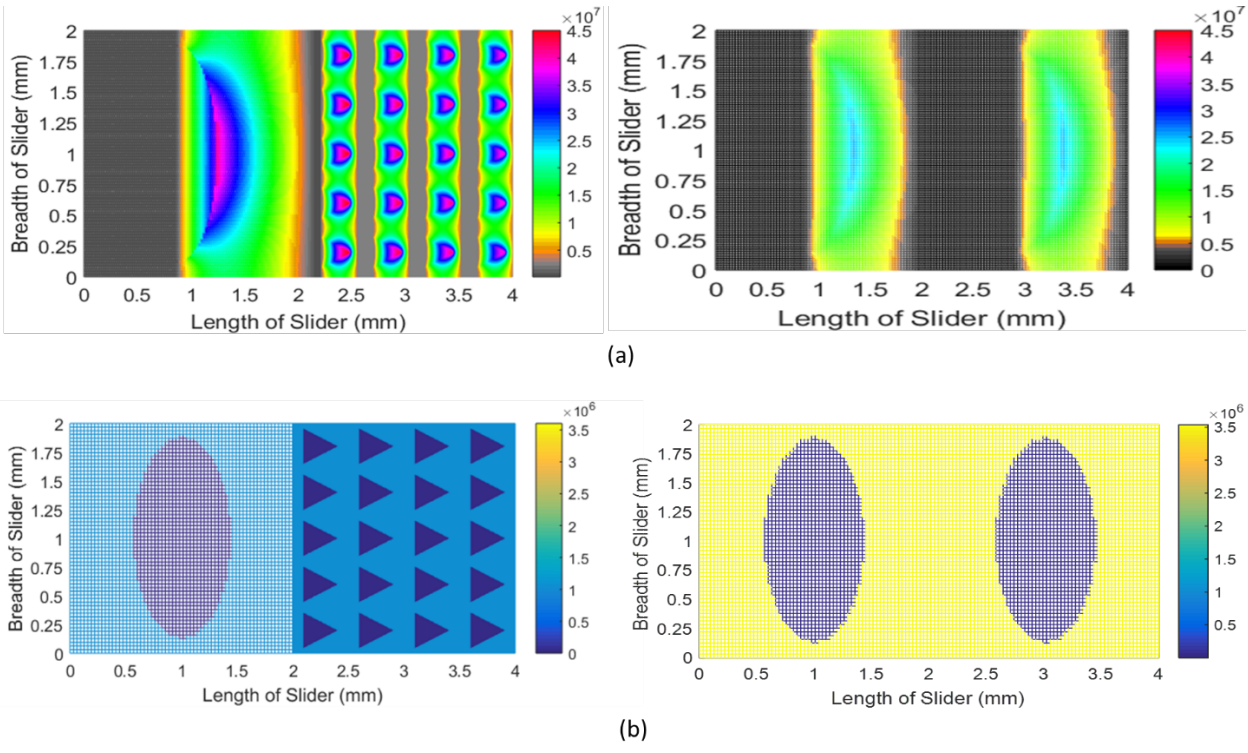

Fig. 4.17 (a) Hydrodynamic and (b) asperity pressure profiles (in Pa) for multi-scaled and single-scaled textures at Load of 80 N and velocity of 8 m/s.

4.3.6 Effect of couple-stress fluid parameter on minimum film thickness and coefficient of friction

In this section, the effect of couple-stress fluid parameter on variation of minimum film thickness, frictional coefficient for the above mentioned single-scaled and multi-scaled textural configuration is studied. It can be observed from Fig. 4.18 that minimum film thickness between the interacting surface increases and frictional coefficient decreases with couple-stress fluid parameter for both single-scaled and multi-scaled textural configurations. Moreover, better tribological performance is observed for multi-scale textures as compared to single scale textures. This may be due to better hydrodynamic pressure obtained for multi-scale texture as shown in Fig. 4.19.

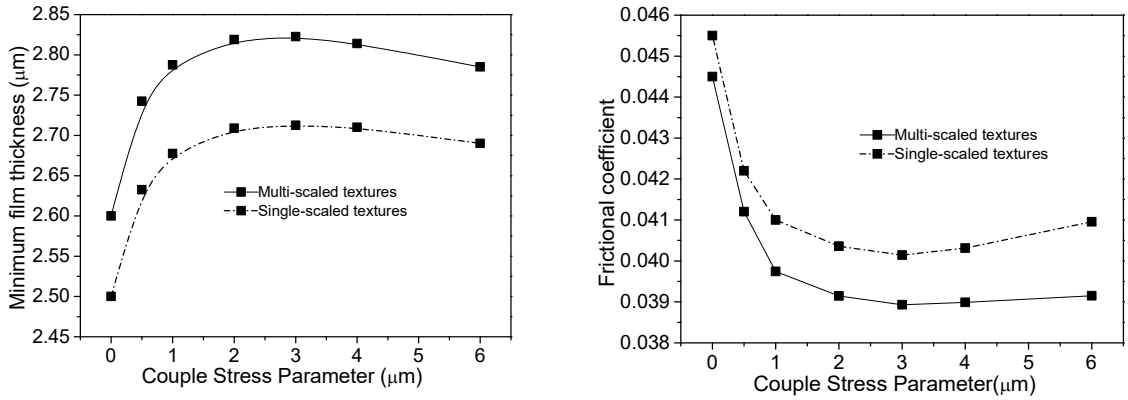

(a) (b)

Fig. 4.18. Comparison of (a) minimum film thickness and (b) frictional coefficient with couple-stress parameter ,*l* for single-scale and multi-scale textures at velocity of 2 m/s, and load of 10 N.

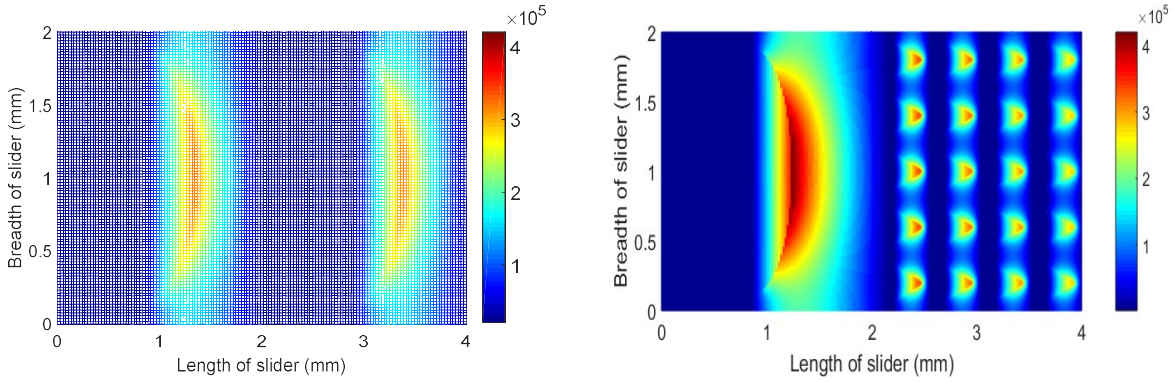

(a) (b)

Fig. 4.19 (a) Hydrodynamic pressure profiles (in Pa) for (a) Single-scaled and (b) multi-scaled textures at couple-stress parameter of 3 μm.

4.4 Summary

This paper has discussed the multi-scale textural position, multi-scale texture shape, multi-scale texture area density along with couple-stress parameter influence on the tribological characteristics of multi-scale textured parallel sliding surfaces under JFO cavitation and mixed lubrication condition. The effect of load and velocity on multi-scale textures is also studied. By the use of multi-scale textures better minimum film thickness, reduced frictional coefficient and higher hydrodynamic load percentage was observed. By observing the above section, it is concluded that multi-scaled textures of shallow-deep pattern with constant texture depth produce improved tribological characteristics. A single shallow texture and number of deep textures of 4 × 5 along and across the fluid flow direction exhibit improved tribological characteristics. Multi-scaled textures of ES-TD configuration contribute improved tribological characteristics than other configurations like ES-ED, TS-ED, and TS-TD. Couple-stress fluid parameter shows positive effect on both minimum film thickness and coefficient of friction of multi-scale textures. On a whole, multi-scaled textures can be used in the applications where both fluid film and asperity contact co-exists. For the applications where both asperity as well as fluid film pressure exists, the single-scale textures produce higher friction. In this circumstance, the concept of multi-scale textures exhibits a higher tribological performance in comparison with single scale textures.

Experimental work gives clear idea on the effect of multi-scale textured sliding contacts on the tribological performance. Therefore, experimental tests were conducted on multi-scale textures to determine the tribological performance. Multi-scaled textures are fabricated on low carbon steel of AISI 1020 through Nd: YAG laser and tested using on pin-on-disc friction and wear test rig. Chapter 5 describes the detailed explanation on the fabrication of multi-scale textures.

Chapter 5

Fabrication of multi-scaled surface textures using a nano-second Nd: YAG laser

Experimental work gives clear idea on the effect of multi-scale textured sliding contacts on the tribological performance. Therefore, experiments were performed on the development of multi-scale textures through laser surface texturing. A laser texturing method has been chosen to fabricate textures due to its effectiveness and accuracy in producing textures of required size and depth. Laser fabrication of textures depends on wavelength, pulse number and frequency. Therefore, in this chapter, experimental tests were conducted on a surface to analyze the effect of wavelength, pulse number and frequency on the produced texture size and depth. Moreover, multi-scale textures were fabricated using appropriate laser parameters.

5.1 Materials

Based on the literature survey, low carbon steel of AISI 1020 type is selected as specimen material. Specimen properties are shown in Table 5.1.

Table 5.1 Specimen material properties.

Material	AISI 1020
Modulus of Elasticity	200 GPa
Yield strength	295 MPa
Poisson's ratio	0.29
Hardness	126 VC
Average surface Roughness (R_a)	0.21±0.09 μm
Density (d)	7.87 g/cc

The specimen surface is fine polished using 1000 and 2000 grit emery papers to minimize roughness. They are further wet polished with alumina-water solution to make specimen free from scratches, and then with 1 µm diamond particle paste to obtain a mirror-like appearance. After polishing, the average surface roughness, R_a of untextured specimens is 0.21±0.09 µm. The surface roughness of pin specimens is measured using a surface roughness tester (Taylor Hobson, Surtronic S-128) as depicted in Fig. 5.1. The measurements are done with a measuring tip having a rounding radius of 2 µm.

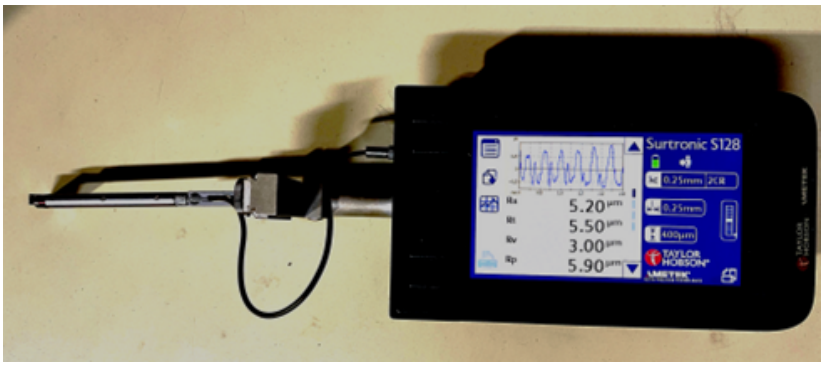

Fig. 5.1 Surface Roughness Tester Surtronic S-100 (Taylor Hobson).

5.2 Method of texture fabrication

The laser texturing is done on AISI 1020 steel using Nd-YAG laser of Beam-tech, Nimma-400 series model. The laser equipment and its working can be seen in Fig. 5.2. The laser emitting from the shutter of laser head is passed through right-angled triangular prism to propagate the laser beam in perpendicular direction due to internal reflection. The optical mechanism of internal reflection is shown in Fig 5.3.

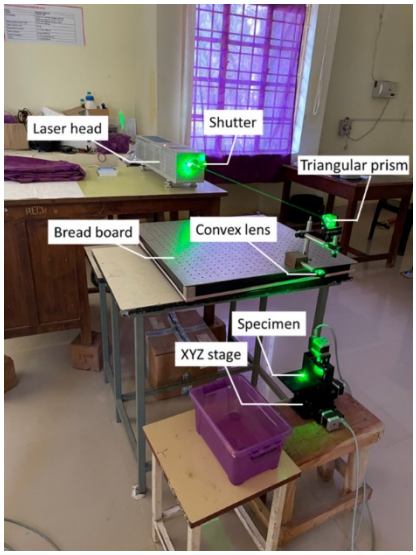

Fig. 5.2. Laser equipment and working of laser.

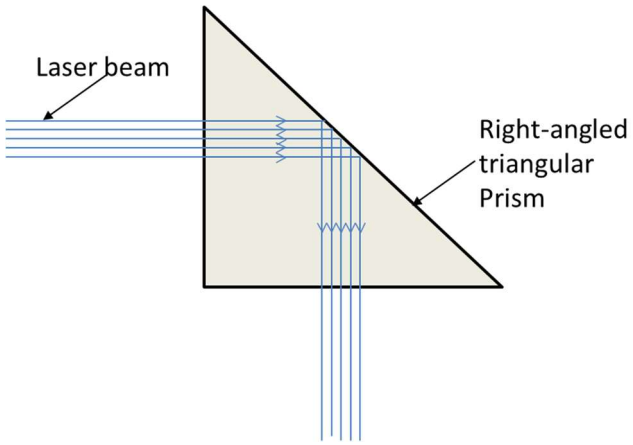

Fig. 5.3. Laser beam propagation due to internal reflection in prism.

The beam is then passed through convex lens and its specifications are shown in Table 5.2. By the use of convex lens, the parallel laser beam is converted to converging beam as shown in Fig. 5.4. The required texture size/beam size *(R)* can be obtained by adjusting the distance between convex lens and specimen. The movement of specimen is controlled by using motorized XYZ stage. The formula to find the specimen-lens distance *(D)* to get the required laser beam size can be given in below equation (refer Appendix-A for the derivation):

$$D = F\left[1 - \frac{R}{B}\right] \tag{6.1}$$

Here, *F*=Focal length of the lens and *B*=Actual laser beam size.

Table 5.2. Lens specifications.

Material	BK7 or equivalent (Borosilicate Crown glass)
Lens shape	Spherical
Diameter	25 mm
Clear Aperture	> 90% of Diameter
Coating	Coated (Single layer MgF2)

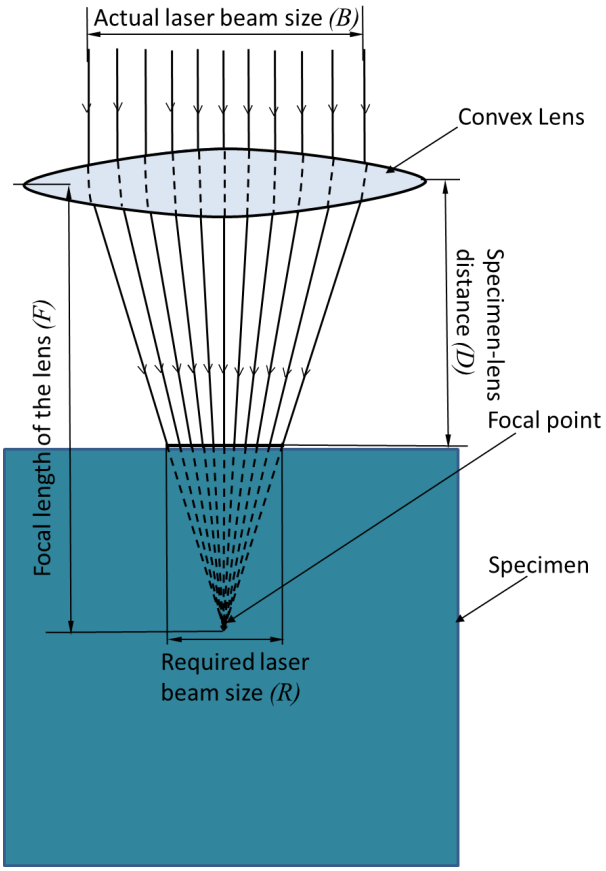

Fig. 5.4. Schematic representation of beam convergence through convex lens.

The fabricated textures are wet polished with alumina-water solution to remove the deposited material along the edge of the textures and then polished with 1 µm diamond particle paste to obtain a mirror-like appearance. The specimen is then cleaned using the ultra-sonic cleaner at 60 Hz frequency for 15 min in room temperature to remove the loose particles present within the texture cavity. The ultra-sonic cleaner used for specimen cleaning is shown in Fig 5.5. After polishing and cleaning, the average roughness (R_a) of the specimen ranges between 0.3±0.07 µm.

Fig. 5.5 Ultra-sonic cleaner (Aczet, CUB 2.5 model).

The size of the texture is visualized using a high-resolution scanning electron microscopy (SEM) of Hitachi-4800 model (Tokyo, Japan) (refer Fig. 5.6) and the obtained SEM image of 1000 µm diameter dimpled surface along with smooth surface is shown in Fig. 5.7(a) and 5.7(b) respectively.

Fig. 5.6. Scanning electron microscope.

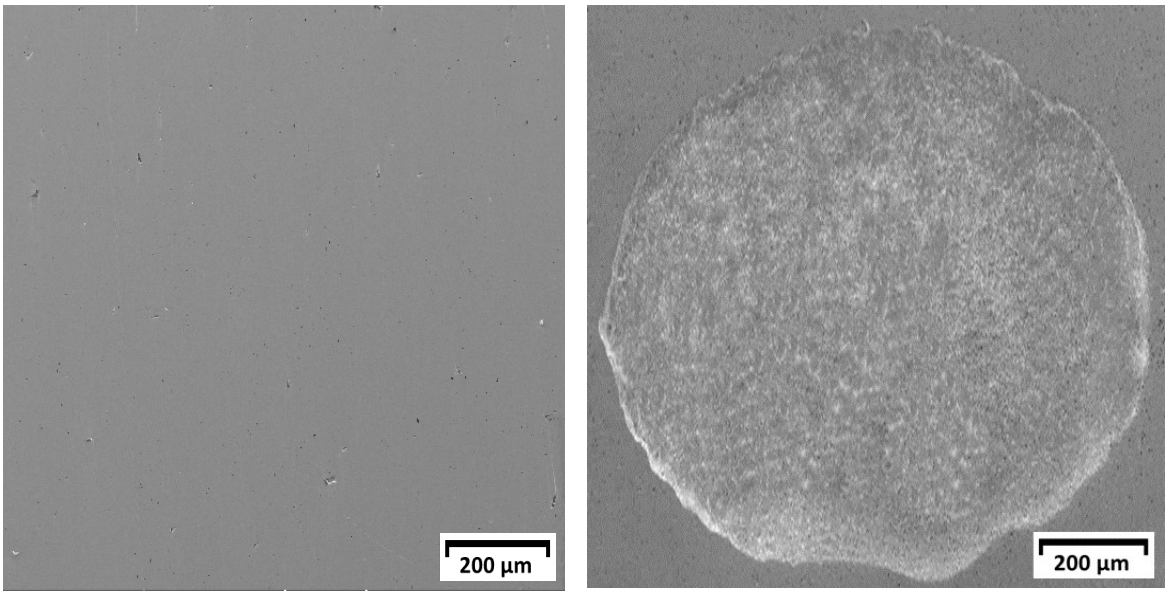

(a) (b)

Fig. 5.7. A SEM image of (a) smooth surface and (b) 1000 µm dimple diameter with dimple cross sectional area.

5.3 Results and discussion

In the previous sub-section, an approach to fabrication of textures through a pulsed Nd: YAG laser is discussed. In this sub-section the effect of laser parameters like pulse number and frequency on texture depth is studied at different wavelengths.

5.3.1 Effect of pulse number on texture depth

In the present analysis, the effect of texture depth vs pulse number for a dimple diameter of 1000 µm at a constant laser fluence of 2.18 J/cm^2 and frequency of 5 Hz is shown in Fig. 5.8. It can be seen in Fig. 5.8 that to produce texture depths till 50 µm, relatively a lower pulse number is required. This may be due to better splattering of the molten pool present inside texture depth around the texture edges due to lower texture depths. To produce texture depths of above 50 µm, relatively higher pulse number is required. This can be due to the molten pool present in larger texture depth does not carry easily above the texture edge. It can also be seen from the Fig. 5.8 that higher texture depths are produced at lower wavelength of 532 nm. This can be attributed to the better absorption of laser energy at 532 nm wavelength by the target material as compared to 1064 nm wavelength.

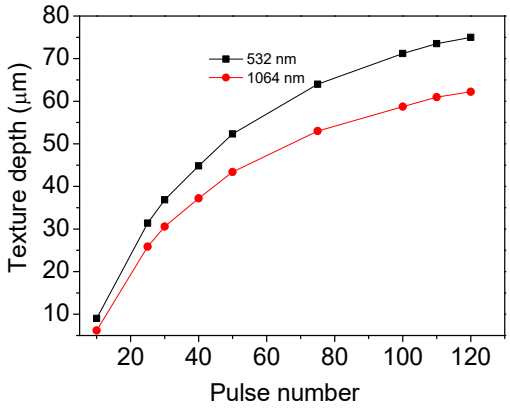

Fig. 5.8. The texture depth vs pulse number for the size of 1000 μm at constant laser fluence of 2.18 J/cm^2 and frequency of 5 Hz.

5.3.2 Effect of frequency on texture depth

The effect of frequency on dimple depth for a dimple diameter of 1000 μm size at constant laser fluence of 2.18 J/cm^2 and pulse number of 50 is shown in Fig. 5.9. It can be seen in Fig. 5.9 that for a wavelength of 532 nm, laser frequency of 1 Hz and 4 Hz produces texture depth of ~16 μm and ~46 μm respectively. It can be observed here that material ablation increased to ~3 times from frequency of 1 Hz to 4 Hz. This can be attributed to the fact that lower laser frequency gives the target material enough time to transmit heat from the molten pool to specimen base. This leads to decrease in temperature within the laser-texture interaction area and making the melt to solidify and remain in the texture area.

However, for a same wavelength of 532 nm, laser frequency of 4 Hz and 10 Hz produces texture depth of ~46 μm and ~60 μm respectively. It can be observed here that material ablation increased to ~1.3 times from frequency of 4 Hz to 10 Hz. This may be due to preservation of melt temperature at higher frequencies due to lower pulse-pulse time period.

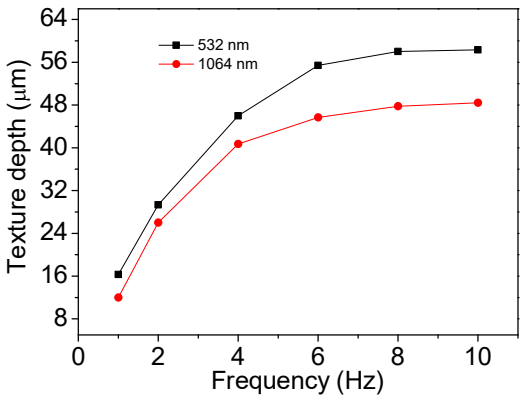

Fig. 5.9. The dimple depth vs frequency for the dimple size of 1000 μm at constant laser fluence of 2.18 J/cm^2 and pulse number of 50.

5.4 Fabrication of Multi-scale textures

In the above subsection the effect of laser parameters on texture size and depth is studied. In this sub-section multi-scale textures are the fabricated with the use of appropriate laser parameters like laser fluence, pulse number, frequency and wavelength.

The rectangular pins of 10×4 mm surface is fine polished with the same process mentioned in section 5.1. After polishing, the average surface roughness, R_a of the untextured pin specimens is 0.21±0.09 μm. From the previous chapter, it is observed that multi-scale textural configuration of elliptical shallow-triangular deep (ES-TD) exhibit better tribological performance. Therefore, in the present analysis, the same configuration (ES-TD) and multi-scale textural model proposed in the previous chapter is used. The multi-scale textural configuration in the present work is shown in Fig 5.10.

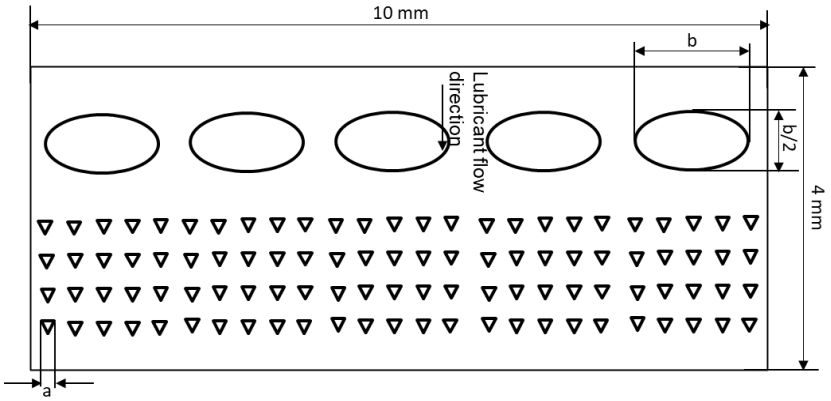

Fig. 5.10 Schematic diagram of multi-scale textural configuration used in the present analysis.

A similar procedure is followed for multi-scale textural fabrication as depicted in sub-section 5.2. However, to produce multi-scale textures of elliptical and triangular shapes, geometric beam shapers are used and these are placed along the laser beam propagation to alter the laser beam geometry from circular to the required shape. The geometric beam shapers used in the present analysis for elliptical and triangular texture fabrication are shown in Fig 5.11. The process of polishing and ultrasonic cleaning of textured pin specimen is similar to that of mentioned in section 5.2. The roughness of the textured surface after polishing and cleaning are 0.3±0.07 μm.

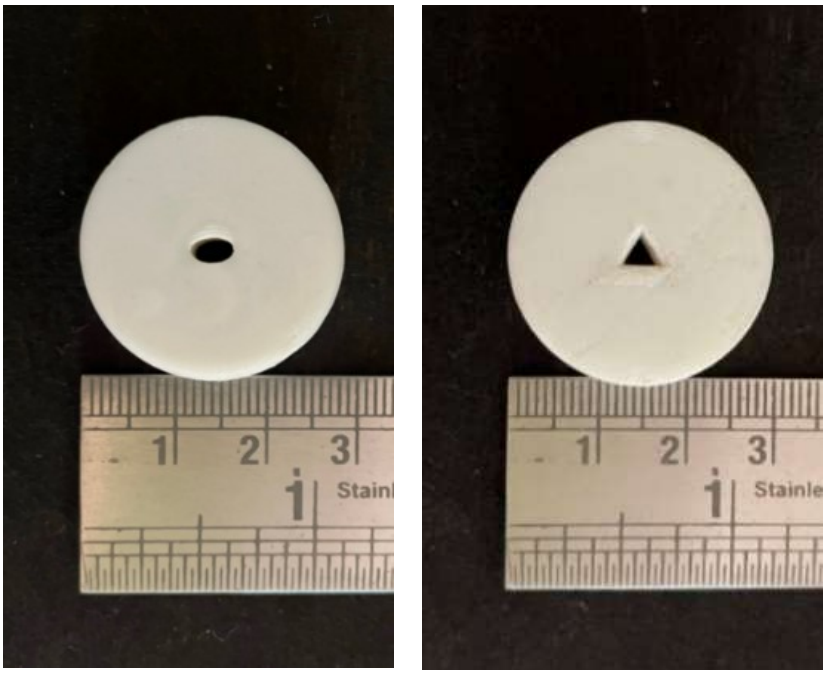

Fig. 5.11 Geometric beam shapers.

By using this method, multi-scale textures of different area densities and texture depths are fabricated. Multi-scale textural pin specimens of different area densities of 0.0 (Untextured), 0.1, 0.2, and 0.3 are shown in Fig. 5.12.

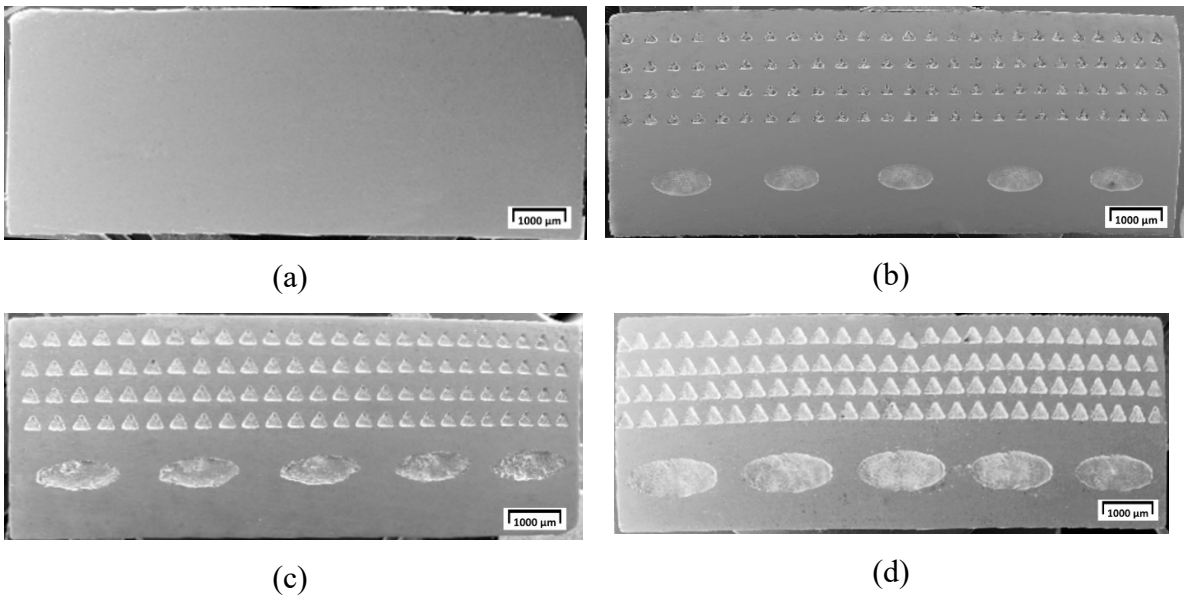

(a) (b)

(c) (d)

Fig. 5.12 Area densities of multi-scale textural configuration (a) *Ad*=0.0 (Untextured pin specimen) (b) *Ad*=0.1 (c) *Ad*=0.2 and (d) *Ad*=0.3.

The area density of 0.3 is chosen as maximum because area density of above 0.3 leads to overlapping of textures. The required texture sizes for elliptical and triangular textures are 1009.3 µm and 215.1 µm respectively for an area density of 0.1, 1427.1 µm and 303.9 µm

respectively for area density of 0.2, and 1747.7 µm and 372.2 µm respectively for area density of 0.3. Textures of each pin specimen are produced with constant frequency, wavelength, laser fluence and pulse number. Moreover, the horizontal movement of pin specimen is produced through motorized XYZ stage. Hence the sizes of each texture, and texture distribution are consistent throughout the experiment. The size and depth of textures is visualized through optical microscope of Huvitz make, HRM-300 model which is shown in Fig 5.13.

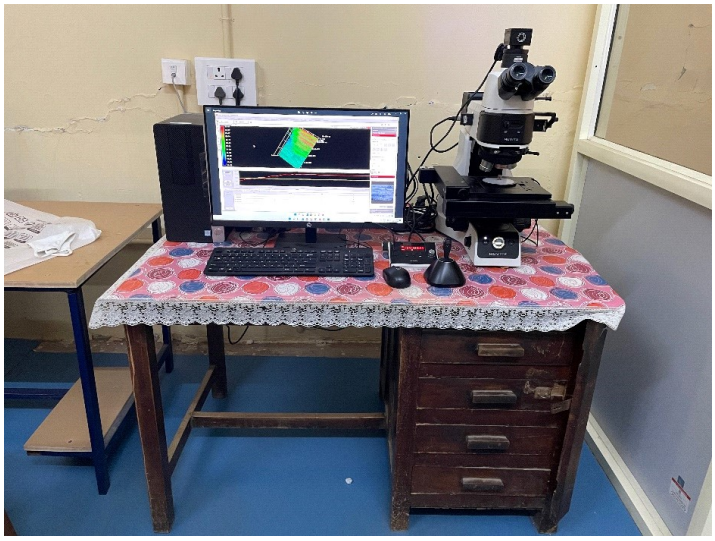

Fig 5.13 Optical microscope (Huvitz make, HRM-300 model, HR3-RF-P type).

The elliptical and triangular texture images of an area density 0.2 is shown in Fig. 5.14. The average sizes of elliptical and triangular texture shapes for different area densities obtained through laser texturing is depicted in Table. 5.3.

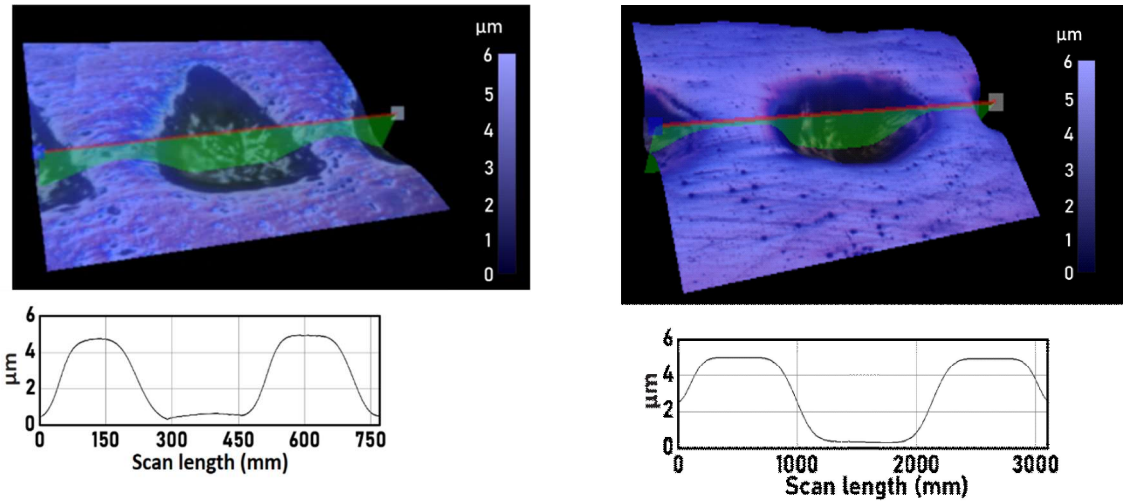

Fig 5.14 (a) triangular and (b) elliptical textures of area density 0.2 and texture depth 5 µm visualized through optical microscope.

Table 5.3 Laser fabricated texture sizes.

Area density	Elliptical texture size (µm)	Triangular texture size (µm)
0.1	1009±4	213±5
0.2	1429±5	304±4
0.3	1747±5	372±3

5.5 Summary

In this chapter, circular shaped surface textures have been developed on the specimen surface through an Nd: YAG laser. The effect of pulse number on dimple depth of 1000 µm diameter at different wavelengths of 532 nm and 1064 nm, and constant laser fluence and frequency of 2.18 J/cm^2 and 5 Hz respectively is studied. Moreover, the effect of frequency on dimple depth is studied at a constant laser fluence and pulse number of 2.18 J/cm^2 and 50 respectively at different wavelengths of 532 nm and 1064 nm. The multi-scale textures (elliptical and triangular shapes of different sizes) are also fabricated. Multi-scale textural configuration ES (1×1)-TD (4×5), of different textural area density and depth are developed on pin specimens by laser ablation method. Laser surface texturing does not affect environment, produced textures in less time period and has high efficiency compared to any other texturing processes. It is found that, texture depths increase with increase in frequency. However, significant change in texture depths can be observed at smaller frequencies. Target material has better laser energy absorption at wavelength of 532 nm. Moreover, multi-scale textures are successfully fabricated on pin specimens. In the chapter 6, the experimental analysis of textured surfaces on tribological performance parameters such as friction and wear are discussed.

Chapter 6

Impact of multi-scaled surface textures on tribological performance of parallel sliding contact under lubricated conditions

The previous chapter discussed about the Nd: YAG laser fabrication of dimples at constant laser fluence and varying pulse number, frequency and wavelengths. The fabrication of multi-scale textures using appropriate laser parameters are also discussed. Therefore, the present chapter reports the effect of multi-scale textural area density and depth on tribological parameters like frictional coefficient and wear rate through a Pin-on-disc test rig.

6.1 Experimental conditions

Uni-directional sliding tests were executed on the pin-on-disc test rig (Magnum make) under fully flooded lubricated environment. The pin-on-disc test rig used in the present analysis is shown in Fig 6.1. The counter-part material to the pin specimen was high carbon steel (AISI 52100) disc. The method of polishing of the disc is similar to that of a pin specimen which has been explained in the Section 5.1. After polishing, the average surface roughness, R_a of the disc is 0.28±0.08 μm. The disc material properties are shown in Table 6.1.

Table 6.1 Disc material properties.

Material	**Disc**
Type	AISI 52100
Modulus of Elasticity	215 GPa
Yield strength	450 MPa
Poisson's ratio	0.28
Hardness	848 VC
Average surface Roughness (R_a)	0.28±0.08 μm
Density (d)	7.81 g/cc

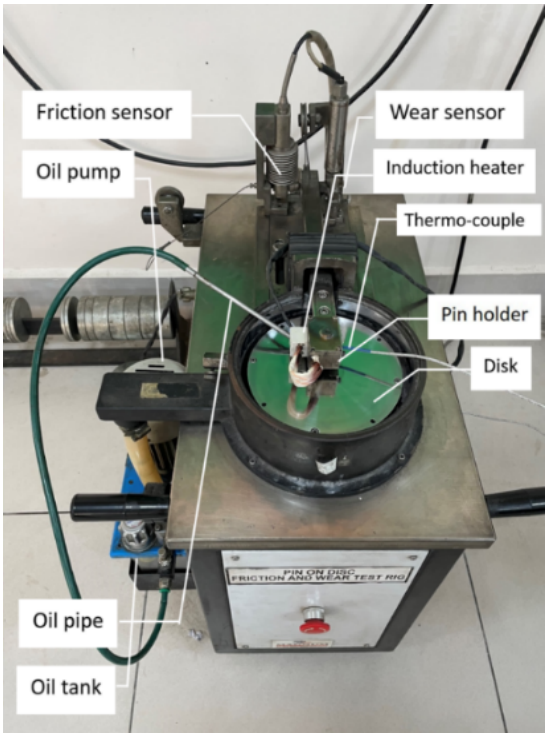

(a)

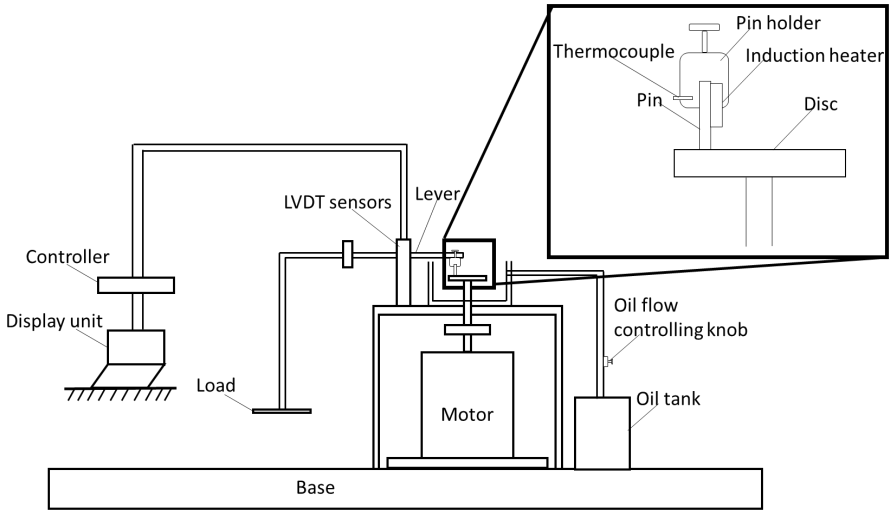

(b)

Fig. 6.1(a) Pin-on-disc test rig (Magnum make, TE-165-LE model) and (b) Schematic of Pin-on-disc test rig.

Commercially available SAE 15W-40 oil is supplied as a lubricant between the specimen-disc contact zone since this produces less sludge (Babu et al., 2020). The required viscosity of lubricant to supply between the contact pair is 0.01 Pa.s. However, the lubricant viscosity at ambient temperature is 0.15 Pa.s. Hence, the viscosity is measured at different temperatures using a redwood viscometer, and the viscosity variation with temperature are shown in Table. 6.2. The specimen-disc contact environment was heated using an induction heater to maintain

the contact temperature around 95°C during the test to obtain viscosity of 0.01 Pa.s. A thermocouple was attached 4 mm above the contact pair to measure the temperature.

Table 6.2 Viscosity of SAE15W-40 lubricant at different temperatures.

Temperature (°C)	30	95
Absolute viscosity (Pa. s)	0.15	0.01

The apparent contact pressure within the specimen-disc contact zone is changed from 1.25 MPa to 10 MPa, by altering the applied normal load from 50N to 400 N. Each specimen is tested for a sliding distance of 1000 m at 2 m/s speed. The experimental conditions are shown in Table 6.3. The lubricant is flowed at 12 drops/min to maintain fully flooded conditions (Venkateswara et al., 2019).

Table 6.3 Experimental conditions.

Test parameter	**Value**	**Unit**
Normal load (L_N)	50-400	N
Speed	2	m/s
Track radius	63	mm
Lubricant	SAE15W-40	-
Sliding distance (S_d)	1000	m

6.2 Friction and wear calculations

The test rig gives the data of instantaneous friction force values at a discrete-time gap of 0.1s for the whole test duration. The instantaneous friction force data considered for the calculation of average friction force is after 60 seconds because the period of 0 – 60 seconds are considered as running-in time period. The average friction force (F_{avg}) is calculated by dividing the summation of instantaneous friction force data with sliding distance (S_d). This calculated average friction force is used to determine the frictional coefficient using the *Eq. (6.1)*. The wear rate is calculated from the *Eq. (6.2)* in which weight loss of the specimen (ΔW) is obtained as the difference between initial weight (W_b) before conducting the test to final weight (W_a) after the test. . The specimens were cleaned with acetone in ultrasonic cleaner to remove all the wear debris present within the textures of specimen surface and the final weight (W_a) is calculated. The W_b and W_a were obtained through weighing machine which has an accuracy of ±0.0001 g. Each sliding test is conducted three times.

$$Frictional\ coefficient = \frac{F_{avg}}{L_N} \tag{6.1}$$

The average wear rate was calculated as follows

$$Wear\ rate = \frac{\Delta W}{d \times S_d} \tag{6.2}$$

$$\Delta W = W_b - W_a \tag{6.3}$$

Here, F_{avg} is the average frictional force, L_N is the applied normal load, W_b is the initial weight of the specimen, W_a is the final weight of the specimen, ΔW is the weight loss of the specimen due to wear, d is density of the specimen and S_d is the sliding distance.

6.3 Results and discussion

The rectangular AISI 1020 low carbon steel specimens of 10×4 mm^2 surface area is textured through Nd: YAG laser. Then, the specimens are polished to remove edge deposits. The tribological tests are conducted through pin-on-disc test rig under lubricated conditions at a constant speed of 2 m/s and at different loads. The area density and texture depth effect on frictional coefficient and wear rate are described in the below sub-sections.

6.3.1 Effect of area density on frictional coefficient and wear rate

In this sub-section, the effect of area density on frictional coefficient and wear rate of multi-scale textural specimens are studied at a texture depth of 5 µm, and a sliding speed of 2 m/s at different loads in between 50 N and 400 N. The effect of load on frictional coefficient and wear rate at different area densities is shown in Fig 6.2.

It can be observed from Fig. 6.2 that frictional coefficient and wear rate of untextured specimen increases with load. This is due to increased resistance of the specimen movement against the disc with load increment. By introducing textures on the specimen, a large reduction in frictional coefficient is observed (refer Fig.6.2 (a)). This is because, textures act as Rayleigh step bearing thereby producing film pressure and lubricant viscosity contributes the most to the frictional coefficient. At higher loads of 200 and 400 N, more asperity interlocking takes place and increases the frictional coefficient.

Among the textured specimens, higher texture area density produces a reduced frictional coefficient under considered loads. This can be due to the fact that higher area density textural specimens contain larger wedges, and generates higher film pressure. Moreover, at higher loading conditions, the larger area density textures can act as better lubricant reservoir and

transfers the lubricant into contact zone thereby reduces the frictional coefficient. The frictional coefficient decreased from 0.108 to 0.041 with the increase in area density from 0 (untextured) to 0.3 at a contact load of 50 N. Moreover, at higher load of 400 N, a reduced frictional coefficient is observed from 0.115 to 0.094 with the increase in area density from 0 (untextured) to 0.3.

The area density effect with load on wear rate is depicted in Fig. 6.2(b). It can be observed that lower wear rate is produced at lower load of 50 N. This is because of lower and narrower wear scars (refer Fig. 6.3(a)) as compared to higher load (refer Fig. 6.3(b)). Moreover, at lower load of 50 N, no/insignificant wear debris is observed inside the textures as compared to higher loads. This is due to lower asperity-asperity interlocking thereby producing lower wear scars and debris. A higher portion of asperity- asperity interlocks within the contact zone may wear off at higher load of 400 N (refer Fig 6.3(b)) due to which higher wear rate is observed as shown in Fig 6.2(b).

At lower loads, higher area density specimens exhibit a lower wear rate. This phenomenon is because of lower ploughing action between contact pair thereby producing lower scars (refer to Fig. 6.3(a)) and the similar kind of result is observed at higher load. This may be because of better accumulation of wear debris in higher area density textures, thereby minimizing third body abrasion. The accumulation of wear debris in textured specimens at higher loads of 400 N is shown in Fig 6.3(b). The wear rate decreased from 1.05×10^{-4} mm^3/m to 0.0635×10^{-4} mm^3/m with the change in area density from 0 (untextured) to 0.3 at a contact load of 50 N. Furthermore, at the higher load of 400 N, the wear rate decreased from 8.51×10^{-4} mm^3/m to 3.05×10^{-4} mm^3/m with the area density from 0 (untextured) to 0.3.

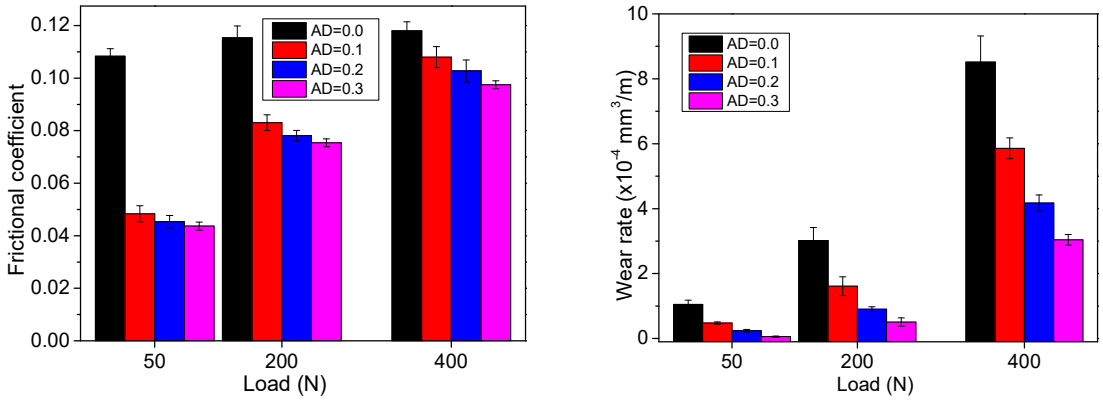

Fig. 6.2 Effect of area density on tribological properties (a) Frictional coefficient and (b) wear rate with load.

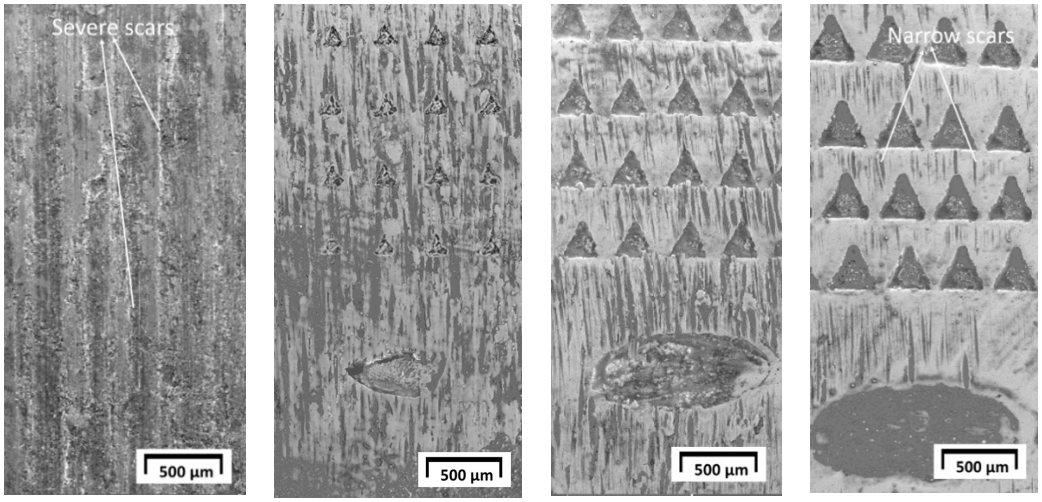

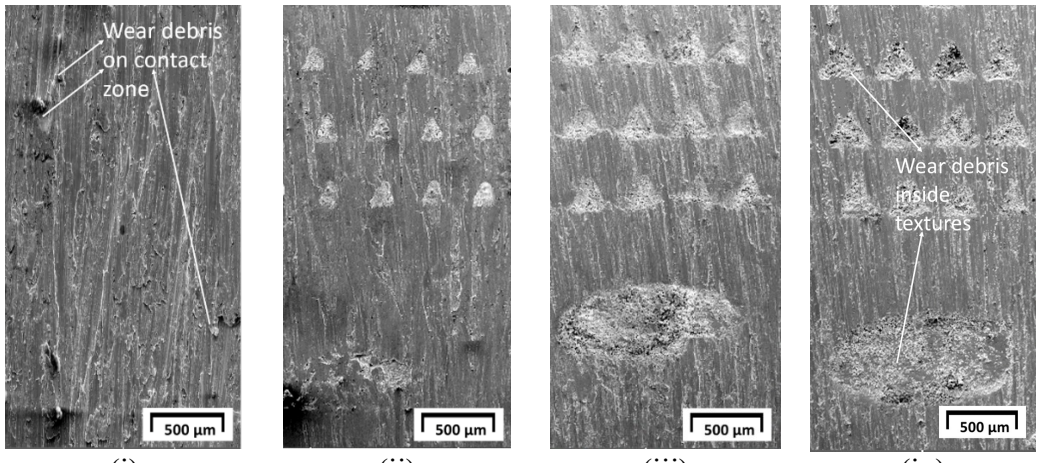

Fig. 6.3. Worn images of specimens at low and high loads of (a) 50 N and (b) 400 N of area density of (i) *Ad*= 0.0 (un-textured), (ii) *Ad*=0.1, (ii) *Ad*=0.2, and (iii) *Ad*=0.3.

6.3.2 Effect of texture depth on frictional coefficient and wear rate

The previous analysis depicts that an area density of 0.3 produced better tribological properties. Therefore, the frictional coefficient and wear rate are analyzed in this sub-section at an area density of 0.3 with different texture depths of 5, 10, and 15 μm. The texture depth is increased with a step of 5 μm. The consistency of texture depths are checked using optical microscope and has been observed in the range of 5±0.6 μm, 10±0.7 μm and of 15±0.9 μm respectively. The individual 3D images of different depths of multi-scaled textures and corresponding depth profiles scanned through optical microscope are shown in Fig 6.4.

The texture depth effect on frictional coefficient and wear rate of multi-scaled textures at a constant speed of 2 m/s are shown in Fig 6.5. It can be observed from Fig. 6.5 that frictional coefficient and wear rate increase with load at any considered texture depth. At the lower load of 50 N, the texture depth of 5 μm produced a lower frictional coefficient and wear rate (refer Fig. 6.5). This may be because of higher hydrodynamic effect at 5 μm texture depth in comparison with other texture depths. However, at higher loads of 200 N and 400 N, the texture depth of 10 μm produced reduced frictional coefficient and wear rate. This can be due to the synergic effect of texture depth of 10 μm producing adequate hydrodynamic pressures, contains enough lubricant to supply within the contact zone and effectively store large volume of wear debris.

Further increase in texture depth to 15 μm leads to increased frictional coefficient and wear rate at all considered loads, as shown in Fig 6.5. This can be attributed to the fluid cavitation, and recirculation effect leading to fluid backflow in multi-scaled textures thereby lubricant not producing enough film pressures to support the applied normal load. The frictional coefficient and wear rate decreased from 0.075 to 0.061 and 0.51×10^{-4} mm^3/m to 0.38×10^{-4} mm^3/m respectively with the increase in texture depth from 5 μm to 10 μm at a contact load of 200 N. Moreover, there is decrease in frictional coefficient and wear rate from 0.094 to 0.075 and 3.02×10^{-4} mm^3/m to 1.53×10^{-4} mm^3/m respectively with the increase in texture depth from 5 μm to 10 μm at a contact load of 400 N.

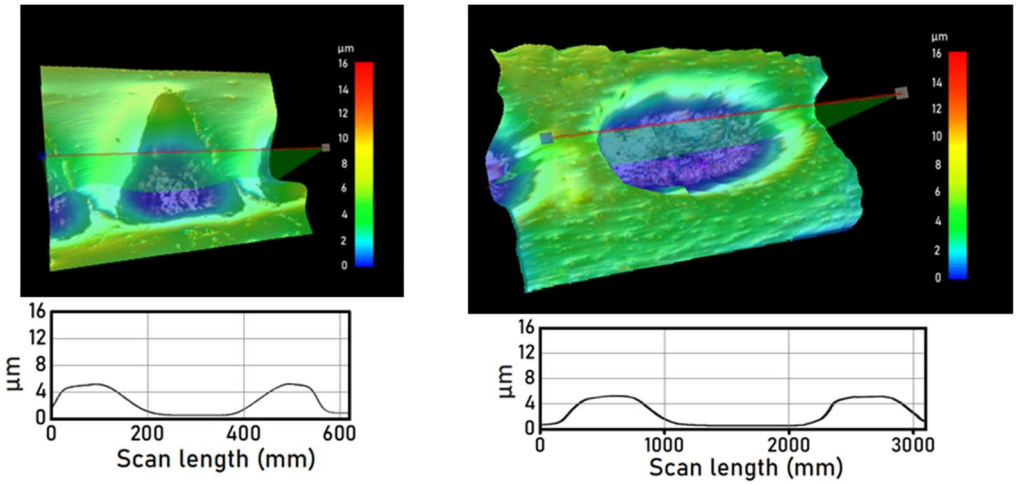

(i) (ii)

(a) 5 µm Texture depth

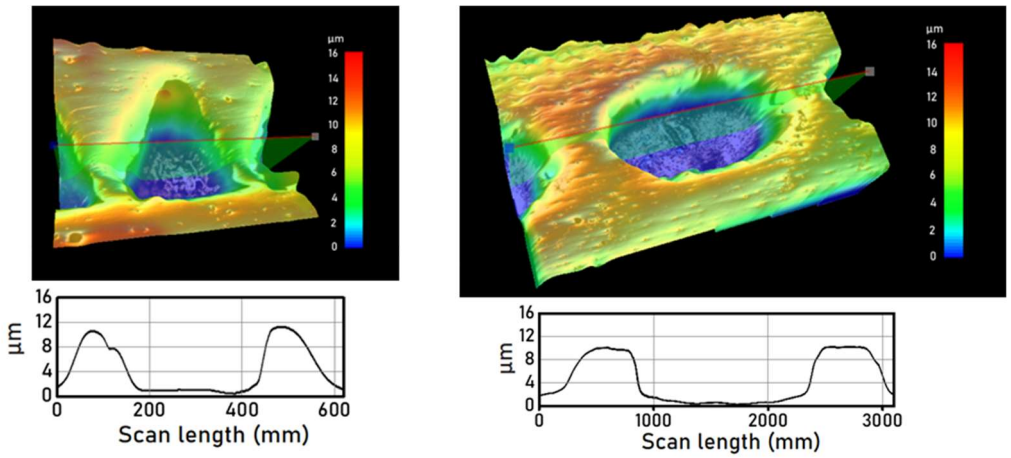

(i) (ii)

(b) 10 µm Texture depth

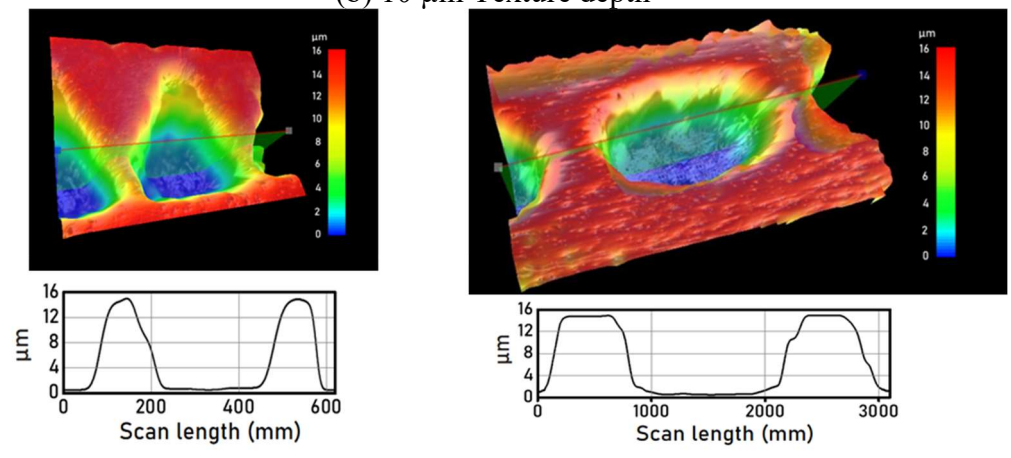

(i) (ii)

(c) 15 µm Texture depth

Fig. 6.4. Three-dimensional morphology and texture depth contours of (i) triangular and (ii) elliptical textures of texture depth of (a) 5 µm (b) 10 µm and (c) 15 µm at the area density of 0.3.

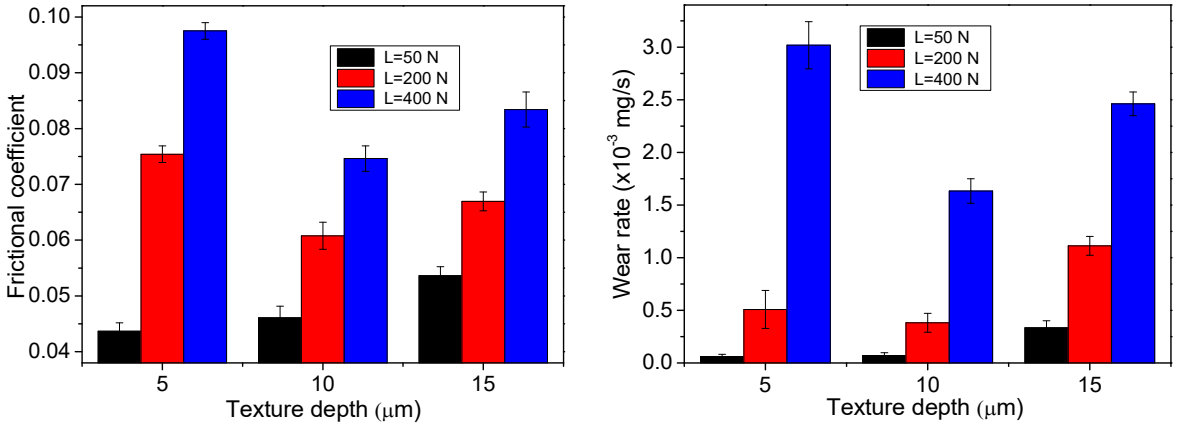

(a) (b)

Fig. 6.5. (a) Frictional coefficient and (b) wear rate graphs with load and texture depths.

6.3.3 Comparison of experimental results with numerical results

Experiment frictional coefficient results at an area density of 0.3 and texture depth of 5 μm are compared with previously obtained numerical results in Chapter 4. The frictional coefficient and wear rate are analyzed at a sliding speed of 2 m/s at different loads. The comparison of the experimental frictional coefficient with the numerical frictional coefficient is shown in Fig 6.6. Appropriate load is applied on a 10 mm×4 mm specimen such that the apparent pressure in both numerical and experimental cases remain the same. It can be observed from Fig. 6.6 that experimental results follow same trend with numerical results. However numerical results over predict the experimental results. This is because numerical analysis include assumptions like the fluid is Newtonian, iso-viscous (i.e., viscosity does not vary with pressure), negligible fluid inertia and slip effects. Moreover, the numerical analysis is performed at steady-state conditions, which is unreal and can't be adopted in the case of test conditions. The experimental results may include ambient errors like sudden change in humidity and slight differences in the required texture size and depth. These may be the reasons for the deviation of results between experimental and numerical. There is decrement of 2.75 % (minimum) and 5.1% (maximum) in experimental frictional coefficient as compared to numerical results for loads of 50 and 400 N respectively.

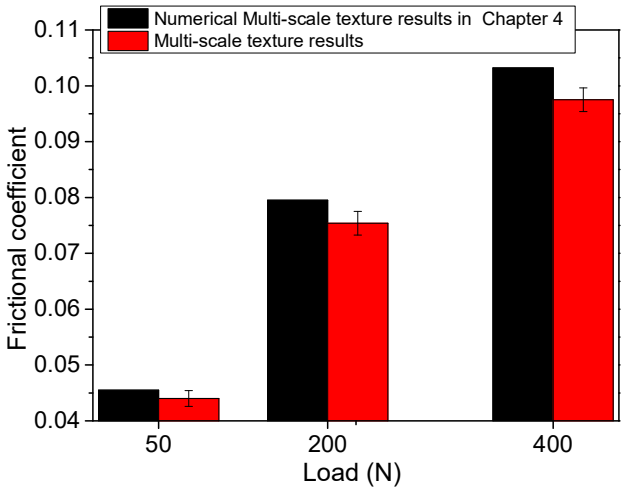

Fig. 6.6. Comparison of experimental frictional coefficient results with numerical at area density of 0.3 and texture depth of 5 µm.

6.3.4 Summary

In this chapter, an experimental study was carried out in order to understand the effect of multi-scale textures surfaces on the tribological performance of parallel sliding contact. After the fabrication of surface textures, the experimental analysis of textured surfaces on tribological performance parameters are discussed. The effect of area density on the frictional coefficient and wear rate is analyzed through a pin-on-disc test rig under fully lubricated conditions. Moreover, Multi-scale textures (elliptical shallow-triangular deep (ES-TD)) of different texture depths (5 µm, 10 µm, and 15 µm) are produced. The effect of texture depth on the frictional coefficient and wear rate is also studied. The experiments were performed at a constant sliding speed of 2 m/s and loads in the range of 50-400 N. The results depict that in most loading conditions, the area density of 0.3 and the texture depth of 10 µm exhibit better tribological properties. Moreover, the obtained experimental results are in-line with numerical results. The overall conclusion of the study and scope for the future work is reported in Chapter 7.

Chapter 7

Conclusions and future scope

The present dissertation focused on the tribological performance of single-scale and multi-scale textured parallel sliding contacts under mixed lubrication regime using mass conservative cavitation condition. In this context, a numerical model was developed to investigate the effects of textural parameters like area density, texture depth, surface roughness, texture number, area density, applied load and sliding velocity on tribological performance of sliding contact. In modelling, hydrodynamic pressures were calculated using the modified Reynolds equation (Patir and Cheng flow model) as well as asperity contact pressures using the Greenwood and Tripp model. The tribological parameters like minimum film thickness, hydrodynamic load percentage, and frictional coefficient was investigated. Different multi-scale textural configurations like Elliptical shallow- Elliptical deep (ES-ED), Elliptical shallow- Triangular deep (ES-TD) Triangular shallow- Triangular deep (TS-TD) and Triangular shallow- Elliptical deep (TS-ED) are optimised for better tribological performance. The optimised multiscale configuration was fabricated at different area densities and texture depths through an Nd: YAG laser. The effect of area density and texture depth on the frictional coefficient and wear rate was analysed under fully lubricated conditions. The experimental tests were also compared with previously obtained numerical results.

7.1 Conclusions

From the numerical and experimental studies performed, the conclusions of the present work can be summarized as follows:

- For single-scaled textures, area density of 0.2 to 0.3, texture depth of 2-6 μm and, combined average surface roughness of σ<0.9 μm produced better tribological performance.
- A single-scaled elliptical texture of an area density of 0.2, texture depth of 3 μm, surface roughness of 0.63 μm at a velocity of 8 m/s exhibit 268% higher film thickness and 74% lower frictional coefficient as compared to the un-textured surface.

- Multi-scaled textures of same height with different diameter produced better tribological performance as compared to multi-scaled textures of same diameter with different heights
- Multi-scaled elliptical shallow-triangular deep (ES-TD) configuration (shallow textures aspect ratio 0.0033 and deep textures aspect ratio 0.014) produce better tribological performance as compared to single scale elliptical textured surfaces (aspect ratio of 0.001) at all considered loads.
- For an area density of 0.3, considered lower load of 10 N (apparent contact pressure of 1.78 MPa) and velocity of 8 m/s, multi-scaled elliptical shallow-triangular deep configuration depicts 4.9 % lower frictional coefficient as compared to single-scaled elliptical texture. Moreover, for same area density and velocity, as load changed from 10 N to 80 N (apparent contact pressure of 14.28 MPa), 17.8 % reduction in frictional coefficient was observed as compared to single-scaled textures.
- Fluid couple stress parameter has positive effect on both single and multi-scaled textured parallel sliding contact.
- The multi-scale textural configuration is fabricated through an Nd: YAG laser. Laser frequency was found to be most influential parameter for texture depth than pulse number and wavelength.
- It has been observed from the experimental results that texture depth of 5 μm and 10 μm exhibit better tribological performance under lower load and higher load conditions respectively.
- A frictional coefficient reduction of 89.3% and wear rate reduction of 93.8% were obtained for multi-scaled textured surface of area density 0.3 and texture depth of 5 μm in comparison with un-textured surface at a lower load of 50 N (apparent contact pressure of 1.78 MPa).
- At a higher load 400 N (apparent contact pressure of 14.28 MPa), frictional coefficient and wear rate reduced to 37.2% and 80.8% respectively for multi-scaled textured surface of area density of 0.3, texture depth of 10 μm as compared to untextured surface.
- The experimental results are in line with the numerical results of multi-scale textures. The minimum and maximum deviation between the experimental and numerical results are 3.2 % and 5.5 % respectively.

7.2 Future scope

Based on the conclusion drawn in this chapter, following recommendations have been

made for future work

- The lubricant viscosity variation with pressure and temperature and its effect on hydrodynamic pressure and viscous friction can be studied.
- The tribological performance of parallel sliding contacts considering transient film thickness condition can be investigated.
- Tribological performance of geometrical patterns of mixing the two textures and variations of the land areas of multi-scale textures should be analysed.
- Analysis should be done on the residual stress developed due to laser strike and its effect on the tribological performance.

References

Abdel-Aal, H.A. and El Mansori, M., 2013. Tribological analysis of the ventral scale structure in a Python regius in relation to laser textured surfaces. *Surface Topography: Metrology and Properties*, *1*(1), p.015001.

Abhishek, K., Hiremath, S.S. and Karunanidhi, S., 2018. A novel approach to produce holes with high degree of cylindricity through Micro-Abrasive Jet Machining (μ-AJM). *CIRP Journal of Manufacturing Science and Technology*, *21*, pp.110-119.

Ahmed, A., Masjuki, H.H., Varman, M., Kalam, M.A., Habibullah, M. and Al Mahmud, K.A.H., 2016. An overview of geometrical parameters of surface texturing for piston/cylinder assembly and mechanical seals. *Meccanica*, *51*(1), pp.9-23.

Anno, J.N., Walowit, J.A. and Allen, C.M., 1968. Microasperity lubrication.

Anno, J.N., Walowit, J.A. and Allen, C.M., 1969. Load support and leakage from microasperity-lubricated face seals.

Arslan, A., Masjuki, H.H., Kalam, M.A., Varman, M., Mufti, R.A., Mosarof, M.H., Khuong, L.S. and Quazi, M.M., 2016. Surface texture manufacturing techniques and tribological effect of surface texturing on cutting tool performance: a review. *Critical Reviews in Solid State and Materials Sciences*, *41*(6), pp.447-481.

Ashwin, A.M. and Sashidhar, A.K.A.S.H., 2012. Frictional power minimization in partially textured piston ring assembly. *Int. J. Mech. Indust. Eng*, *2*(4), pp.40-44.

Aspinwall, D.K., Wise, M.L.H., Stout, K.J., Goh, T.H.A., Zhao, F.L. and El-Menshawy, M.F., 1992. Electrical discharge texturing. *International Journal of Machine Tools and Manufacture*, *32*(1-2), pp.183-193.

Babu, P.V., Ismail, S. and Ben, B.S., 2021. Experimental and numerical studies of positive texture effect on friction reduction of sliding contact under mixed lubrication. *Proceedings of the Institution of Mechanical Engineers, Part J: Journal of Engineering Tribology*, *235*(2), pp.360-375.

Bai L, Sun J, Zhang P, Khan ZA. Friction behavior of a textured surface against several materials under dry and lubricated conditions. Materials. 2021;14:5228.

Bhushan, B., 2009. Biomimetics: lessons from nature–an overview. *Philosophical Transactions of the Royal Society A: Mathematical, Physical and Engineering Sciences*, *367*(1893), pp.1445-1486.

Blatter, A., Maillat, M., Pimenov, S.M., Shafeev, G.A., Simakin, A.V. and Loubnin, E.N., 1999. Lubricated sliding performance of laser-patterned sapphire. *Wear*, *232*(2), pp.226-230.

Blau, P.J., Qu, J., Zhou, Y., Cooley, K.M., ERDMAN III, D.L. and Hsu, S.M., 2014. *Friction Reduction through Surface Modification* (No. ORNL/TM-2014/599). Oak Ridge National Lab.(ORNL), Oak Ridge, TN (United States).

Brizmer, V., Kligerman, Y. and Etsion, I., 2003. A laser surface textured parallel thrust bearing. *Tribology transactions*, *46*(3), pp.397-403.

Brown, M.S. and Arnold, C.B., 2010. Fundamentals of laser-material interaction and application to multiscale surface modification. In *Laser precision microfabrication* (pp. 91-120). Berlin, Heidelberg: Springer Berlin Heidelberg.

Buxton, A.L. and Dance, B.G.I., 2006. Surfi-Sculpt TM- Revolutionary surface processing with an electron beam. In *Surface Engineering; Proceedings of the 4 th International Surface Engineering Congress* (pp. 107-110).

Cannon, A.H. and King, W.P., 2009. Casting metal microstructures from a flexible and reusable mold. *Journal of Micromechanics and Microengineering*, *19*(9), p.095016.

Chattopadhyay, R., 2001. *Surface wear: analysis, treatment, and prevention*. *OH, USA,* ASM international.

Chen, W. and Ahmed, H., 1993. Fabrication of 5–7 nm wide etched lines in silicon using 100 keV electron-beam lithography and polymethylmethacrylate resist. *Applied physics letters*, *62*(13), pp.1499-1501.

Chilamakuri, S.K. and Bhushan, B., 1997. Optimization of asperities for laser-textured magnetic disk surfaces. *Tribology transactions*, *40*(2), pp.303-311.

Chong WWF, Teodorescu M and Rahnejat H., 2014. Mixed thermo-elastohydrodynamic cam–tappet power loss in lowspeed emission cycles. Int J Engine Res 2014; 15: 153–164

Coburn, J.W. and Winters, H.F., 1979. Plasma etching—A discussion of mechanisms. *Journal of vacuum Science and Technology*, *16*(2), pp.391-403.

Costa, H.L. and Hutchings, I.M., 2007. Hydrodynamic lubrication of textured steel surfaces under reciprocating sliding conditions. *Tribology international*, *40*(8), pp.1227-1238.

Cui, S., Zhou, Y., Wang, Y. and Zhai, L., 2020. Fish detection using deep learning. *Applied Computational Intelligence and Soft Computing*, *2020*, pp.1-13.

Dadouche, A. and Conlon, M.J., 2016. Operational performance of textured journal bearings lubricated with a contaminated fluid. *Tribology International*, *93*, pp.377-389.

Daniel, C., Mücklich, F. and Liu, Z., 2003. Periodical micro-nano-structuring of metallic surfaces by interfering laser beams. *Applied Surface Science*, *208*, pp.317-321.

De Wit, C.C. and Tsiotras, P., 1999, December. Dynamic tire friction models for vehicle traction control. In *Proceedings of the 38th IEEE conference on decision and control (Cat. no. 99CH36304)* (Vol. 4, pp. 3746-3751). IEEE.

Denkena, B., Abele, E., Brecher, C., Dittrich, M.A., Kara, S. and Mori, M., 2020. Energy efficient machine tools. *CIRP Annals*, *69*(2), pp.646-667. Denkena et al.,2020

Dobrica, M.B., Fillon, M., Pascovici, M.D. and Cicone, T., 2010. Optimizing surface texture for hydrodynamic lubricated contacts using a mass-conserving numerical approach. *Proceedings of the Institution of Mechanical Engineers, Part J: Journal of Engineering Tribology*, *224*(8), pp.737-750.

Dowson, D., 1993. Piston assemblies; background and lubrication analysis. In *Tribology Series* (Vol. 26, pp. 213-240). Elsevier.

Dumitru, G., Romano, V., Weber, H.P., Haefke, H., Gerbig, Y. and Pflüger, E., 2000. Laser microstructuring of steel surfaces for tribological applications. *Applied Physics A*, *70*, pp.485-487.

Dumitru, G., Romano, V., Weber, H.P., Haefke, H., Gerbig, Y. and Pflüger, E., 2000. Laser microstructuring of steel surfaces for tribological applications. Applied Physics A, 70(4), pp.485-487

Etsion, I., 2005. State of the art in laser surface texturing. *J. Trib.*, *127*(1), pp.248-253.

Etsion, I., 2010. Surface texturing for in-cylinder friction reduction. *Tribology and dynamics of engine and powertrain*, pp.458-470.l

Etsion, I., Halperin, G., Brizmer, V. and Kligerman, Y., 2004. Experimental investigation of laser surface textured parallel thrust bearings. *Tribology Letters*, *17*(2), pp.295-300.

Etsion, I., Kligerman, Y. and Halperin, G., 1999. Analytical and experimental investigation of laser-textured mechanical seal faces. *Tribology Transactions*, *42*(3), pp.511-516.

Feng, L., Zhang, Y., Li, M., Zheng, Y., Shen, W. and Jiang, L., 2010. The structural color of red rose petals and their duplicates. *Langmuir*, *26*(18), pp.14885-14888.

Fowell, M.T., Medina, S., Olver, A.V., Spikes, H.A. and Pegg, I.G., 2012. Parametric study of texturing in convergent bearings. Tribology International,52, pp.7-16.

Fu, Y.F., Yuan, C.Q. and Bai, X.Q., 2017. Marine drag reduction of shark skin inspired riblet surfaces. *Biosurface and Biotribology*, *3*(1), pp.11-24.

Gachot, C., Rosenkranz, A., Hsu, S.M. and Costa, H.L., 2017. A critical assessment of surface texturing for friction and wear improvement. *Wear*, *372*, pp.21-41.

Gachot, C., Rosenkranz, A., Wietbrock, B., Hirt, G. and Muecklich, F., 2013. Advanced Design of Hierarchical Topographies in Metallic Surfaces by Combining Micro-Coining and Laser Interference Patterning. *Advanced Engineering Materials*, *15*(6), pp.503-509.

Galda, L., Koszela, W. and Pawlus, P., 2007. Surface geometry of slide bearings after percussive burnishing. *Tribology International*, *40*(10-12), pp.1516-1525.

Galda, L., Pawlus, P. and Sep, J., 2009. Dimples shape and distribution effect on characteristics of Stribeck curve. *Tribology International*, *42*(10), pp.1505-1512.

Gao, Y., Wu, B., Zhou, Y. and Tao, S., 2011. A two-step nanosecond laser surface texturing process with smooth surface finish. *Applied Surface Science*, *257*(23), pp.9960-9967.

Geiger, M., Roth, S. and Becker, W., 1998. Influence of laser-produced microstructures on the tribological behaviour of ceramics. *Surface and Coatings Technology*, *100*, pp.17-22.

Gherca, A.R., Maspeyrot, P., Hajjam, M. and Fatu, A., 2013. Influence of texture geometry on the hydrodynamic performances of parallel bearings. *Tribology Transactions*, *56*(3), pp.321-332.

Grabon, W., Pawlus, P., Wos, S., Koszela, W. and Wieczorowski, M., 2018. Effects of cylinder liner surface topography on friction and wear of liner-ring system at low temperature. *Tribology International*, *121*, pp.148-160.

Greco, A., Martini, A., Liu, Y., Lin, C. and Wang, Q.J., 2010. Rolling contact fatigue performance of vibro-mechanical textured surfaces. *Tribology Transactions*, *53*(4), pp.610-620.

Green, M.A., 2002. Lambertian light trapping in textured solar cells and light-emitting diodes: analytical solutions. *progress in Photovoltaics: Research and Applications*, *10*(4), pp.235-241.

Greenwood, J.A. and Tripp, J.H., 1970. The contact of two nominally flat rough surfaces. *Proceedings of the institution of mechanical engineers*, *185*(1), pp.625-633.

Grützmacher, P.G., Profito, F.J. and Rosenkranz, A., 2019. Multi-scale surface texturing in tribology—current knowledge and future perspectives. *Lubricants*, *7*(11), p.95.

Grützmacher, P.G., Rosenkranz, A., Szurdak, A., Gachot, C., Hirt, G. and Mücklich, F., 2018. Effects of multi-scale patterning on the run-in behavior of steel–alumina pairings under lubricated conditions. *Advanced Engineering Materials*, *20*(1), p.1700521.

Grützmacher, P.G., Rosenkranz, A., Szurdak, A., König, F., Jacobs, G., Hirt, G. and Mücklich, F., 2018. From lab to application-Improved frictional performance of journal bearings induced by single-and multi-scale surface patterns. *Tribology International*, *127*, pp.500-508. (Grützmacher et al., 2018, a)

Gu, C., Meng, X., Xie, Y. and Li, P., 2016. A study on the tribological behavior of surface

texturing on the nonflat piston ring under mixed lubrication. *Proceedings of the Institution of Mechanical Engineers, Part J: Journal of Engineering Tribology*, *230*(4), pp.452-471.

Gu, C., Meng, X., Xie, Y. and Li, P., 2016. A study on the tribological behavior of surface texturing on the nonflat piston ring under mixed lubrication. *Proceedings of the Institution of Mechanical Engineers, Part J: Journal of Engineering Tribology*, *230*(4), pp.452-471.

Guichelaar, P., Folkert, K., Etsion, I. and Pride, S., 2002. Effect of micro-surface texturing on breakaway torque and blister formation on carbon-graphite faces in a mechanical seal. *Lubr. Engng*, *58*, pp.18-23.

Guzek, A., Podsiadlo, P. and Stachowiak, G.W., 2013. Optimization of textured surface in 2D parallel bearings governed by the Reynolds equation including cavitation and temperature. *Tribology Online*, *8*(1), pp.7-21.

Han, J., Fang, L., Sun, J. and Ge, S., 2010. Hydrodynamic lubrication of microdimple textured surface using three-dimensional CFD. *Tribology transactions*, *53*(6), pp.860-870.

Henry, Y., Bouyer, J. and Fillon, M., 2015. An experimental analysis of the hydrodynamic contribution of textured thrust bearings during steady-state operation: A comparison with the untextured parallel surface configuration. *Proceedings of the Institution of Mechanical Engineers, Part J: Journal of Engineering Tribology*, *229*(4), pp.362-375.

Holmberg, K. and Erdemir, A., 2017. Influence of tribology on global energy consumption, costs and emissions. *Friction*, *5*(3), pp.263-284.

Holmberg, K. and Erdemir, A., 2019. The impact of tribology on energy use and CO2 emission globally and in combustion engine and electric cars. *Tribology International*, *135*, pp.389-396.

Holmberg, K., Andersson, P. and Erdemir, A., 2012. Global energy consumption due to friction in passenger cars. *Tribology international*, *47*, pp.221-234.

Holzwarth, U. and Cotogno, G., 2012. Total hip arthroplasty. *Brussels: European Commission*.

Hsu, S.M., Jing, Y. and Zhao, F., 2015. Self-adaptive surface texture design for friction reduction across the lubrication regimes. *Surface Topography: Metrology and Properties*, *4*(1), p.014004.

Hsu, S.M., Jing, Y., Hua, D. and Zhang, H., 2014. Friction reduction using discrete surface textures: principle and design. *Journal of Physics D: Applied Physics*, *47*(33), p.335307.

Hu, Y., Cheng, H.S., Arai, T., Kobayashi, Y. and Aoyama, S., 1994. Numerical simulation of piston ring in mixed lubrication—a nonaxisymmetrical analysis.

Huang, J., Beckemper, S., Gillner, A. and Wang, K., 2010. Tunable surface texturing by polarization-controlled three-beam interference. *Journal of Micromechanics and Microengineering*, *20*(9), p.095004.

Iturralde, M.A., 2013. Surface micro texturing using modulation assisted machining.

Keller, J., Fridrici, V., Kapsa, P. and Huard, J.F., 2009. Surface topography and tribology of cast iron in boundary lubrication. *Tribology International*, *42*(6), pp.1011-1018.

Kelly, M.K., Rogg, J., Nebel, C.E., Stutzmann, M. and Kátai, S., 1998. High-Resolution Thermal Processing of Semiconductors Using Pulsed-Laser Interference Patterning. *physica status solidi (a)*, *166*(2), pp.651-657.

Khonsari, M.M., 2013. Reynolds Equation. In: Wang, Q.J., Chung, YW. (eds) Encyclopedia of Tribology. Springer, Boston, MA.

Kim, B., Chae, Y.H. and Choi, H.S., 2014. Effects of surface texturing on the frictional behavior of cast iron surfaces. *Tribology International*, *70*, pp.128-135.

Kinoshita, S., Yoshioka, S. & Kawagoe, K, 2002. Mechanisms of structural colour in the Morpho butterfly: cooperation of regularity and irregularity in an iridescent scale. Proc. R. Soc. B 269, 1417–1421.

Koch, K., Bhushan, B. and Barthlott, W., 2009. Multifunctional surface structures of plants: an inspiration for biomimetics. *Progress in Materials science*, *54*(2), pp.137-178.54, 137–178.

Komvopoulos, K., 2003. Adhesion and friction forces in microelectromechanical systems: mechanisms, measurement, surface modification techniques, and adhesion theory. *Journal of adhesion science and technology*, *17*(4), pp.477-517.

König, K., Krauss, O. and Riemann, I., 2002. Intratissue surgery with 80 MHz nanojoule femtosecond laser pulses in the near infrared. *Optics express*, *10*(3), pp.171-176.

Kovach JT, Tsakiris EA, Wong LT. Engine friction reduction for improved fuel economy.1982.

Kovalchenko, A., Ajayi, O., Erdemir, A., Fenske, G. and Etsion, I., 2004. The effect of laser texturing of steel surfaces and speed-load parameters on the transition of lubrication regime from boundary to hydrodynamic. *Tribology Transactions*, *47*(2), pp.299-307.

Kurella, A. and Dahotre, N.B., 2005. Surface modification for bioimplants: the role of laser surface engineering. *Journal of biomaterials applications*, *20*(1), pp.5-50.

Kuršelis, K., Kiyan, R. and Chichkov, B.N., 2012. Formation of corrugated and porous steel surfaces by femtosecond laser irradiation. *Applied surface science*, *258*(22), pp.8845-8852.

Leong, J.C. and Lin, C.Y., 2007. Effects of golf ball dimple configuration on aerodynamics, trajectory, and acoustics. *Journal of flow visualization and image processing*, *14*(2).

Li, K., Yao, Z., Hu, Y. and Gu, W., 2014. Friction and wear performance of laser peen textured surface under starved lubrication. *Tribology international*, *77*, pp.97-105.

Liu, K. and Jiang, L., 2011. Bio-inspired design of multiscale structures for function integration. *Nano Today*, *6*(2), pp.155-175.

Ma, C., Duan, Y., Yu, B., Sun, J. and Tu, Q., 2017. The comprehensive effect of surface texture and roughness under hydrodynamic and mixed lubrication conditions. *Proceedings of the Institution of Mechanical Engineers, Part J: Journal of Engineering Tribology*, *231*(10), pp.1307-1319.

Mahmoudi, B., Torkamany, M.J., Aghdam, A.S.R. and Sabbaghzade, J., 2010. Laser surface hardening of AISI 420 stainless steel treated by pulsed Nd: YAG laser. *Materials & Design (1980-2015)*, *31*(5), pp.2553-2560.

Malshe, A., Rajurkar, K., Samant, A., Hansen, H.N., Bapat, S. and Jiang, W., 2013. Bio-inspired functional surfaces for advanced applications. *CIRP Annals*, *62*(2), pp.607-628.

Marques, C., Desta, Y.M., Rogers, J., Murphy, M.C. and Kelly, K., 1997. Fabrication of high-aspect-ratio microstructures on planar and nonplanar surfaces using a modified LIGA process. *Journal of microelectromechanical systems*, *6*(4), pp.329-336.

Martz, L.S., 1949. Preliminary report of developments in interrupted surface finishes. *Proceedings of the Institution of Mechanical Engineers*, *161*(1), pp.1-9.

Mayer, G., 2005. Rigid biological systems as models for synthetic composites. *Science*, *310*(5751), pp.1144-1147.

Miao, J., Li, Y., Rao, X., Zhu, L., Guo, Z. and Yuan, C., 2019. Effects of different surface grooved cylinder liner on the tribological performance for cylinder liner-piston ring components. *Industrial Lubrication and Tribology*.

Mishra, P. and Ramkumar, P., 2018. *Effect of micro texture on tribological performance of piston ring-cylinder liner system under different lubrication regimes* (No. 2018-28-0052). SAE Technical Paper.

Mücklich, F., Lasagni, A. and Daniel, C., 2006. Laser Interference Metallurgy–using interference as a tool for micro/nano structuring. *International Journal of Materials Research*, *97*(10), pp.1337-1344.

Murthy, A.N., Etsion, I. and Talke, F.E., 2007. Analysis of surface textured air bearing sliders with rarefaction effects. *Tribology Letters*, *28*, pp.251-261.

Nagendra Prasad, K. and Syed, I., 2020. Influence of surface textures by ink-jet print followed by chemical etching process on the performance of HSS cutting tool. In *Advances in Applied Mechanical Engineering* (pp. 603-610). Springer, Singapore.

Nakano, M., Korenaga, A., Korenaga, A., Miyake, K., Murakami, T., Ando, Y., Usami, H. and Sasaki, S., 2007. Applying micro-texture to cast iron surfaces to reduce the friction coefficient under lubricated conditions. *Tribology letters*, *28*(2), pp.131-137.

Obergfell, K., Schulze, V. and Vöhringer, O., 2003. Classification of microstructural changes in laser hardened steel surfaces. *Materials Science and Engineering: A*, *355*(1-2), pp.348-356.

Olivier, J.G.J. and Janses-Maenhout, G., 2015. CO2 Emissions from Fossile Fuel Combustion Part III: Total Green House Gas Emissions. *International Energy Agency*.

Özmen, Ö., Sinanoğlu, C., Caliskan, A. and Badem, H., 2020. Prediction of leakage from an axial piston pump slipper with circular dimples using deep neural networks. *Chinese Journal of Mechanical Engineering*, *33*(1), pp.1-11.

Pascovici, M.D., Cicone, T., Fillon, M. and Dobrica, M.B., 2009. Analytical investigation of a partially textured parallel slider. *Proceedings of the Institution of Mechanical Engineers, Part J: Journal of Engineering Tribology*, *223*(2), pp.151-158.

Patir, N. and Cheng, H.S., 1978. An average flow model for determining effects of three-dimensional roughness on partial hydrodynamic lubrication.

Patir, N. and Cheng, H.S., 1979. Application of average flow model to lubrication between rough sliding surfaces.

Petare, A., Deshwal, G., Palani, I.A. and Jain, N.K., 2020. Laser texturing of helical and straight bevel gears to enhance finishing performance of AFF process. *The International Journal of Advanced Manufacturing Technology*, *110*(7), pp.2221-2238.

Prakash, V., Priyadarshni, N., Das, A.K. and Chattopadhyay, S., 2022. Fabrication of hydrophobic surface on Ti6Al4V by WEDM process for surgical instruments and bioimplants. *The International Journal of Advanced Manufacturing Technology*, pp.1-13.

Predescu, A., Pascovici, M.D., Cicone, T., Popescu, C.S., Grigoriu, C. and Dragulinescu, D., 2010. Friction evaluation of lubricated laser-textured surfaces. *Lubrication Science*, *22*(10), pp.431-442.

Qiu, M. and Raeymaekers, B., 2015. The load-carrying capacity and friction coefficient of incompressible textured parallel slider bearings with surface roughness inside the texture features. *Proceedings of the Institution of Mechanical Engineers, Part J: Journal of Engineering Tribology*, *229*(4), pp.547-556.

Qiu, M., Delic, A. and Raeymaekers, B., 2012. The effect of texture shape on the load-carrying

capacity of gas-lubricated parallel slider bearings. *Tribology Letters*, *48*, pp.315-327.

Qiu, M., Minson, B.R. and Raeymaekers, B., 2013. The effect of texture shape on the friction coefficient and stiffness of gas-lubricated parallel slider bearings. *Tribology International*, *67*, pp.278-288.

Rahmani, R., Mirzaee, I., Shirvani, A. and Shirvani, H., 2010. An analytical approach for analysis and optimisation of slider bearings with infinite width parallel textures. *Tribology International*, *43*(8), pp.1551-1565.

Rahmani, R., Shirvani, A. and Shirvani, H., 2007. Optimization of partially textured parallel thrust bearings with square-shaped micro-dimples. Tribology Transactions, 50(3), pp.401-406.

Rahnejat, H., Balakrishnan, S., King, P.D. and Howell-Smith, S., 2006. In-cylinder friction reduction using a surface finish optimization technique. *Proceedings of the Institution of Mechanical Engineers, Part D: Journal of Automobile Engineering*, *220*(9), pp.1309-1318.

Riveiro, A., Maçon, A.L., del Val, J., Comesaña, R. and Pou, J., 2018. Laser surface texturing of polymers for biomedical applications. *Frontiers in physics*, *6*, p.16.

Ronen, A., Etsion, I. and Kligerman, Y., 2001. Friction-reducing surface-texturing in reciprocating automotive components. *Tribology transactions*, *44*(3), pp.359-366.

Rosenkranz, A., Grützmacher, P.G., Murzyn, K., Mathieu, C. and Mücklich, F., 2021. Multi-scale surface patterning to tune friction under mixed lubricated conditions. *Applied Nanoscience*, *11*(3), pp.751-762.

Rosenkranz, A., Szurdak, A., Gachot, C., Hirt, G. and Muecklich, F., 2016. Friction reduction under mixed and full film EHL induced by hot micro-coined surface patterns. *Tribology International*, *95*, pp.290-297.

Rosenkranz, A., Szurdak, A., Grützmacher, P.G., Hirt, G. and Mücklich, F., 2018. Friction reduction induced by elliptical surface patterns under lubricated conditions. *Advanced Engineering Materials*, *20*(3), p.1700731.

Sahlin, F., Glavatskih, S.B., Almqvist, T.R. and Larsson, R., 2005. Two-dimensional CFD-

analysis of micro-patterned surfaces in hydrodynamic lubrication. *J. Trib.*, *127*(1), pp.96-102.

Schaffer, C.B., Jamison, A.O. and Mazur, E., 2004. Morphology of femtosecond laser-induced structural changes in bulk transparent materials. *Applied Physics Letters*, *84*(9), pp.1441-1443.

Segu, D.Z. and Hwang, P., 2015. Friction control by multi-shape textured surface under pin-on-disc test. *Tribology International*, *91*, pp.111-117.

Segu, D.Z. and Hwang, P., 2016. Effectiveness of multi-shape laser surface texturing in the reduction of friction under lubrication regime. *Industrial lubrication and Tribology*, 68(1): 116–124.

Segu, D.Z. and Kim, S.S., 2014. Influence on friction behavior of micro-texturing under lubricated non-conformal contact. *Meccanica*, *49*(2), pp.483-492.

Segu, D.Z., Choi, S.G., hyouk Choi, J. and Kim, S.S., 2013. The effect of multi-scale laser textured surface on lubrication regime. *Applied surface science*, *270*, pp.58-63.

Segu, D.Z., Kim, J.H., Choi, S.G., Jung, Y.S. and Kim, S.S., 2013. Application of Taguchi techniques to study friction and wear properties of MoS2 coatings deposited on laser textured surface. *Surface and Coatings Technology*, *232*, pp.504-514.

Seidel, H., 1990. The mechanism of anisotropic, electrochemical silicon etching in alkaline solutions. In *IEEE 4th Technical Digest on Solid-State Sensor and Actuator Workshop* (pp. 86-91). IEEE.

Shamsul Baharin, A.F., Ghazali, M.J. and A Wahab, J., 2016. Laser surface texturing and its contribution to friction and wear reduction: a brief review. *Industrial Lubrication and Tribology*, *68*(1), pp.57-66.

Sharma, N., Kango, S., Tayal, A., Sharma, R.K. and Sunil, 2016. Investigations on the influence of surface texturing on a couple stress fluid–based journal bearing by using JFO boundary conditions. *Tribology Transactions*, *59*(3), pp.579-584.

Shen, C. and Khonsari, M.M., 2016. The effect of laser machined pockets on the lubrication of piston ring prototypes. *Tribology International*, *101*, pp.273-283.

Sinanoğlu, C., Nair, F. and Karamış, M.B., 2005. Effects of shaft surface texture on journal bearing pressure distribution. *Journal of materials processing technology*, *168*(2), pp.344-353.

Singh, A. and Harimkar, S.P., 2012. Laser surface engineering of magnesium alloys: a

review. *Jom*, *64*, pp.716-733.

Siripuram, R.B. and Stephens, L.S., 2004. Effect of deterministic asperity geometry on hydrodynamic lubrication. *J. Trib.*, *126*(3), pp.527-534.

Song, F., Yang, X., Dong, W., Zhu, Y., Wang, Z. and Wu, M., 2022. Research and prospect of textured sliding bearing. *The International Journal of Advanced Manufacturing Technology*, pp.1-25.

Stephens, L.S., Siripuram, R., Hayden, M. and McCartt, B., 2002, January. Deterministic micro asperities on bearings and seals using a modified LIGA process. In *Turbo Expo: Power for Land, Sea, and Air* (Vol. 36096, pp. 573-580).

Sudrie, L., Franco, M., Prade, B. and Mysyrowicz, A., 2001. Study of damage in fused silica induced by ultra-short IR laser pulses. *Optics Communications*, *191*(3-6), pp.333-339.

Sun, M., Luo, C., Xu, L., Ji, H., Ouyang, Q. and Yu, D., 2005. Artificial lotus leaf by nanocasting. *Langmuir*, *21*(19), pp.8978-8981.

Sun, Z.B., Dong, X.Z., Chen, W.Q., Shoji, S., Duan, X.M. and Kawata, S., 2007. Two-and three-dimensional micro/nanostructure patterning of CdS–polymer nanocomposites with a laser interference technique and in situ synthesis. *Nanotechnology*, *19*(3), p.035611.

Sundaram, S.K. and Mazur, E., 2002. Inducing and probing non-thermal transitions in semiconductors using femtosecond laser pulses. *Nature materials*, *1*(4), pp.217-224.

Syed, I. and Sarangi, M., 2013, Influence of texture orientation on the hydrodynamic lubrication. In *Proceedings of 1st International and 16th National Conference on Machines and Mechanisms (iNaCoMM-2013), India* (pp. 850-856).

Syed, I. and Sarangi, M., 2014. Hydrodynamic lubrication with deterministic micro textures considering fluid inertia effect. *Tribology International*, *69*, pp.30-38.

Szurdak, A. and Hirt, G., 2015. Development and experimental verification of a new roller-coining setup to texture flat and curved surfaces. In *Applied Mechanics and Materials* (Vol. 794, pp. 128-135). Trans Tech Publications Ltd.

Szurdak, A., Rosenkranz, A., Gachot, C., Hirt, G. and Mücklich, F., 2014. Manufacturing and

tribological investigation of hot micro-coined lubrication pockets. In *Key Engineering Materials* (Vol. 611, pp. 417-424). Trans Tech Publications Ltd.

Tang, W., Kukulka, D.J., Smith, R. and Li, W., 2020. In-tube condensation and evaporation heat transfer coefficients in four enhanced surface tubes: An experimental investigation. *Chemical Engineering Transactions*, *81*, pp.439-444.

Tang, W., Zhou, Y., Zhu, H. and Yang, H., 2013. The effect of surface texturing on reducing the friction and wear of steel under lubricated sliding contact. *Applied surface science*, *273*, pp.199-204.

Tay, N.B., Minn, M. and Sinha, S.K., 2011. A tribological study of SU-8 micro-dot patterns printed on Si surface in a flat-on-flat reciprocating sliding test. *Tribology Letters*, *44*, pp.167-176.

Tomanik, E., Profito, F.J. and Zachariadis, D.C., 2013. Modelling the hydrodynamic support of cylinder bore and piston rings with laser textured surfaces. *Tribology international*, *59*, pp.90-96.

Uddin, M.S., Ibatan, T. and Shankar, S., 2017. Influence of surface texture shape, geometry and orientation on hydrodynamic lubrication performance of plane-to-plane slider surfaces. *Lubrication Science*, *29*(3), pp.153-181.

Venkateswara Babu P, Syed, I. and Beera, S.B., 2019. Influence of positive texturing on friction and wear properties of piston ring-cylinder liner tribo pair under lubricated conditions. *Industrial Lubrication and Tribology*, *71*(4), pp.515-524.

Vijayaraghavan D and Keith TG Jr. Development and evaluation of a cavitation algorithm. Tribol Int 1989; 32: 225–233.

Volchok, A., Halperin, G. and Etsion, I., 2002. The effect of surface regular microtopography on fretting fatigue life. *Wear*, *253*(3-4), pp.509-515.

Von der Linde, D. and Sokolowski-Tinten, K., 2000. The physical mechanisms of short-pulse laser ablation. *Applied Surface Science*, *154*, pp.1-10.

Wakuda, M., Yamauchi, Y., Kanzaki, S. and Yasuda, Y., 2003. Effect of surface texturing on friction reduction between ceramic and steel materials under lubricated sliding contact. *Wear*, *254*(3-4), pp.356-363.

Wang, Q.J. and Zhu, D., 2005. Virtual texturing: modeling the performance of lubricated contacts of engineered surfaces, *Trans. ASME, J. Tribol.*, 127(4):722-728.

Wang, W.Z., Huang, Z., Shen, D., Kong, L. and Li, S., 2013. The effect of triangle-shaped surface textures on the performance of the lubricated point-contacts. *Journal of Tribology, 135*(2).

Wang, X., Adachi, K., Otsuka, K. and Kato, K., 2006. Optimization of the surface texture for silicon carbide sliding in water. *Applied Surface Science*, *253*(3), pp.1282-1286.

Wang, X., Kato, K. and Adachi, K., 2002. The lubrication effect of micro-pits on parallel sliding faces of SiC in water. *Tribology transactions*, *45*(3), pp.294-301.

Wang, X., Kato, K., Adachi, K. and Aizawa, K., 2003. Loads carrying capacity map for the surface texture design of SiC thrust bearing sliding in water. *Tribology international*, *36*(3), pp.189-197.

Wang, X., Wang, J., Zhang, B. and Huang, W., 2015. Design principles for the area density of dimple patterns. *Proceedings of the Institution of Mechanical Engineers, Part J: Journal of Engineering Tribology*, *229*(4), pp.538-546.

Wen, L., Weaver, J.C. and Lauder, G.V., 2014. Biomimetic shark skin: design, fabrication and hydrodynamic function. *Journal of Experimental Biology*, *217*(10), pp.1656-1666.

Won, S.J. and Kim, H.S., 2019. Effects of laser parameters on morphological change and surface properties of aluminum alloy in masked laser surface texturing. *Journal of Manufacturing Processes*, *48*, pp.260-269.

Wu, C. and Zheng, L., 1989. An average Reynolds equation for partial film lubrication with a contact factor.

Wu, X., Ge, Z., Niu, H., Ruan, J. and Zhang, J., 2018. Edge effect factor affecting the tribological properties in water of protrusion surface textures on stainless steel. *Biosurface and*

Biotribology, *4*(2), pp.46-49.

Xie, Y., Li, Y., Wang, Y., Suo, S. and Liu, X., 2014. An experimental investigation of tribological performance of triangular textures in water lubrication regime. *Science China Physics, Mechanics and Astronomy*, *57*(2), pp.273-279.

Yin, B., Xu, B., Jia, H., Zhou, H., Fu, Y. and Hua, X., 2018. Effects of the array modes of laser-textured micro-dimples on the tribological performance of cylinder liner–piston ring. *Proceedings of the Institution of Mechanical Engineers, Part J: Journal of Engineering Tribology*, *232*(7), pp.871-881.

Yu, H., Deng, H., Huang, W. and Wang, X., 2011. The effect of dimple shapes on friction of parallel surfaces. *Proceedings of the Institution of Mechanical Engineers, Part J: Journal of Engineering Tribology*, *225*(8), pp.693-703.

Yu, H., Wang, X. and Zhou, F., 2010. Geometric shape effects of surface texture on the generation of hydrodynamic pressure between conformal contacting surfaces. *Tribology Letters*, *37*(2), pp.123-130.

Yu, T.H. and Sadeghi, F., 2001. Groove effects on thrust washer lubrication. *J. Trib.*, *123*(2), pp.295-304.

Yuan, S., Huang, W. and Wang, X., 2011. Orientation effects of micro-grooves on sliding surfaces. *Tribology International*, *44*(9), pp.1047-1054.

Yue, H., Deng, J., Ge, D., Li, X. and Zhang, Y., 2019. Effect of surface texturing on tribological performance of sliding guideway under boundary lubrication. *Journal of Manufacturing Processes*, *47*, pp.172-182.

Zhan X, Yi P, Liu Y, Xiao P, Zhu X, Ma J. Effects of single-and multi-shape laser-textured surfaces on tribological properties under dry friction. Proceedings of the Institution of Mechanical Engineers, Part C: J. Mech. Eng. Sci. 2020;234:1382-1392.

Zhan, J. and Yang, M., 2012. Investigation on dimples distribution angle in laser texturing of cylinder–piston ring system. *Tribology transactions*, *55*(5), pp.693-697.

Zhao, Y., 2014. The importance of lubricant and fluid analysis in predictive maintenance. *Spectro Scientific*.

Appendix A

The parallel rays emitting from a source is converged at focal point through as shown in Fig.5.15.

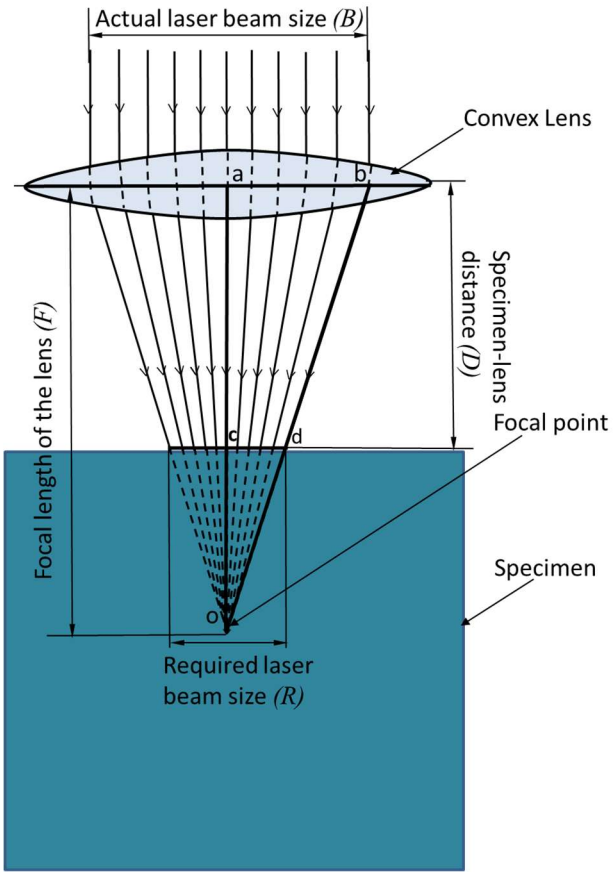

Fig. 5.15. Schematic representation of parallel rays' beam convergence through convex lens

By considering $\angle cod$ is similar to $\angle aob$

$$co/cd = ao/ab$$

$$(ao-ac)/cd = ao/ab$$

$$\frac{F-D}{(R/2)} = \frac{F}{(B/2)}$$

$$F-D = \frac{R.F}{B}$$

$$D = F\left[1-\frac{R}{B}\right]$$

Outcomes of the research

Publications in Journals:

1. Reddy AR and Ismail S. Tribological performance of textured parallel sliding contact under mixed lubrication condition by considering mass conservation condition and couple-stress parameter. *Proc. Inst. Mech. Eng.(ImechE) Part J: J. Eng. Tribol.* 2021; 235: 410-422, SAGE, SCI IF-1.758.

2. Annadi RR and Syed I. Tribological study of multi-scale textured parallel sliding contacts by considering a mixed lubrication regime and mass conservation condition. *Proc. Inst. Mech. Eng. (ImechE) Part J: J. Eng. Tribol.* 2022; 236: 807-822, SAGE, SCI IF-1.758.

3. Annadi RR, Syed I. Impact of multi-scaled surface textures on tribological performance of parallel sliding contact under lubricated condition. *Tribology .International.* 2023; 183: 108415. ELSEVIER, SCI IF-6.2.

Papers presented in National and International conferences:

1. Annadi RR, Syed I. The laser texturing of AISI 1020 material under ambient conditions using a nano-second pulsed laser. InAIP Conference Proceedings 2023 Jun 22 (Vol. 2810, No. 1).

2. Ramana Reddy Annadi, Syed Ismail, Effect of couple stresses parameter and mixed lubrication regime condition on the performance of piston ring/cylinder liner assembly by considering JFO cavitation condition, International Conference on Recent Advances in Materials, Manufacturing & Energy Systems (ICRAMMES), 3–4 January 2019, VRSEC, Vijayawada, Andhra Pradesh, India.

3. Ramana Reddy Annadi, Syed Ismail, Impact of hydrodynamic pressure gradient on oil friction in parallel sliding contacts, National Conference in Mechanical Engineering: Advances in Materials and Design (NCMEAMD), 19-21 May 2022, VIT, Bibwewadi, Pune, India.